ETH
Eidgenössische Technische Hochschule Zürich
Swiss Federal Institute of Technology Zurich

PAUL SCHERRER INSTITUT
PSI

Design and Fabrication of a Two-Dimensional Photonic Band Gap Structure for Terahertz-driven particle acceleration based on Fused Silica

Master Thesis

in Physiscs

Department D-PHYS

ETH Zurich

written by

BSc ETH Physics
Max Kellermeier

supervised by

Dr. A. Adelmann
Dr. R. Ischebeck

January 16, 2018

ETH

Eidgenössische Technische Hochschule Zürich
Swiss Federal Institute of Technology Zurich

Declaration of originality

The signed declaration of originality is a component of every semester paper, Bachelor's thesis, Master's thesis and any other degree paper undertaken during the course of studies, including the respective electronic versions.

Lecturers may also require a declaration of originality for other written papers compiled for their courses.

I hereby confirm that I am the sole author of the written work here enclosed and that I have compiled it in my own words. Parts excepted are corrections of form and content by the supervisor.

Title of work (in block letters):

Design and Fabrication of a Two-Dimensional Photonic Band Gap Structure for Terahertz-Driven Particle Acceleration Based on Fused Silica

Authored by (in block letters):

For papers written by groups the names of all authors are required.

Name(s):	**First name(s):**
Kellermeier	Max

With my signature I confirm that

- I have committed none of the forms of plagiarism described in the 'Citation etiquette' information sheet.
- I have documented all methods, data and processes truthfully.
- I have not manipulated any data.
- I have mentioned all persons who were significant facilitators of the work.

I am aware that the work may be screened electronically for plagiarism.

Place, date	**Signature(s)**
Villigen, 09.10.2017	Max

For papers written by groups the names of all authors are required. Their signatures collectively guarantee the entire content of the written paper.

Abstract

In this thesis a novel type of Terahertz waveguide suited for particle acceleration is proposed. Cylindrical rods of fused silica are arranged in a hexagonal lattice to attain photonic band gap guidance of a TM-like mode. The geometrical parameters are optimized for confinement, phase synchronization, and nearly suppressed higher order modes. At a rod radius of $r = 0.38\,\mathrm{a}$ and a hollow core diameter $r_D = 0.97\,\mathrm{a}$ with respect to the distance a between the rods, a characteristic impedance of $Z_c = 99\,\Omega$ is attained.

A new technique for micro-fabrication of fused silica, under current research and development, was explored with respect to feasibility of manufacturing structures close to the proposed one. After sampling the volumetric pattern with the focal spot of a femtosecond laser, the locally irradiated regions are exposed to an etchant which defines the microstructure. The attained results miss a hollow core and exhibit incomplete bulk etching as well as varied size in cylinder diameter. Difficulties arise in writing and etching deeply in the substrate because of spherical aberration of the laser and diffusion of the etchant into unexposed glass closer to the surface.

Contents

1 Introduction and Motivation

Conventional linear accelerating structures such as radiofrequency (RF) cavities are mostly limited by electrical breakdown of the metal wall at high electric fields. Typically, they can operate at gradients of $30 - 50\,\mathrm{MV/m}$ which leads to large devices for high energy particle acceleration. To attain the same particle energy with smaller devices new accelerator designs are needed to overcome the metallic breakdown limitation. High-gradient small accelerator devices will pave the road for many different applications, like tabletop free electron lasers or in-house medical accelerators.
High field gradients are attained in the optical frequency regime using current laser technology for broad-bandwidth pulses [1] but the short wavelengths will lead to energy spread if the bunch length is in the same order of magnitude or above. Timing to match the phase between guided mode and particle bunch also requires alignment in the length scale of the wavelength. Additionally, fabricating devices is more difficult on that length scale.
Terahertz frequencies provide a good balance between optical and radio frequencies. The breakdown threshold for surface electric fields increases into the GV/m range [2] and the long wavelength provides easier timing and higher charge per bunch as compared to optical frequencies. Fabricating three-dimensional (3D) devices on the length scale of $100\,\mu\mathrm{m}$ is also easier than on the $1\,\mu\mathrm{m}$ scale. Dielectric laser accelerators [3] are mostly investigated for optical operations. Recently, acceleration by single-cycle THz pulse centered at $0.45\,\mathrm{THz}$ have been demonstrated [2]. The pulse, generated by optical rectification, was coupled into a dielectric-loaded circular waveguide which supports an accelerating speed of light (SOL) TM-mode. An on-axis gradient of $10\,\mathrm{MV/m}$ was achieved. With further advances in strong-field Terahertz (THz) generation [4] a rapid increase in acceleration gradient is expected.
With the focus on an accelerator waveguide, a new manufacturing technique will be explored [5]. An infrared (IR) femtosecond laser pulse irradiates fused silica locally and samples a three dimensional pattern inside the substrate. The laser exposed zones are chemically etched, leading to high-aspect ratio volumetric structures. The technique shall be used to fabricate an all-dielectric terahertz waveguide for particle acceleration which will not be limited by RF induced breakdown but only by particle and laser irradiation damage.
To attain wave confinement in hollow core a new waveguide for terahertz is designed. Photonic band gap structures, such as the silicon based woodpile [6] or the fused silica photonic band gap fiber [7], have been designed and fabricated [8] for acceleration with optical and IR frequencies. For Terahertz, hollow core photonic band gap fibers provide propagation with low absorption losses [9], but, to the best of our knowledge, up to now no photonic band gap waveguide has been designed to guide terahertz modes for particle acceleration.

This thesis consists of two main parts. The first one focuses on designing an appropriate photonic band gap structure, while the second part serves as a feasibility study of the manufacturing process for such devices. An overview of photonic crystal theory and fused silica properties will be given in the next section.

2 Theoretical Fundamentals

The following chapter will give an overview of the theoretical understanding of photonic crystals and photonic band gap structures. It is not stated everywhere explicitly, but the following sections summarize the introductory given in *Photonic Crystals - Molding the Flow of Light* by J. Joannopoulos, S. Johnson, J. Winn and R. Meade [10].

2.1 Electromagnetism as an Eigenvalue Problem

Every macroscopic electromagnetic phenomenon is described by the Maxwell's equations

$$\begin{aligned} \nabla \cdot \mathbf{D} &= \rho, \\ \nabla \cdot \mathbf{B} &= 0, \\ \nabla \times \mathbf{E} + \partial_t \mathbf{B} &= 0, \\ \nabla \times \mathbf{H} - \partial_t \mathbf{D} &= \mathbf{j}, \end{aligned} \tag{2.1}$$

where $\mathbf{E}$ and $\mathbf{H}$ are the macroscopic electric and magnetic fields, $\mathbf{D}$ and $\mathbf{B}$ are the electric and magnetic displacement fields, and ρ and $\mathbf{j}$ are the free charge and current densities, respectively. The fields are time and space dependent, $\mathbf{E} = \mathbf{E}(\mathbf{r}, t)$, although the explicit notation of dependence is omitted here.
In general the dielectric permittivity ε, which relates the $\mathbf{E}$-field and the electric displacement field by

$$\mathbf{D} = \varepsilon \mathbf{E},$$

is a tensor of rank two. The same is valid for the magnetic permeability μ, which describes the relation between the $\mathbf{H}$- and the $\mathbf{B}$-field by

$$\mathbf{H} = \mu \mathbf{B}.$$

In the following we will limit ourselves to homogeneous isotropic media for which ε and μ are scalars. It is common to characterize a material by its relative optical properties ε_r and μ_r with respect to the vacuum permittivity ε_0 and permeability μ_0, meaning that

$$\begin{aligned} \varepsilon &= \varepsilon_r \varepsilon_0, \\ \mu &= \mu_r \mu_0. \end{aligned}$$

We will consider mixed media, composites of regions of homogeneous dielectric materials, in which ε is a function of the position, $\varepsilon = \varepsilon(\mathbf{r})$. This media composite does not change over time and is restricted to the source-free case, in which we set $\rho = 0$ and $\mathbf{j} = 0$.
To further simplify the electromagnetic propagation problem material dispersion is ignored. The dielectric permittivity is a function of the field's frequency, $\varepsilon(\omega)$, but far from any absorption edge and as long as the frequency range of interest is not to large, ε can be treated as a constant. Whether or not the frequency range is small enough depends on the material dispersion itself and the requirements of our problem in study. For instance, if a deviation of ε by 5 % is acceptable for the outcome, a frequency range in which $\varepsilon(\omega)$ deviates only by this percentage can be treated as constant permittivity. Later, an explicit example is given in chapter 3.1.

Similar assumptions can be made for the permeability. For most dielectric materials $\mu_r \approx 1$ is a very good approximation. Media, which have a permeability differing significantly from the vacuum permeability are not taken into account for our studies. Finally, the media of interest are assumed to be transparent which means that ε_r is real and positive. Therefore, light can propagate lossless through the medium. The refractive index, generally $n = \sqrt{\mu_r \varepsilon_r}$, is reduced to the square root of ε_r.

Applying those assumptions, Maxwell's equations (2.1) become

$$\nabla \cdot (\varepsilon(\mathbf{r})\mathbf{E}) = 0, \tag{2.2}$$
$$\nabla \cdot \mathbf{H} = 0, \tag{2.3}$$
$$\nabla \times \mathbf{E} + \mu_0 \partial_t \mathbf{H} = 0, \tag{2.4}$$
$$\nabla \times \mathbf{H} - \varepsilon_r(\mathbf{r})\varepsilon_0 \partial_t \mathbf{E} = 0. \tag{2.5}$$

Due to the linearity of Maxwell's equations the solutions can be expanded in harmonic modes which allow to separate the spatial dependence from the time dependence, $\mathbf{H}(\mathbf{r}, t) = \mathbf{H}(\mathbf{r})e^{-i\omega t}$ and $\mathbf{E}(\mathbf{r}, t) = \mathbf{E}(\mathbf{r})e^{-i\omega t}$. This is not a strong restriction since by Fourier analysis any other solution can be build from linear combinations of harmonics.

The two curl equations (2.4) and (2.5) relate both separated fields $\mathbf{E}(\mathbf{r})$ and $\mathbf{H}(\mathbf{r})$ to each other. To decouple them, first, equation (2.5) is divided by $\boldsymbol{\varepsilon}(\mathbf{r})$. Taking the curl and inserting equation (2.4) for $\nabla \times \mathbf{E}(\mathbf{r})$ results in

$$\nabla \times \left(\frac{1}{\varepsilon(\mathbf{r})} \nabla \times \mathbf{H}(\mathbf{r}) \right) = \left(\frac{\omega}{c} \right)^2 \mathbf{H}(\mathbf{r}). \tag{2.6}$$

Here, ε_0 and μ_0 were replaced by the vacuum speed of light,

$$c = \frac{1}{\sqrt{\varepsilon_0 \mu_0}}.$$

and, from now on, $\varepsilon(\mathbf{r})$ denotes the relative permittivity. Equation (2.6) is the fundamental eigenvalue problem which we have to solve for a given permittivity distribution $\varepsilon(\mathbf{r})$, additionally restricted by the transversality requirement in equation (2.3). For a certain solution, $\mathbf{E}(\mathbf{r})$ is fixed as well due to Maxwell's fourth equation, eq. (2.5).

As stated above, the problem is considered an eigenvalue problem. To see this, it is expressed as

$$\hat{\Theta}\mathbf{H}(\mathbf{r}) = \left(\frac{\omega}{c} \right)^2 \mathbf{H}(\mathbf{r}), \tag{2.7}$$

in which $(\omega/c)^2$ on the right hand side is termed the eigenvalue of the differential operator

$$\hat{\Theta} = \nabla \times \frac{1}{\varepsilon(\mathbf{r})} \nabla \times \quad .$$

Without explicit explanation it is an important feature from a mathematical point of view that the operator is not only linear, but also Hermitian. This imposes some properties which are well known from the eigenvalue problem of quantum mechanics. The eigenvalues are positive, including ω to be real, and states of different frequencies ω_1 and ω_2 are *orthogonal*. If two different harmonic modes happen to have equal frequencies they are called degenerate. This

degeneracy relies on a symmetry of the system and the fields are not necessarily orthogonal. Table 2.1 shows the analogy between the quantum mechanical Schrödinger equation for a wave function and the electromagnetic eigenproblem.

While we have formulated the eigenvalue problem in terms of the magnetic field $\mathbf{H}(\mathbf{r})$ the use of the electric field is physically identical. Unfortunately the operator for the electric field formulation is not Hermitian anymore. The equation can be expressed as a so called generalized eigenproblem, having Hermitian operators on both sides of the equation. But for numerical studies this is impractical due to the transversality constraint depending on ε, eq. (2.2).
To have a Hermitian operator in the eigenproblem and an easier applicable transversality constraint one can use the electric displacement field $\mathbf{D}$. Since the operator for this formulation is more complex it is convenient to retain the $\mathbf{H}$ formulation.

2.2 Importance of Symmetries

If our system of interest has certain symmetries the electromagnetic modes can be classified by eigenvalues of the symmetry operators. This is again an analog to quantum mechanics. Here, we focus on application of this classification. For a fundamental explanation we refer to [10, p.27ff]. As a first example consider continuous translational symmetry in two directions, the xy plane . In terms of the translation operator $\hat{T}_{\mathbf{d}}$, which shifts the argument of a function by the vector $\mathbf{d}$, we have

$$\hat{T}_{\mathbf{d}}\varepsilon(\mathbf{r}) = \varepsilon(\mathbf{r}-\mathbf{d}) = \varepsilon(\mathbf{r}) \tag{2.8}$$

for arbitrary vectors $\mathbf{d}$ in the xy plane . In this case the eigenfunctions of $\hat{T}_{\mathbf{d}}$ are given by $e^{i(k_x x+k_y y)}$ for some k_x and k_y, up to a constant prefactor. Since the eigenfunctions of a symmetry operator of our system and the operator $\hat{\Theta}$ from our eigenproblem must have common eigenfunctions, the xy dependence is separable,

$$\mathbf{H}_{\mathbf{k}}(\mathbf{r}) = e^{i(k_x x+k_y y)}\mathbf{H}(z), \quad \text{where } \mathbf{k} = (k_x, k_y).$$

Any mode is therefore at least identified by its in-plane wavevector $\mathbf{k}$. But it's not sufficient to identify a mode uniquely. For a certain wavevector there may be multiple modes with the same $\mathbf{k}$ due to the z dependence. Whether or not this direction obeys an additional symmetry, we can at least label the states in order of increasing frequency ω by an additional number n. Then $(\mathbf{k}, n)$ identifies a state uniquely. If some states are degenerate a third index has to be included to label them.
Since we haven't assumed anything about the z dependence the labeling can be either continuous

Table 2.1: Comparison between quantum mechanics and electrodynamics [10, p. 23]

	Quantum Mechanics	*Electrodynamics*
Field	$\Psi(\mathbf{r},t) = \Psi(\mathbf{r})e^{-iEt/\hbar}$	$\mathbf{H}(\mathbf{r},t) = \mathbf{H}(\mathbf{r})e^{-i\omega t}$
Eigenvalue problem	$\hat{H}\Psi = E\Psi$	$\hat{\Theta}\mathbf{H} = \left(\frac{\omega}{c}\right)^2\mathbf{H}$
Hermitian operator	$\hat{H} = -\frac{\hbar^2}{2m}\nabla^2 + V(\mathbf{r})$	$\hat{\Theta} = \nabla \times \frac{1}{\varepsilon(\mathbf{r})}\nabla \times$

or discrete, or partially discrete up to a certain frequency and continuous above. The later case is observed for the example of a glass slab in the next paragraph.

Due to the translational symmetry in xy being continuous, the wavevector $\mathbf{k}$ as a label for the modes is also continuous and the frequency is expressed as a dependence on the wavevector, $\omega = \omega(\mathbf{k})$. This is called a dispersion relation. But since there are multiple modes with the same wave vector the dependence extends to $\omega = \omega(\mathbf{k}, n)$. This is often called a band structure or band diagram where the label n is referred to as band number.

As an example, the band diagram of an infinite glass slab is shown in figure 2.1. For a fixed $\mathbf{k}$ the band number is discrete as long as the frequency is below the SOL dispersion $\omega = c|\mathbf{k}|$. Above, it becomes continuous and, in fact, corresponds to states which extend into air. Far from the plate those states are additionally classified by k_z, the third component of the wave vector.

What does this classification by symmetry mean for labeling quantities, like $\mathbf{k}$ in the example? It's of great importance that they are conserved quantities such that a field pattern starting with wavevector $\mathbf{k}$ will keep this wavevector for all future times.
Another important point to mention here is the breaking of such symmetries. A broken symmetry mixes states which were distinct before. For instance, it allows coupling between different modes at interfaces.

Instead of discussing every symmetry operation and its corresponding conserved quantity in detail we provide an overview here:

Time translation invariance Analogously to the above space-translation symmetry the continuous time-translation can be studied. While the conservation of $\mathbf{k}$ depends on the geometric properties of $\varepsilon(\mathbf{r})$, time-translation invariance is a property of Maxwell's equation and therefore holds for any arbitrary geometry. As a consequence the frequency ω is a conserved quantity.

Time reversal symmetry For lossless materials the eigenvalues of eq. (2.6) are real. As a consequence the complex conjugate of a mode is also a solution with the same eigenvalue. Taking the complex conjugate is equivalent to reversing the time in Maxwell's equations. For states classified by the wavevector it follows $\omega(\mathbf{k}) = \omega(-\mathbf{k})$.

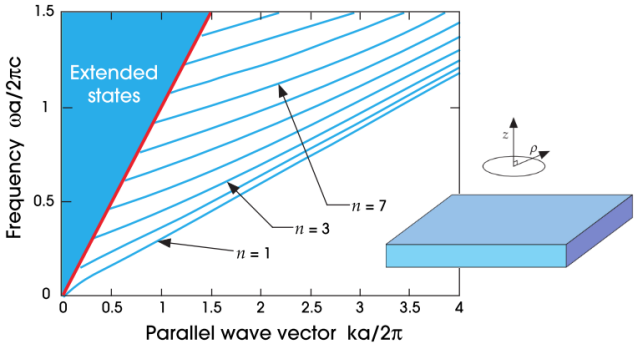

Figure 2.1: Band diagram of an infinitely extended glass slab, shown in the inlet. The slab is translationally symmetric in the xy plane which is why the eigenmodes are classified by the conserved in-plane wavevector. [10, p. 30]

Rotational symmetry Rotating the reference frame may also leave the system invariant. The above scenario of a glass slab is symmetric under continuous rotations around the z axis. It follows that $\omega(\mathcal{R}_\alpha \mathbf{k}) = \omega(\mathbf{k})$ for any α, where $\mathcal{R}(\alpha)$ is the rotation operator around the z axis by the angle α. In fact this allowed us to neglect the vectorial character of $\mathbf{k}$ in the band diagram, $\omega(\mathbf{k}) = \omega(k = |\mathbf{k}|)$, Fig. 2.1.
If the system is only invariant under discrete rotations, like crystals or the structure discussed in section 5.3,

$$\varepsilon(\mathcal{R}_n \mathbf{r}) = \varepsilon(\mathbf{r}) \quad \text{for a certain integer } n \text{ and } R_n = R(\alpha = \tfrac{2\pi}{n}),$$

the vectorial character cannot be ignored. But the symmetry introduces redundancy such that it is sufficient to compute only a fraction of the modes. The specific consequence will be explained for crystals in section 2.4.

Mirror symmetry If the system is symmetric around a mirror plane it allows to distinguish certain modes by their polarization. For a mirror reflection $\mathcal{M}$ being a symmetry of the system, $\varepsilon(\mathcal{M}\mathbf{r}) = \varepsilon(\mathbf{r})$, modes with in-plane wavevector $\mathcal{M}\mathbf{k} = \mathbf{k}$ are also eigenstates of the reflection operator. Their eigenvalues are ± 1 such that the fields are either even or odd under reflections. Even modes have only in-plane $\mathbf{E}$ components while $\mathbf{H}$ is purely perpendicular to the mirror plane. Therefore they are called **TE** modes. For odd modes exactly the opposite is true and they are called **TM** due to the purely in-plane $\mathbf{H}$ field.
This separation in general holds only at $\mathcal{M}\mathbf{r} = \mathbf{r}$ for $\mathcal{M}\mathbf{k} = \mathbf{k}$. In an effectively two-dimensional (2D) system, having a uniform distribution along the third component, all modes can be classified as being either TM or TE, as long as only the in-plane wavevector is considered. Let $\mathbf{k}_\parallel$ be the wavevector in the mirror plane, and $k_\perp$ the out-of-plane component. For a mode at $\mathbf{k} = (\mathbf{k}_\parallel, 0)$ having a certain polarization, a small perturbation to $k_\perp$, $k_\perp \neq 0$, cannot completely destroy this polarization. Such modes are hybrid modes but are either associated as **TM-like** or **TE-like**.

Continuous translation symmetry at an interface Although already discussed, continuous translation symmetry in one direction should be mentioned here. The reason for that is the consequence of index guiding in which the parallel component $k_\parallel$ of the wavevector at an interface is conserved. It will be explained in further detail in the section 2.3.

Discrete translational symmetry This symmetry is of great importance as the fundamental basis for the Bloch theorem and the Bloch states. It will be discussed in section 2.4.

2.3 Index Guiding

At an interface between two materials of different refractive index a phenomenon called total internal reflection can occur. It is well understood from a geometrical optics perspective as Snell's law,

$$n_1 \sin\theta_1 = n_2 \sin\theta_2.$$

Here, $n_1 = \sqrt{\varepsilon_1}, n_2 = \sqrt{\varepsilon_2}$ are the refractive indices of the first resp. the second material, θ_1 is the incident angle of a light ray with respect to the interface normal and θ_2 is the refracted angle in the second medium, also with respect to the normal axis.
Assume $n_1 > n_2$. In this case there exists a critical angle θ_c such that

$$\frac{n_1}{n_2} \sin\theta_c = 1.$$

For any incident angle $\theta_1 > \theta_c$ Snell's law has no real solution for θ_2 any more. The wave is interpreted as fully reflected.

Snell's law is deduced from ray optics which require the wavelength to be much smaller than the system's length scale. In fact, Snell's law is only a consequence of a more general concept called index guiding, arising due to the translational symmetry at the interface. This concept is valid beyond the scope of ray optics.
Consider a flat surface between the two materials. Along this interface the system has a translation symmetry such that the wavevector component $k_\parallel$ parallel to the interface is conserved. $\mathbf{k}$ of the incident ray splits up in $k_\parallel = |\mathbf{k}| \sin\theta_1$ and $k_\perp = |\mathbf{k}| \cos\theta$ where $|\mathbf{k}| = n_1\omega/c$. By requiring $k_\parallel(n_1) = k_\parallel(n_2)$ due to conservation of ω and inserting $|\mathbf{k}_1|, |\mathbf{k}_2|$, Snell's law is directly obtained.

To further investigate the solutions of Maxwell's equations consider modes far from the interface in the low index medium, n_2. They resemble modes within infinite media with

$$\omega = \frac{c}{n_2}\sqrt{k_\parallel + k_\perp^2}. \tag{2.9}$$

For a given $k_\parallel$ there exists a mode with ω for any frequency above $\omega = k_\parallel c/n_2$. In case of air being the low refractive index medium this is shown in the band diagram Fig. 2.1 for frequencies above the SOL dispersion. This frequency range is termed as light cone.
Besides the modes extended into the low refractive media there are additional solutions with frequencies below $\omega = k_\parallel c/n_2$. To still satisfy eq. (2.9) the perpendicular component has to be imaginary, $k_\perp = \pm i\sqrt{k_\parallel^2 - \varepsilon\frac{\omega^2}{c^2}}$. This means those modes, being extended in the high refractive medium, are evanescent in the low refractive material. In the glass slab example in Fig. 2.1, those are the discrete bands $\omega_n(k_\parallel)$. For larger wavevectors the number of bands increases and approaches the ray optics limit of total internally reflected modes.

2.4 Bloch Theorem for Periodic Media

For the topic of this thesis the most important symmetry is the invariance under discrete translations. Such system are referred to as photonic crystals, in analogy to crystals of atoms or molecules.
A crystal is only translation-invariant under certain shift vectors $\mathbf{a}$. For each dimension one can choose one minimal vector $\mathbf{a}_i$ such that every other translation vector is a superposition of $\mathbf{a}_1, \mathbf{a}_2$ and $\mathbf{a}_3$ with integral coefficients,

$$\varepsilon(\mathbf{r} + i\mathbf{a}_1 + j\mathbf{a}_2 + k\mathbf{a}_3) = \varepsilon(\mathbf{r}), \quad \text{for } i, j, k \in \mathbb{Z}. \tag{2.10}$$

The vectors $\mathbf{a}_1, \mathbf{a}_2, \mathbf{a}_3$ are called primitive lattice vectors while the term lattice constant refers to their lengths a_1, a_2, a_3. They do not have to be orthogonal necessarily but it's often convenient to choose different basis vectors for the crystal than for the lattice to achieve a nice geometric property like equal sized lattice constants or orthogonality. The difference between the lattice and a crystal structure is explained in the following.

A mathematical lattice, also denoted as Bravais lattice, only describes the translational invariance of a system. When steping over one spatial period the system looks the same as before. But the lattice does not describe how the system looks like within this period. That's where the crystal basis comes in. The crystal basis describes the content of a unit cell, the volume spanned

by the lattice vectors. A crystal structure is then formed by the lattice and the crystal basis. As an example consider the so called honeycomb lattice which is actually a crystal. The underlying periodicity is given by a trigonal lattice depicted in Fig. 2.2(a). The crystal basis can be anything but it needs at least two units to result in the honeycomb structure. The units chosen in figure 2.2(b) are black circles which will be repeated at every point of the underlying lattice. Often the term honeycomb lattice is used to describe a physical model in which one implicitly assumes the usage of two elementary units and only specifies the kind of unit. For instance, graphene is a honeycomb lattice of carbon atoms.

In general, an operation is a symmetry of the system only if the corresponding symmetry operator and the operator $\hat{\Theta}$ from eq. (2.6) commute. Whenever two operators commute one can construct common eigenstates, and, determining the eigenstates of the symmetry operator is often easier. In case of discrete translation symmetry these eigenfunctions are plane waves, but arbitrary wave vectors do not classify the modes uniquely. Consider the translation operation along one direction, along $\mathbf{R} = j\mathbf{a}_1$. The according eigenfunction is $e^{i\mathbf{k}\cdot\mathbf{r}}$ with eigenvalue $e^{i\mathbf{k}\cdot j\mathbf{a}_1}$. But shifting $\mathbf{k}$ by a vector $\mathbf{k}'$ such that $\mathbf{k}' \cdot \mathbf{a}_1 = 2\pi l, l \in \mathbb{Z}$ results in the same eigenvalue. All modes with this eigenvalue form a degenerate set of modes which share the property of being invariant under the operation $\mathbf{k} \to \mathbf{k} + \mathbf{k}'$. The shifts in $\mathbf{k}$-space are integral multiples of the reciprocal lattice vector $\mathbf{b}_1$ satisfying $\mathbf{b}_1 \cdot \mathbf{a}_1 = 2\pi$.
Considering all lattice vectors the reciprocal lattice vectors are formed by

$$\mathbf{b}_i = \pi\epsilon_{ijk}\frac{\mathbf{a}_j \times \mathbf{a}_k}{\mathbf{a}_1 \cdot (\mathbf{a}_2 \times \mathbf{a}_3)}, \tag{2.11}$$

where ϵ_{ijk} denotes the fully antisymmetric tensor.

As a consequence a mode $\mathbf{H}_\mathbf{k}(\mathbf{r})$ classified by $\mathbf{k}$ can be expanded as a Fourier series. Separating the eigenfunction from the expansion results in the important Bloch theorem:
Any solution to the eigenvalue problem (2.6) of a periodic dielectric function $\varepsilon(\mathbf{r})$ with periodicity $\mathbf{R}$ consists of a function $\mathbf{u}(\mathbf{r})$ with the same underlying periodicity multiplied by a plane wave of different periodicity,

$$\mathbf{H}_\mathbf{k}(\mathbf{r}) = e^{i\mathbf{k}\mathbf{r}}\mathbf{u}_\mathbf{k}(\mathbf{r}), \quad \text{with} \quad \mathbf{u}_\mathbf{k}(\mathbf{r}+\mathbf{R}) = \mathbf{u}_\mathbf{k}(\mathbf{r}). \tag{2.12}$$

It follows that a mode is in general not invariant under a lattice step since it changes the phase by e^{ika}. A shift in the reciprocal space by $\mathbf{G} = l\mathbf{b}_1 + m\mathbf{b}_2 + n\mathbf{b}_3$ leaves the field unchanged, so the modes $\mathbf{H}_\mathbf{k}$ and $\mathbf{H}_{\mathbf{k}+\mathbf{G}}$ are physically equivalent. Thus, the dispersion relation $\omega(\mathbf{k})$ must obey the same characteristic. To determine the complete dispersion relation it is therefore sufficient

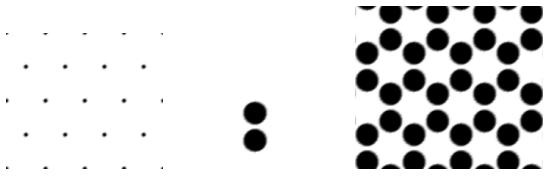

(a) (b) (c)

Figure 2.2: (a) Trigonal resp. hexagonal lattice points (b) Crystal basis of a honeycomb structure of black circles (c) Placing the crystal basis repeatedly at each lattice point results in the honeycomb structure.

to consider only the so called Brillouin zone, the volume of non-redundant $\mathbf{k}$'s in the reciprocal space. The exact shape of the Brillouin zone depends on the lattice but, examplarily, for a one-dimensional lattice of period a the Brillouin zone ranges from $-\pi/a$ to π/a.

Requiring the solution of the electromagnetic eigenproblem (2.6) to be a Bloch state for a certain wave vector $\mathbf{k}$, the problem translates into

$$\hat{\Theta}_{\mathbf{k}}\mathbf{u}_{\mathbf{k}} = \left(\frac{\omega(\mathbf{k})}{c}\right)^2 \mathbf{u}_{\mathbf{k}}(\mathbf{r}), \quad \text{with} \quad \hat{\Theta}_{\mathbf{k}} = (i\mathbf{k}+\nabla)\times\frac{1}{\varepsilon(\mathbf{r})}(i\mathbf{k}+\nabla)\times \tag{2.13}$$

which has to be solved for $\mathbf{u}_{\mathbf{k}}(\mathbf{r})$. The introduced operator is again Hermitian and depends on $\mathbf{k}$.
Due to the required spatial periodicity of $\mathbf{u}_{\mathbf{k}}(\mathbf{r})$ the new eigenvalue problem (2.13) is restricted to the unit cell. Since this is a finite volume one expects the eigenvalues to be discrete, in analogy to a cavity. So for a given Bloch wave vector, the modes can be labeled by a band number n, in increasing order of their discretely spaced frequencies $\omega_n(\mathbf{k})$. For a given band the wave vector enters as a continuous parameter, so $\omega_n(\mathbf{k})$ is a family of functions, characteristic for the photonic crystal of interest. This set of functions is termed the band structure of the Photonic Crystal (PhC).

As mentioned previously, rotational symmetry induces additional redundancy in the dispersion relation. In two dimensions the square lattice is invariant under rotations by 90° while the trigonal lattice has a six-fold rotation axis which is why it is also often called the hexagonal lattice. In two dimensions trigonal and hexagonal denote the same symmetry but, extending to the third dimension, three-fold rotational axis without including six-fold rotational symmetry can occur. Those lattices are called rhombohedral.
For the band structure, rotation symmetry allows to reduce the Brillouin zone since the rotated eigenstate with wave vector $\mathcal{R}\mathbf{k}$ and the original eigenstate share the same eigenvalue $\omega_n(\mathcal{R}\mathbf{k}) = \omega_n(\mathbf{k})$. So a four-fold rotational symmetry axis allows to reduce the volume in $\mathbf{k}$-space by a factor of four and still keeping the full information about the band diagram. In the same way, the Brillouin zone of a hexagonal crystal allows to be reduced by a factor of six.
In analogy to rotations, reflection and inversion operations can be studied and, whenever the crystal obeys such a symmetry, the band structure $\omega_n(\mathbf{k})$ is symmetric as well. Those symmetry operations are called the point group of the crystal.
Considering all point groups the remaining volume in $\mathbf{k}$-space having non-redundant information about the frequency $\omega(\mathbf{k})$ is called the irreducible Brillouin zone. An example is given by the crystal based on the square lattice in Fig. 2.3. The associated Brillouin zone in the reciprocal space, depicted in Fig. 2.3, can be reduced by a factor of eight.
It is important to mention that, in order to have the same irreducible zone for the PhC and the underlying lattice, the crystal basis must exhibit the same point group symmetries within the unit cell. If the unit cell breaks a symmetry of the lattice the irreducible zone is extended.

2.5 Phenomenology of Band Gaps

A band gap is a frequency range in the spectrum for which the eigenvalue problem (2.6) resp. (2.13) has no solution. For a conceptual crystal, being extended infinitely in space, electromagnetic modes with such frequencies can not exist. In reality a crystal always have a finite extent such that modes with band gap frequency do exist but with exponentially decaying intensity

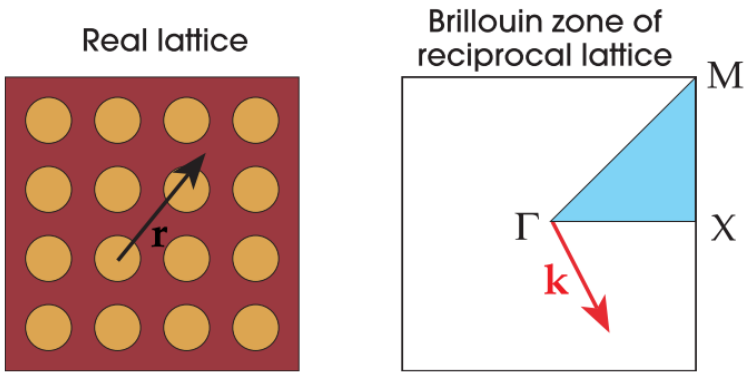

Figure 2.3: Photonic crystal of circles on a square lattice, together with the irreducible Brillouin zone in the reciprocal space. Special points in the Brillouin zone have lattice specific names by convention. [10, p. 38]

from the surface into to the crystal bulk.

How do band gaps arise? A one dimensional crystal, shown in Fig. 2.4(b), is used to explain the physical origin from a variational approach. The layers of same material, colored in green and blue, have a lattice constant a. Initially, assume that those layers have the same permittivity ε such that the structure is, in fact, a homogeneous dielectric medium. The dispersion relation is simply the light line,

$$\omega(k) = \frac{ck}{\sqrt{\varepsilon}}.$$

Instead of using the continuous labeling of the modes by the wave vector k we can artificially

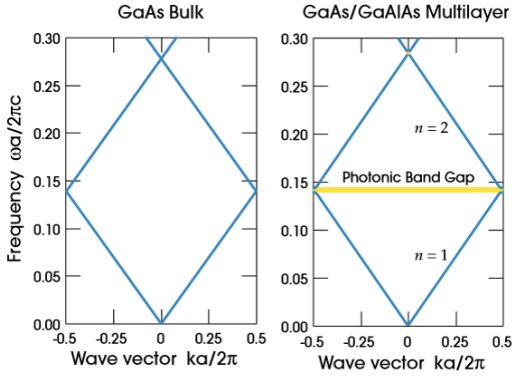

(a)

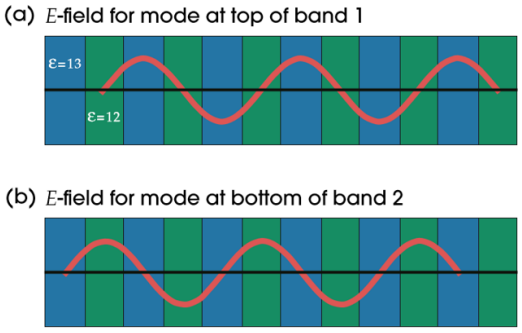

(b)

Figure 2.4: (a) Band diagram before and after perturbation of ε in the green layers of the crystal slab in Fig. (b). Properties of GaAs and GaAlAs are applied to compute the bands. (b) Electric field of the first band at the boundary of the Brillouin zone $k = 0.52\pi/a$, and the field of the second band at the same k [10, p. 48]

introduce a band number n such that $k = k' + na/2\pi$ with a Bloch wave vector $-\pi/a \leq k' < \pi/a$ from the Brillouin zone. This is called back-folding to the first Brillouin zone and the according band diagram is given on the left-hand plot of Fig. 2.4(a). At the boundary $k = \pi a$ of this artificial zone the mode has twice the periodicity of the lattice. The according mode is shown in Fig. 2.4(b), once with its energy concentrated in the blue region and, once with the energy in the green region. Physically, the two situations are identical since they are equal in energy and the partitioning in blue and green regions is completely artificial.

By applying a small perturbation to ε, let's say decreasing it in the green cells, the blue region become distinct from a electromagnetic point of view. Having a larger fraction of its energy concentrated in the high-ε regions the mode in the upper Fig. 2.4(b) shifts towards lower frequencies. In contrast, the energy density in the low-ε regions is larger for the second mode than for the first one. This leads to a shift towards higher frequencies.
This is due to [10, p. 18]

$$\frac{\Delta\omega}{\omega} \approx -\frac{\Delta n}{n} \cdot (\text{fraction of } \int \varepsilon |\mathbf{E}|^2 \text{ in the perturbed regions}),$$

derived from perturbation theory applied to the Hermitian eigenproblem. Here, n is the refractive index.
As a result the initial mode splits up in two, with different frequency and energy. This is represented in the band diagram as a gap, left Fig. in 2.4(a), meaning that a state with energy in between does not exist.

2.6 Scale Invariance of Maxwell's Equation

The eigenvalue equation derived from Maxwell's equation (2.6) does not exhibit a characteristic length scale - it is scale invariant. As a consequence, the system can be contracted or expanded while keeping the same characteristics of the PhC up to scaling factor. In practice this scaling is limited to the frequency range in which our assumptions about ε are valid.
By compressing or expanding the system of interest with a scaling factor s, inserting the new dielectric function $\varepsilon(\mathbf{r})$ into eq. (2.6) and make a change in variables $\mathbf{r}' = s\mathbf{r}$, we find that the new mode profile $\mathbf{H}'(\mathbf{r}')$ is identical to the original one and that the frequency changes by $\omega' = \omega/s$. Besides length scaling, substituting the dielectric function by $\varepsilon(\mathbf{r})' = \varepsilon(\mathbf{r})$ changes the frequency in the same way as before. The mode profile remains unchanged.

Especially the second scaling property has an important consequence for photonic crystals. Suppose the crystal consists of two media with ε_1 and ε_2. The band diagram is determined by the distribution of $\varepsilon(\mathbf{r})$ in the unit cell. Due to the scaling not the absolute values of ε_1 and ε_2 are important but rather the so called dielectric constrast, $\varepsilon_1/\varepsilon_2$. If the band structure of a given PhC should be kept while replacing one medium, the second medium has to be replaced as well. Considering a PhC of a single material with ε_1, in which vacuum plays the role of ε_2, using a different material requires to recompute the full band structure.

2.7 Units

The scaling properties allow us to set a characteristic length and express all quantities relative to it. Additionally, by setting $c = 1$ all quantities become dimensionless. For a PhC the lattice

constant may be a good choice for such a characteristic length scale. For example a time period of $T = 0.4$ refers to $0.4 \cdot a/c$. By inserting a and c in SI units the period in seconds is computed. A wavelength may be given by 5.5 which actually means $\lambda = 5.5a$. Throughout this thesis frequencies will be given without explicit unit, so $f = 0.45$ is meant to be $f = 0.45\ c/a$. The same is used for the angular frequency, where $\omega = 0.45$ is $\omega = 0.45\ 2\pi c/a$. Spatial quantities will always use the reference quantity explicitly, for example in $r = 0.2a$.

In the following, relative units are used for numerical studies. For fabrication the characteristic length is set by an experimental constraint, e.g. designing the structure for a frequency of 1 THz.

2.8 Requirements for Accelerating Particles

A charged particle passing through an electromagnetic field is subjected to the Lorentz force,

$$\boldsymbol{F} = q(\boldsymbol{E} + c\boldsymbol{\beta} \times \boldsymbol{B})$$

where q is the charge of the particle and β its velocity in natural units. In order to accelerate particles along their trajectory significant components from the E-field are necessary since the magnetic field does not do work.
In general, the net force, acting on a particle in an oscillating field, will average to zero over multiple periods. Only in the case where the particle travels with the same velocity as the EM-field's phase, the received force is constant and significant over several periods. This is called the synchronicity condition,

$$v_{ph} = \beta \tag{2.14}$$

where $v_{ph} = \omega/k$ is the phase velocity.

3 Choice of Material

In most cases, band gaps increase in size with increasing index contrast (as an example see [10, p. 244ff]). On the other hand many high-ε materials require elaborate fabrication techniques, like photo lithography used for silicon.
To keep fabrication efforts simple and to explore a new technology, direct laser writing in fused silica is used. The two step method uses the focal spot of tabletop femtosecond laser to sample the glass substrate and changes its properties such that exposed regions are dissolvable by hydrogen fluoride acid (HF). A detailed description is given in chapter 6.

3.1 Optical Properties of Glass

Two important assumptions were made on ε to develop the theory about photonic bands. First, the absorption coefficient is sufficiently low that the material can be treated as transparent, having zero absorption in the spectrum of interest. Second, ε does not depend on the frequency ω. For the general complex refractive index $n(\omega) = \sqrt{\varepsilon(\omega)}$ this means $n(\omega) = n_r(\omega) + in_i(\omega) \approx n_r$.
To validate this prerequisite for fused silica in the terahertz regime, its optical properties are shown in Fig. 3.1 resp. Fig. 3.2. Kitamura et al. [11] reviewed studies reporting the real and the imaginary parts of $n(\omega)$ over a broad spectrum ranging from 30 nm to 1000 μm. This includes also the terahertz regime which, in terms of wavelength, spans roughly from 30 µm to 1000 µm. For the assumption of constant ε the current work is limited to the range from 100 µm to 500 µm in which the refractive index is given by $n = 1.950 \pm 0.003$. The deviation by 0.17 % is accepted as tolerance.
Further, the range is far from any absorption edge in Fig. 3.2. In fact, the imaginary part $n_i(\omega)$ varies between 0.52×10^{-3} at 0.3 THz and 0.011 at 2.5 THz [12]. The intensity of an electromagnetic wave spatially decays by $I \propto e^{-2n_i\omega/cx}$. For example, at 1 THz the absorption index is $n_i = 4 \times 10^{-3}$ such that the intensity drops to $1/e$ over a distance of 3.7 cm. For long waveguides this decay is large. For a proof of concept model it is acceptable to assume $n_i \approx 0$.
However, the true complex refractive index can significantly be affected by the manufacturing process of the fused silica glass, crystallinity, impurities, point defects, inclusions and bubbles [11]. For this reason the mentioned values are only approximately valid. In case of an experiment which relies on high accuracy in both refractive and absorption index it is recommended to determine them independently or, if provided, rely on information by the manufacturers.

3.2 3D Printable polymers

Considering the absorption index n_i polymers may be advantageous in comparison with fused silica. Busch et al. [13] characterized five typical 3D printable materials and, additionally, High Density Polyethylene (HDPE) and Polypropylene (PP) in the frequency range from 0.2 THz to 1.4 THz. Within the uncertainty of the conducted experiment, the last two polymers have vanishing absorption coefficient α resp. absorption index n_i. Unfortunately, HDPE and PP are poorly printable due to their softness, the high temperature expansion coefficient and unclear melting point. Under the 3D printables polystyrene has the highest terahertz transparency, with

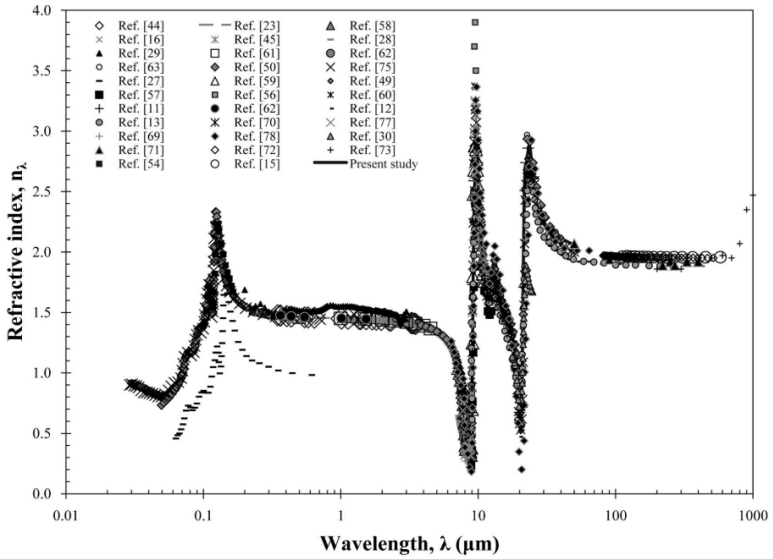

Figure 3.1: Refractive Index $n(\lambda)$ of fused silica glass spanning from UV up to the THz frequencies [11]. This is the real part $n_r(\omega)$ of the complex refractive index $n = n_r + in_i$ with its dependence expressed in terms of the vacuum wavelength.

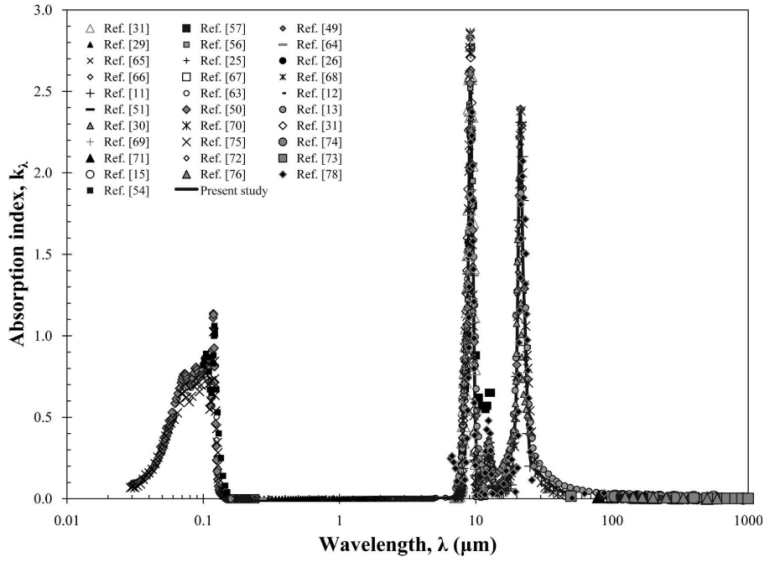

Figure 3.2: Imaginary part of the complex refractive index as absorption index, $n_i = k(\lambda)$, for fused silica glass [11]. Strong absorption edges are observed below 0.1 µm, at 9 µm, 12 µm and 23 µm.

maximal $\alpha = 5\,\mathrm{cm}^{-1}$ at 1.5 THz.

On the other hand, polymers have a lower refractive index which is reduces the occurrence of large band gaps. For instance, for PP and HDPE $n_r = 1.5$ resp. $n_r = 1.53$ were measured, remaining constant over the investigated frequency range.

Furthermore, radiation damage for polymers is an additional concern for particle accelerator application. For fused silica beam-induced damage due to passing relativistic electrons is expected to be lower.
Heating by incident high power THz pulse is an additional figure of merit that has not been answered yet, neither for polymers nor for fused silica.

To study the new fabrication process for fused silica and due to the known radiation hardness at optical frequencies, fused silica was chosen as medium for the structure.

4 Band Structure of a Fused Silica Woodpile at Terahertz Frequency

Three dimensional photonic crystal structures provide ability to guide the laser to different sections in a fully integrated accelerator on a chip [8, 15]. If such a structure obeys a complete band gap it allows to introduce mode confining defects in all directions. This is beneficial especially considering guiding laser pulses to different sections in the particle channel.

The woodpile structure shown in Fig. 4.1(a) is such a three dimensional crystal, first studied by Cowan [6] for the application to particle acceleration. It consists of rods with rectangular cross section which are arranged in regularly manner. Within a layer the rods of width w and height h are parallel to each other, with a distance of a between them. Along the vertical axis four such layers are stacked but shifted and rotated with respect to each other. The rods of the second layer are perpendicular to the ones from the first layer, while the third layer is shifted by a half period $a/2$. The last layer is also shifted but additionally rotated by 90° like the second layer.

One intuitive way to choose an orthogonal basis for the lattice is

$$\mathbf{a}_1 = a\hat{\mathbf{x}}, \quad \mathbf{a}_2 = a\hat{\mathbf{y}}, \quad \mathbf{a}_3 = c\hat{\mathbf{z}}$$

where $\hat{\mathbf{x}}, \hat{\mathbf{y}}, \hat{\mathbf{z}}$ are the unit vectors of the coordinate system in figure 4.1(a). The content of the unit cell for such a choice of lattice vectors is shown in 4.1(b). Here, one observes that shifting the origin of the unit cell by $\frac{1}{2}\mathbf{a}_1 + \frac{1}{2}\mathbf{a}_2 + \frac{1}{2}\mathbf{a}_3$ leads to the same cell content. This implies an additional translational symmetry, which corresponds to the body-centered tetragonal crystal.

In section 2.5 it was observed that a band gap opens up at the Brillouin zone boundary $|\mathbf{k}| = \pi/a$ for an arbitrary variation in ε. Here, only a one-dimensional crystal was studied. Conceptually, one could expect to find the same property in three dimensions, if the edge of the Brillouin zone had the same magnitude $|\mathbf{k}|$ in all directions [10, p. 99]. However, since such a lattice does not exist, the dielectric contrast has to compensate the mismatch of the Brillouin zone shape to form a complete band gap. This compensation is attained with lower contrast if

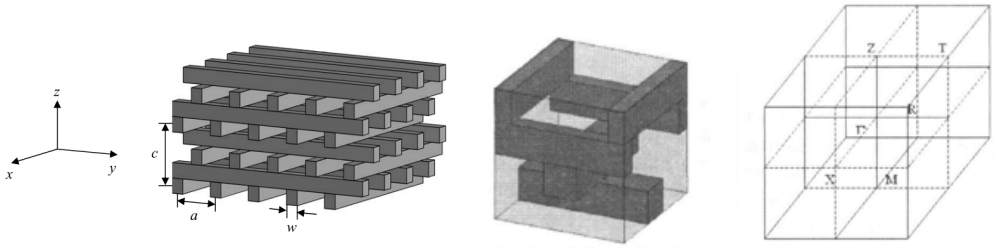

(a) (b) (c)

Figure 4.1: (a) Woodpile structure consisting of rods with rectangular cross section [6] (b) body centered tetragonal unit cell and (c) the corresponding Brillouin zone [14].

the Brillouin zone is nearly spherical which is the case for the face-centered cubic crystal (FCC). An illustrative explanation for this reasoning is given in appendix B.

Applied to the woodpile it is desired to modify the parameters such that it has a FCC symmetry. Choosing different lattice vectors for the woodpile allows us to describe it as a face-centered tetragonal structure. For this purpose, consider the basis vectors

$$\tilde{\mathbf{a}}_1 = \mathbf{a}_1 + \mathbf{a}_2, \quad \tilde{\mathbf{a}}_2 = \mathbf{a}_1 - \mathbf{a}_2, \quad \tilde{\mathbf{a}}_3 = \mathbf{a}_3,$$

with which the crystal lattice is also translation symmetric under

$$\begin{aligned}
\frac{1}{2}(\tilde{\mathbf{a}}_1 + \tilde{\mathbf{a}}_2) &= \mathbf{a}_1, \\
\frac{1}{2}(\tilde{\mathbf{a}}_1 + \tilde{\mathbf{a}}_3) &= \frac{1}{2}(\mathbf{a}_1 + \mathbf{a}_2 + \mathbf{a}_3), \\
\frac{1}{2}(\tilde{\mathbf{a}}_1 + \tilde{\mathbf{a}}_3) &= \frac{1}{2}(\mathbf{a}_1 - \mathbf{a}_2 + \mathbf{a}_3).
\end{aligned}$$

The vectors on the left hand side, in terms of the basis vectors $(1/2, 1/2, 0), (1/2, 0, 1/2), (0, 1/2, 1/2)$, reflect the lattice points in a face-centered tetragonal unit cell.

The desired face-centered cubic crystal lattice is a special case of the face-centered tetragonal one, in which not only $\tilde{\mathbf{a}}_1$ and $\tilde{\mathbf{a}}_2$ have equal length but all three basis vectors, $|\tilde{\mathbf{a}}_1| = |\tilde{\mathbf{a}}_2| = |\tilde{\mathbf{a}}_3|$. As $|\tilde{\mathbf{a}}_3| = |\mathbf{a}_3| = c$ and $|\tilde{\mathbf{a}}_2| = |\tilde{\mathbf{a}}_1| = |\mathbf{a}_1 + \mathbf{a}_2| = \sqrt{2}a$, it is required that

$$\sqrt{2}a = c. \tag{4.1}$$

With this constraint, the crystal most likely exhibits a complete band gap.

Because of the symmetries of the woodpile unit cell the irreducible Brillouin zone reduces to the volume enclosed by the indicated points in Fig. 4.1(c) [14]. In terms of the reciprocal lattice vectors

$$\mathbf{b}_1 = \frac{2\pi}{a}\hat{\mathbf{x}}, \quad \mathbf{b}_2 = \frac{2\pi}{a}\hat{\mathbf{y}}, \quad \mathbf{b}_3 = \frac{2\pi}{\sqrt{2}a}\hat{\mathbf{z}},$$

those are

$$\begin{aligned}
\Gamma &= (0, 0, 0), & X &= (1/2, 0, 0), \\
M &= (1/2, 1/2, 0), & R &= (1/2, 1/2, 1/2), \\
Z &= (0, 0, 1/2), & T &= (0, 1/2, 1/2).
\end{aligned}$$

4.1 Band Diagram by Plane Wave Method

Fully-vectorial eigenmodes were computed by preconditioned conjugate-gradient minimization of the block Rayleigh quotient in a planewave basis, using the freely available software package MIT Photonic Bands (MPB) [16]. In order to define the geometry within the software the intuitive unit cell from Fig. 4.1(b) was used. The only remaining free geometrical parameter is the rod width w. It was varied between $w = 0.2a$ and $w = 0.6a$ in steps of $0.05a$ in order to cover a range of different sizes. The resulting band diagram for $w = 0.25a$ is shown in Fig. 4.2. The

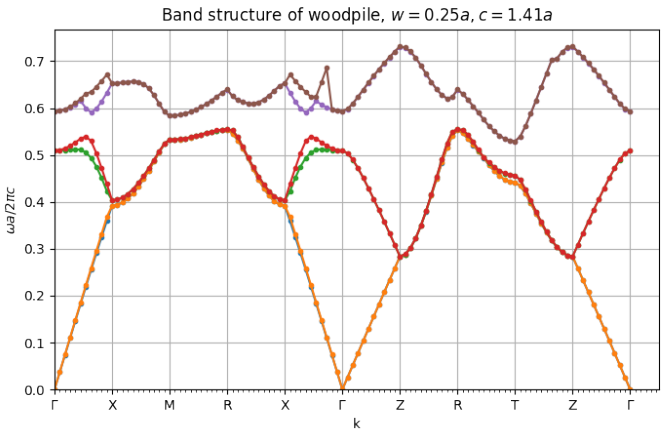

Figure 4.2: Band diagram of a fused silica woodpile with a FCC unit cell, $w = 0.25a, c = 1.41a$, containing the five lowest bands. If there were a band gap it would be expected to be between the third and the fourth band, shown in red and brown. As visible in between the points R and T the lowest frequency of the brown band is below the maximum of the red band.

labels on the x-axis are the boundaries of the irreducible Brillouin zone.

Between $f = 0.56$ and $f = 0.58$ the structure would exhibit a complete band gap if the brown air band did not drop down to $f = 0.53$ at the T-point. By increasing the row width the minimum of the brown band shifted to higher frequencies first. But with further increase beyond $w = 0.35a$ it drops without having passed the maximum of the red band.
To exhibit a complete band gap in three dimensions, the woodpile crystal requires a refractive index above 1.9 [17]. For a significant band gap size $n = 1.95$ is not sufficient.

4.2 Band diagram by FDTD Simulation

To verify the previous band structure result simulations were performed with the Finite-difference time domain (FTDT) method [18], using the freely available software package MIT Electromagnetic Equation Propagation (MEEP) [19]. A broad Gaussian pulse from a point source inside the unit cell excites the structure. It is important to not place the source in a symmetry center and choose a random polarization in order to excite all kinds of modes. After the source has turned off, resonances remain inside the geometry and are analyzed by harmonic inversion [20]. Here, a pulse centered at $f = 0.3, \Delta f = 1.8$ is used. The field is analyzed for 300 a/c time units after the source has turned off. The reference unit size a was discretrized with 25 steps, corresponding to $\Delta x = 0.04a$ on the computational grid.
The resulting FTDT based band diagram, Fig. 4.3, matches the previous one very well, Fig.4.2, and exhibits the same band characteristic in the range from R to T.

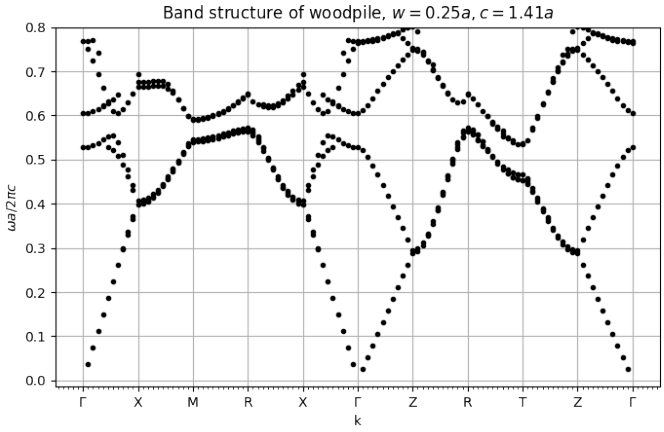

Figure 4.3: The five lowest bands of a fused silica woodpile with an FCC unit cell, $w = 0.25a, c = 1.41a$, computed with the FTDT method. The band diagram matches the one from frequency domain computations, Fig.4.2. If there were a band gap it would be expected to be between the third and the fourth band.

5 Two Dimensional Photonic band gap structure

Because of the lack of a 3D band gap for omnidirectional guidance, a new approach is undertaken to attain guidance along a single direction. A transverse band gap design is studied for this purpose.
Four steps are taken to approach the 2D photonic band gap structure of our interest.
In the first step the band structure of a trigonal photonic crystal with a single glass cylinder at each lattice site is investigated. Secondly, the defect created by removing a single cylinder confines a single state. The crystal is optimized for confining the light of this mode. As a third step the finite extent of a real structures is taken into account but still restricted to two dimensions. Finally the overall 3D geometry, including the mounting of the glass rods, is investigated with respect to its supported electromagnetic modes.

The previous statement of a favored nearly spherical Brillouin zone for a complete band gap translates in two dimensions to a Brillouin zone being nearly circular. With its hexagonal Brillouin zone the trigonal lattice favours a complete band gap.
Throughout this chapter, the investigation of band structures is done with the frequency-domain eigensolver MPB. In the following the lattice constant a will always be used as the reference size for the units. The periodic plane, is referred to as the xy plane while the direction of the cylinder axis is the third dimension, denoted as z. With respect to the desired particle channel z is also called the longitudinal axis while xy form the transverse plane.

5.1 Trigonal Lattice of Cylinders

The irreducible Brillouin zone of the trigonal lattice is shown in the inlet of Fig. 5.1 where the characteristic points in the two-dimensional **k**-space are

$$\Gamma = \begin{pmatrix} 0 \\ 0 \end{pmatrix}, \quad M = \begin{pmatrix} 0 \\ 1/2 \end{pmatrix}, \quad K = \begin{pmatrix} -1/3 \\ 1/3 \end{pmatrix},$$

in units of $2\pi/a$.
For an initial radius $r = 0.2$ of the glass cylinders with permittivity $\varepsilon = 3.8$ eight TM- and TE-bands were computed. The unit cell was discretized by 64 pixels per lattice constant.

Considering both polarizations the structure does not obey a complete band gap, but limiting only to TM bands, a gap ranging from $f = 0.45$ to $f = 0.55$ is observed between the first and the second band, having a gap-midgap ratio of 19 %. Incident waves with a gap frequency and a E-field polarization along the z axis are reflected from the PhC since they don't excite extended modes. The penetrating field decays exponentially from the surface into the bulk.

By introducing an air defect in the following section a state from the dielectric band - the lower band of the gap - will be lifted into the gap. The field of the defect mode is more strongly confined the larger the gap size is. Therefore, the rod radius r was optimized for maximizing the gap-midgap ratio. At $r = 0.24$ the gap ranges from 0.41 to 0.51 with a size of 22 %.

So far the band diagram only reflects modes propagating inside the crystal plane, with $k_z = 0$. The bands change significantly for propagation along the z axis. The first band for the trigonal lattice is shown in Fig. 5.2(a). As explained in chapter 2.2 the mirror symmetry is broken for $k_z \neq 0$, so a separation into TM and TE polarization does not exist anymore. A hybrid mode is a superposition of TM- and TE-polarization. But for low wave vectors the TM-like fraction of an initially TM-polarized wave still dominates.
Fig. 5.2(b) shows the projected band structure for the trigonal lattice of glass rods. Here, the second band, being TE-like, was removed to examine the TM-like bands 1 and 3. No gap along k_z exists due to the continuity of the crystal along the z-axis. Any wave penetrating the crystal from the cross sectional surface with frequency ω will excite an extended mode in the structure. There exist sets of $(k_\perp, k_z, n)$ such that $\omega = \omega_n(k_\perp, k_z)$. Still, they can not necessarily propagate in any direction because of band gaps in the transverse plane. For a fixed k_z the condition $\omega = \omega_n(k_\perp)$ may not be fulfilled.
For instance, this is the case between the first and the third band in Fig. 5.2(b) around $k_z \approx 0$. The TM-like gap decreases in size towards larger k_z. At $k_z = 0.4$ it vanishes. Above $k_z = 0.6$ a new gap appears and more and more gaps emerge with larger k_z while the bands become flat. This is a characteristic common for all two-dimensional crystals. For large out-of-plane propagation the wavelength becomes small such that the light is trapped inside the high-ε regions due to index-guiding. The overlap of modes between neighboring rods vanishes which leads to decoupled modes and discrete states within a single rod.

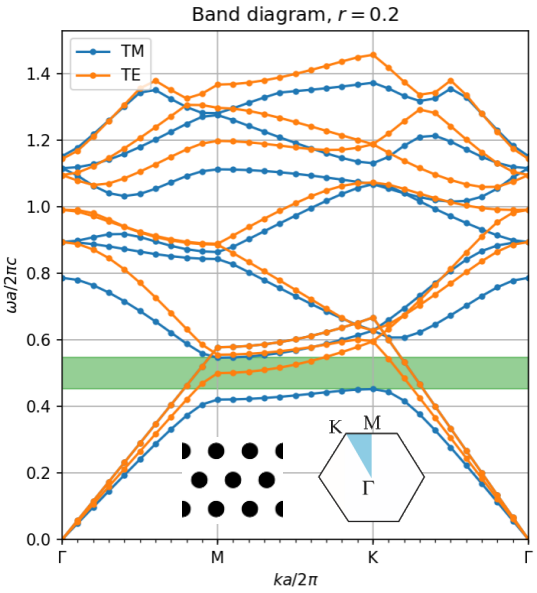

Figure 5.1: Band diagram of the trigonal lattice of cylindrical glass rods ($\varepsilon = 3.8$), shown in the left inset. The right inset shows the Brillouin zone of the trigonal lattice, with the irreducible zone shaded in blue.

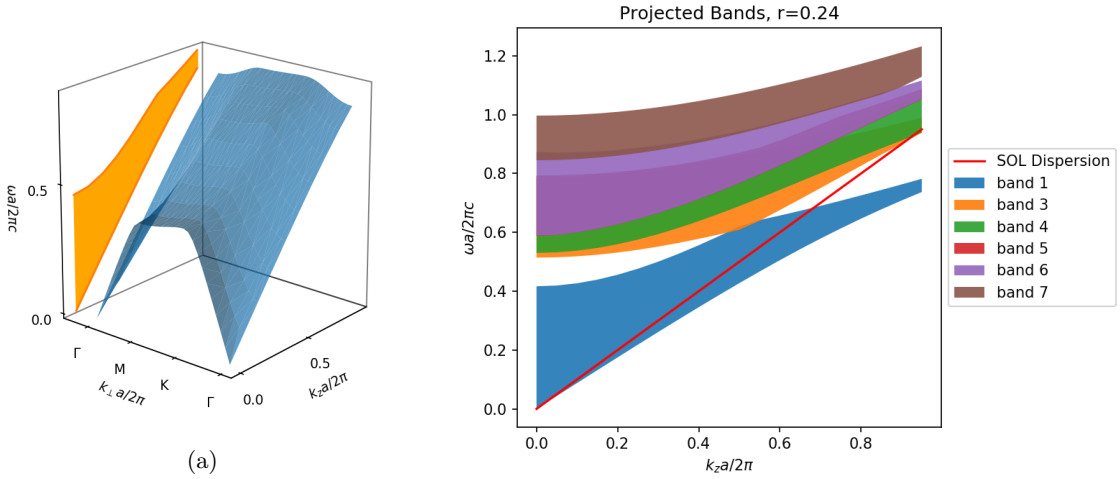

(a) (b)

Figure 5.2: (a) First band of the trigonal lattice including the out-of-plane component k_z. The projection of the transverse components onto $\omega(k_z)$ is added in the background. (b) Projected band diagram $\omega(k_z)$ of the trigonal lattice of rods without the second band.

5.2 Defect Mode of Single Rod Removed

By perturbing a lattice site a single state with frequency inside the gap can be localized. Such a point defect breaks the translational symmetry. The modes can not be decoupled anymore by the in-plane wavevector k but the band gaps remain.
The state induced by the defect decays exponentially into the surrounding crystal. An extended mode with gap frequency is forbidden. The crystal forms reflective walls such that the defect acts like a cavity.
In general, a point defect can occur either due to different material, by variation of refractive index, or by changing the geometry of the unit cell at a lattice site. For our goal to guide electromagnetic modes and particles in the same channel, the type of defect is limited to a hollow core. A nearly cylindrical vacuum channel is desired so one glass rod is removed.
To compute the defect's frequency and field pattern the supercell technique is applied. A finite number of cells from the original lattice is considered into which the defect is introduced. The resulting geometry is by itself treated as a new unit cell of a crystal. By choosing a supercell size of five sites, shown as contour in Fig. 5.3(a), the band structure with the hollow core was computed for the originally trigonal glass lattice. The supercell requires more bands to be computed as intended since extending the computational cell over multiple lattice sites leads to back folding into the first Brillouin zone. This means by doubling the cell size a single band splits up in two, containing redundant information about the mode configurations. In order to cover the full frequency range of the three lowest bands, in which the gap lies, 75 bands are computed for the supercell. The stored electric energy in the core is used to classify the defect mode. Here, the core is artificially defined as the area within the distance of $1.0a$ from the center.
The trapped mode between the TM bands has a frequency of $f = 0.46$ and confines 44 % of the energy in the core. The frequency agrees with the midgap frequency. The normalized field pattern for the longitudinal electric field component E_z in the supercell is shown in figure 5.3(a)

and, additionally, in Fig. 5.3(b) along the center axes.
A variation of r supports the previous statement that the confinement is maximized by a large band gap. Though, the change in stored energy is small. At $r = 0.2$, 42 % confinement was reached.

5.3 Truncated Effectively Two-dimensional Structure

An infinitely extended lattice is an idealized model for a real physical structure. The crystal is truncated at a certain lattice cell number and the truly localized defect mode becomes leaky. The resonance has a non vanishing leakage rate into the PhC. This leakage decreases exponentially with the number of surrounding lattice sites [10, p. 83].
The crystal is truncated such that it keeps the six-fold rotational symmetry of the lattice. The resulting hexagonal shape is shown in Fig. 5.4(a) for $n_{cells} = 5$. Hereby, the number of lattice cells is counted from the core to the outer surface. The decaying mode is described by a complex frequency $\omega = \omega_r - i\omega_i$, where the real part corresponds to the result from the supercell computation. The field decays with $e^{-\omega_i t}$ while the energy decay has the doubled rate $2\omega_i$. The quality factor Q relates the imaginary and the real frequency parts to classify the decay as dimensionless quantity,

$$Q = \frac{\omega_r}{-2\omega_i}. \tag{5.1}$$

It is equivalent to the ratio between the electromagnetic energy U in the cavity and its outgoing power P, weighted by the frequency,

$$Q = \frac{\omega_r U}{P}. \tag{5.2}$$

To study the resonance, FTDT simulations were conducted for varied cell number, ranging from $n_{cells} = 4$ to 10.
A resolution of 20 pixels per unit length is chosen, corresponding to $\Delta x = 0.05$. To satisfy the Courant–Friedrichs–Lewy condition for finite difference methods [21], MEEP uses a time discretization of $\Delta t = 0.5\Delta x$ by default, where the ratio between the temporal and the spatial step size is called the Courant factor. Throughout this work the default Courant factor of 0.5 is kept

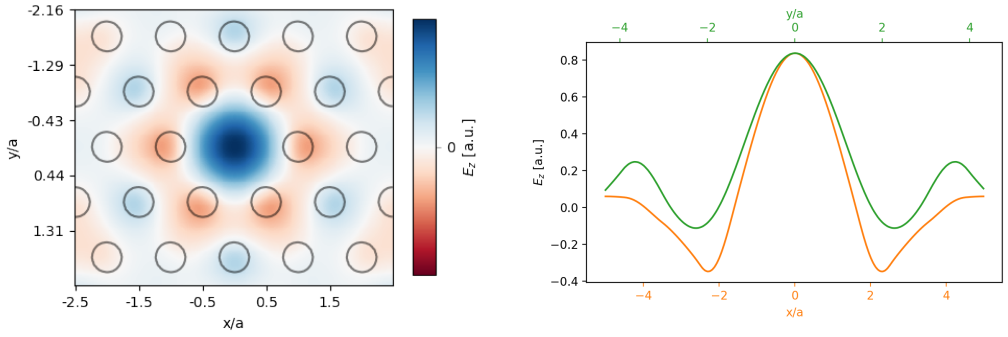

(a) (b)

Figure 5.3: (a) TM Defect mode within super cell computation of five cells. 44 % of the energy is stored inside the defect. (b) E_z field distribution along x and y axis.

for all simulations.

A Gaussian point source placed in the center excites the structure. After the source has turned off, the simulation is continued for 300 additional time units, during which a temporal signal processing of E_z is done by harmonic inversion using filter-diagonalization method [22] at the center point.
Initially, a broad band pulse excitation of $f = 0.46, \Delta f = 0.3$ is applied to investigate whether further resonances occur than the desired one. In table 5.1 the result is listed for five lattice cells. Besides the desired mode at $f = 0.46$ two additional modes were found at 0.41 and 0.53. Considering their Q-factor the energy decays to $e^{-2\pi}$ over 100 and 50 optical periods, respectively. The desired resonance dominates with $Q = 510$.
To get the field pattern the structure is excited with a narrow band source, $f = 0.46, \Delta f = 0.05$. Comparing Fig. 5.4(b) and Fig. 5.3(a) it is concluded that the resonant mode matches the trapped mode very well. On the other hand the field outside the structure is visible.
In Fig. 5.4(b) the relation between Q and n_{cells} is plotted for the desired mode. The confinement increases significantly with n_{cells}, by $Q \propto e^{n_{cells}}$.
As a conclusion even few rods are sufficient to trap the mode between the glass rods in comparison with the model of an infinite crystal. Even 4 rods support a confined state, although its leakage is not neglectable.

frequency	imag. freq.	Q
0.41	-0.0021	97
0.46	-4.5×10^{-4}	510
0.53	-0.0052	51

Table 5.1: Exemplary resonances found by harmonic inversion of the time signal in a 2D truncated crystal with $n_{\text{cells}} = 5$.

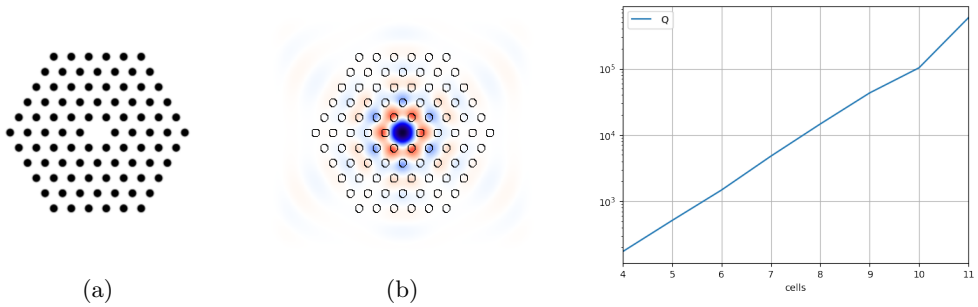

(a) (b) (c)

Figure 5.4: (a) Truncated structure of the trigonal crystal of glass rods. Five lattice sites are used where the number of cells is counted from the center to the outer surface. (b) Field distribution E_z of the desired resonance at $f = 0.46$ (c) Q-factor depending on the number of cells, $Q(n_{cells})$.

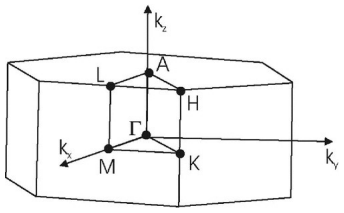

Figure 5.5: Full Brillouin zone of the structure with mounting plates along the z axis.

5.4 Mounted Three Dimensional Cylinders

While a model of vacuum inclusions in a refractive material is practically possible, e.g. air holes in glass, the inverse is not directly possible. At least the rods must be attached to walls at both ends.
For mechanical stability and further tuning of the trapped electromagnetic wave, mounting plates are inserted in regular distance. Here, we assume them to be round in the transverse plane, as shown in Fig. 5.6(d). The design of a truncated crystal is given in Fig. 5.6(a). Three new geometric parameters are introduced, the mounting thickness, the distance between the plates and the number of mountings.
In fact, the new periodic pattern along the longitudinal direction forms a new kind of photonic crystal. Considering the lattice in the transverse plane the structure forms a three dimensional crystal with a linear defect along the cylinder axis. Its Brillouin zone is shown in Fig.5.5. A band gap is not desired as the mode confined in xy should propagate along z.

5.5 Resonances of the Finite Waveguide

In order to keep perturbations to the electromagnetic modes from the unmounted structure small, the distance between the mounting plates l_m is chosen larger than the corresponding free-space wavelength $\lambda = c/f = 2a$. Due to the same reason the thickness d_m should be very small. The initial values are set to $l_m = 5a$ and $d_m = 0.5a$. The number of longitudinal cells in the initial configuration is $n_l = 4$, counted from the center to the exit of the waveguide.
For the aperture of the waveguide at the mounting plates two different sizes were examined, either the size of a single rod or the complete defect size in the crystal plane, Fig. 5.6(f) resp. 5.6(e). First, the small waveguide aperture is considered.

The study of resonant modes is done as before, by exciting the structure with a broad Gaussian pulse of center frequency $f = 0.3$ and width $\Delta f = 0.5$, and analyzing the fields at the point of excitation for a period of 300 units after the source has turned off. To retrieve the pattern of a single resonance, the simulation is repeated with a narrow band source at the resonant frequency. The spatial resolution is chosen as 20 pixels per unit length a.
The source is placed asymmetrically within the hollow core, neither in the center of the mounting plate nor on the z-axis, to examine which modes can be excited with a longitudinal point-like dipole current. The position of the source is visible in the later field pattern.
Two resonant modes were found, table5.2. Compared to the previous results of the 2D case, the confinement is clearly weak. The Q-factor is below 100 for both determined modes. Interestingly, the desired frequency of the band gap does not appear. In addition to narrow band excitations

at $f = 0.19$ and $f = 0.29$ a pulse with band gap frequency is studied. All narrow band excitations have a width of $\Delta f = 0.5$. The lowest frequency mode turns out very noisy and with dipole-like E_z field pattern. The relative amplitude in 5.2 already indicates the low significance compared to the second mode. The field pattern for the $f = 0.292$ resonance is shown in figure 5.7. The peak is located in the center of the transverse plane but losses are significant not only at the mounting, 5.7(b), but E_z also extends through the whole xy plane at the PhC structure. The field is hardly confined in the core. In the longitudinal plane, 5.7(a) and 5.7(c), the field appears to be confined to the center axis. But since the source is still visible the leakage has to be significant.
For the additional narrow band excitation at $f = 0.47$ the remaining source signal dominates the resonance.

Table 5.3 lists the resonances found in a waveguide with large mounting plate aperture. In contrast to the previous result, a mode close to the band gap frequency was found, $f = 0.48$. It also dominates the other resonances in amplitude but decays faster, $Q = 56$. As Fig. 5.8 shows, its longitudinal field leaks less to the surrounding vacuum than the dominating mode from the small aperture waveguide.

The mounting plates introduce a new periodicity along the z-axis. The resonances may be addressed to the bands of the longitudinal crystal structure. Here, the Q-factor is significantly lowered compared to the 2D PhC, but it is not clear whether this is a general phenomenon because of mountings plates. For a general statement different mounting plate parameters have to be studied in future as well as the band structure along the cylinder axis.

frequency	imag. freq.	Q	rel. amplitude
0.20	-0.0012	81	3.5×10^{-7}
0.29	-0.0023	64	3.2×10^{-4}

Table 5.2: Resonant modes of the mounted, three dimensional structure with small aperture at the mounting plates, Fig. 5.6(f). The exciting source has a frequency of $f = 0.3$, $\Delta f = 0.4$. Harmonic inversion was applied for $T = 300$ time steps after the sources turned off.

frequency	imag. freq.	Q	rel. amplitude
0.32	-0.0018	90	2.8×10^{-5}
0.48	-0.0043	56	0.019
0.50	-0.0031	81	1.5×10^{-4}

Table 5.3: Resonant modes of the large aperture waveguide, Fig. 5.6(e). The exciting source has a frequency of $f = 0.3$, $\Delta f = 0.4$. Harmonic inversion was applied for $T = 300$ time steps after the sources turned off.

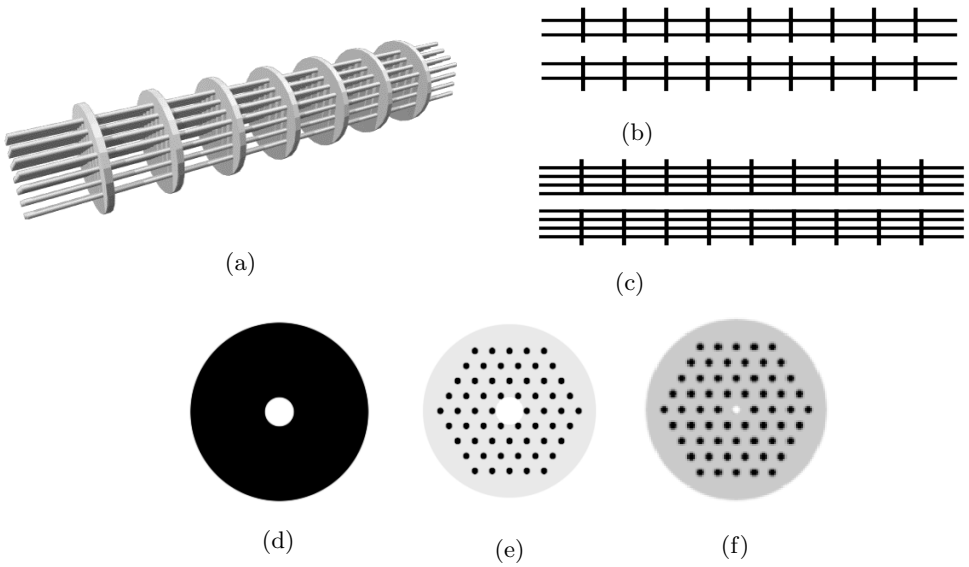

Figure 5.6: (a) Full model of the waveguide with mounting plates (b), (c) cross section of the structure in the xz-plane resp. xy plane . (d) Cross sectional view in the transverse plane at the mounting plates. (e) Transverse plane between the rods with circular plate in the background (f) Alternative aperture in the mounting plate, with the same size as the rods

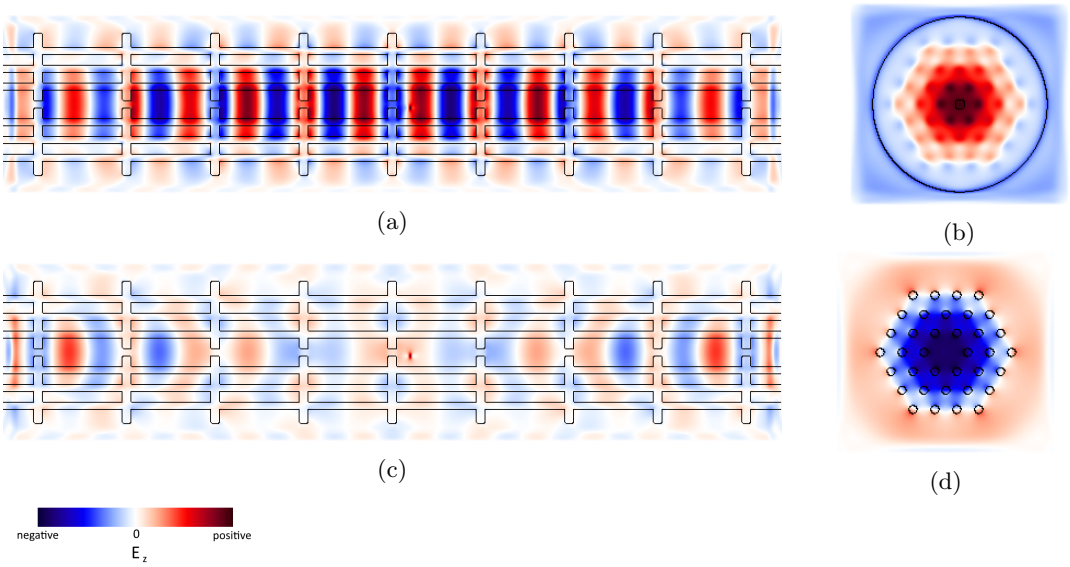

Figure 5.7: Field pattern E_z at $f = 0.29$ for three different cross sections. (a), (c) show the same cross section at two time points shifted by a quarter period, such that the amplitude in the center is maximal resp. minimal. The field strength for both is normalized to the same colormap. In (c) the exciting source is visible in the center. (b) E_z in the transverse plane at the center plate. (d) Transverse cross section between the mounting plates.

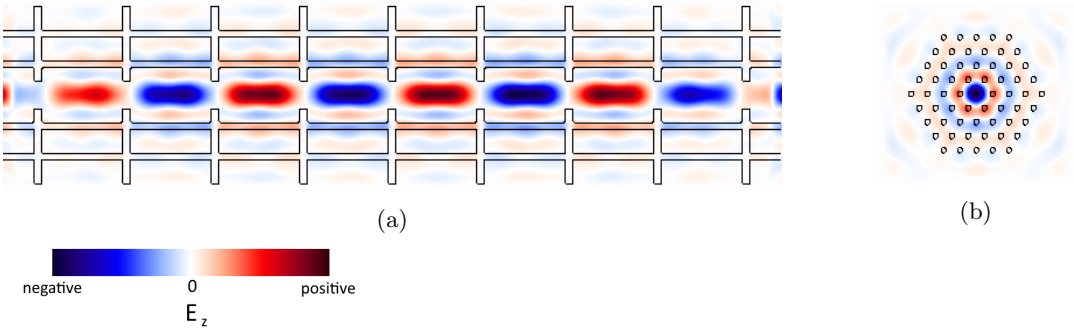

Figure 5.8: Longitudinal field pattern E_z for the waveguide with large aperture in the mounting plates at resonance frequency $f = 0.48$ from table 5.3. (a) Cross section at $x = 0$, showing the on-axis field (b) Transverse plane between the mounting plates.

5.6 Overview of Free Parameters

The full structure has several geometric parameters which affect the propagation of electromagnetic waves inside. They can be assigned to three groups: photonic crystal parameters, defect parameters and mounting parameters. The refractive index is not considered as a free parameter.

Photonic crystal The finite photonic crystal is fully described by the radius r of the glass cylinders and the number of lattice cells n_{cells}. n_{cells} is counted from the hollow core to the outer surface within the xy plane. The lattice constant a is set to unity in all computations as it serves as reference scale.

Defect Parameters As described earlier, there are different ways to introduce a defect. One can either consider the number of removed cells as one parameter, allowing to remove 1 rod, 7 rods, 19 and so on. Or the core can truncate single rods and is described by the defect radius r_D.

Mounting The mounting plates have a finite thickness d_m, a distance of l_m and a finite number of mountings is used. Here, the longitudinal cells n_l are described in the same way as the transverse ones, by counting from the center to the end of the waveguide.
As described above the the aperture is an additional characteristic. If not stated differently, the large aperture is used in the following.

The overall structure length is given by the mounting distance and the longitudinal period, $L = n_l \cdot l_m$. The mounting radius r_m is chosen such that it is always larger than the 2D PhC, $r_m = (n_{cells} + 1)a$. The width w and height h of the crystal in xy plane are given by

$$w = 2(n_{cells}a + r),$$
$$h = 2\left(\frac{\sqrt{3}}{2}n_{cells}a + r\right),$$

where $\sqrt{3}/2a$ is the distance of rod layers along the y axis. The layer height is important for the manufacturing in later sections.

5.7 Energy Gain

For the two modes found above, $f = 0.48$ in the large aperture configuration and $f = 0.29$ in the small aperture waveguide, the relative on-axis energy gain was computed for a test-particle without velocity change. The absolute energy gain depends on the amplitude of the field, but the fields are normalized in the FTDT simulation. Therefore, we can only compare about the energy gain relative to the particle velocity.
In first approximation the energy gain is defined as

$$G = \frac{1}{T}\int_0^T E_z(\mathbf{r}(t), t)dt \tag{5.3}$$

where T is the period of the oscillation and the field acts on an on-axis particle,

$$\mathbf{r}(t) = \mathbf{r}(0, 0, z(t)). \tag{5.4}$$

A particle is placed on the left side of the structure Fig. 5.7(c). While the particle moves with velocity βc along the center axis, $z(t) = z_0 + \beta ct$, the field is integrated. Instead of integrating

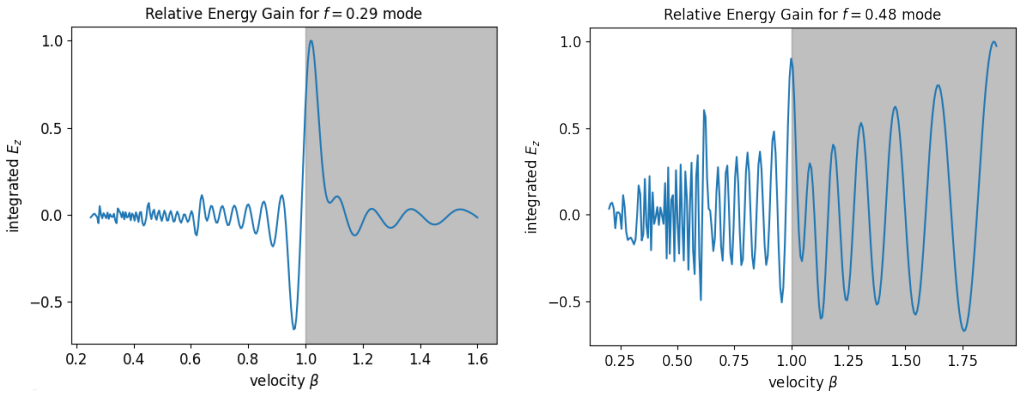

(a) (b)

Figure 5.9: (a) Relation between particle velocity β and energy gain $G(\beta)$, eq. (5.3) , normalized to maximum gain. E_z from Fig. 5.7(c) is used. (b) Same relation $G(\beta)$ for the $f = 0.48$ mode in the large aperture waveguide, Fig. 5.8(a).

only over a single period, the particle is tracked to the end of the structure. The longer the gain is accumulated the higher is the accuracy for a given velocity β. Additionally, accumulating over multiple periods reduces the relevance of the initial start position for the absolute value of the gain. A particle with certain velocity receiving negative gain will still be accelerated if the timing of its arrival is tuned according to the phase match.
For higher precision $E_z(0, 0, z, t)$ is interpolated as well as periodically continued. This allows to track the particle over several cells of the waveguide structure, assuming the mode in 5.7(c) resp. 5.8(a) is periodic along the z-axis. This is a very strong restriction since we know from Bloch's thereom that the electromagnetic state does not necessarily have the same periodicity as the underlying geometric object.

Fig. 5.9 shows the dependence of the gain on particle velocity β. Here, also nonphysical values for β were used, $\beta > 1$, meaning that a hypothetical particle would travel faster than speed of light. Although not realistic, this trick is helpful to understand the phase velocity of those modes.
In principle, both modes support acceleration of relativistic particles, $\beta \leq 1$, as the peaks in the gain $G(\beta)$ illustrate. For the small aperture structure this clearly peak dominates the gain, Fig. 5.9(a). More smaller peaks are observed around $\beta \approx 0.6$ and $\beta \approx 0.45$, but the gain has dropped by a factor of 10 resp. 20. At velocities as low as 0.45 the peak is very weakly pronounced. Particles with $\beta = 0.85$ receive more gain although the gain envelope is not peaked here. One misleading characteristic observed in Fig. 5.7(c) is the presence of the source. It is not clear whether the field pattern represents the eigenmode sufficiently. This may distort the realistic energy gain as well as the restriction to periodicity along the z-axis.
In Fig. 5.9(b), the two envelope peaks are weakly pronounced, comparing them with their neighborhood in velocity space. Additionally, the envelope increases further with $\beta > 1$. This indicates a phase velocity above SOL, meaning that the ideal synchronicity condition can't be satisfied.

The the spatial on-axis field $E_Z(z) = E_z(0, 0, z, t_0)$ is analyzed for a fixed time point by Fourier transformation to $E_z = E_z(k_z)$. The time point t_0 is chosen by maximizing the amplitude. The first mode of interest, Fig. 5.7(a), exhibits wavelength components at $\lambda = 3.13\,\mathrm{a}$ and $\lambda =$

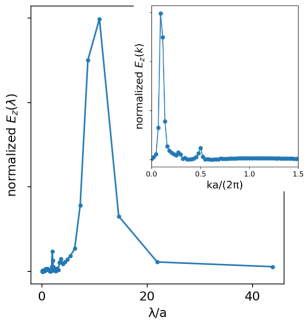

Figure 5.10: Fourier transform of the field pattern $E_z(z) = E_z(0, 0, z, t_0)$ to extract wavelength components. In the inlet the components $E_z(k_z)$ in the **k**-space are plotted. The underlying figure uses the wavelength $\lambda = 2\pi/k$ as the x axis.

8.78 a where the first one dominates the second by factor of 1.5. Taking the frequency into account, the two components travel with a phase velocity of $v_p 0.91\,\mathrm{c}$ and $v_p = 2.56\,\mathrm{c}$. While the second component is not useful for matching the synchronicity condition with a traveling particle, the first one is close to the peak in energy gain $G(\beta)$, Fig. 5.9(a). Further analysis, including uncertainties from computation, are required to get a better understanding of this weak resonance.
The spatial field pattern in the small aperture waveguide with frequency $f = 0.48c/a$ contains predominantly one wavelength component at $\lambda \approx 10a$, Fig.5.10, corresponding to a phase velocity of $5c$. This verifies the previous statement from $G(\beta)$ that the phase velocity is clearly above the desired range of $\beta = v_p$.
As before, the wavelength results require additional work to quantify them more accurately. For an estimation whether the modes fail the synchronicity, the retrieved values are sufficient.

5.8 Transmission through Waveguide

In order to investigate the electromagnetic propagation through a finite structure, transmission simulations are conducted.
The transmitted power through a waveguide, for a certain frequency, is given by the surface integral of the poynting vector over the cross sectional plane,

$$P(\omega) = \mathrm{Re}\,\hat{\mathbf{n}} \int \mathbf{E}(\mathbf{x}, \omega)^* \times \mathbf{H}(\mathbf{x}, \omega) d^2\mathbf{x}, \tag{5.5}$$

where $\mathbf{n}$ is the normal direction of the transverse plane, $\mathbf{E}(\mathbf{x}, \omega)$ and $\mathbf{H}(\mathbf{x}, \omega)$ are the spectral components of the fields. Since the flux resp. the ng vector is not a linear function of the fields it is required to perform the Fourier transformation to $\mathbf{E}(\omega), \mathbf{H}(\omega)$ before taking the integral. In the simulation this is done by accumulating the components from each time step together with the appropriate Fourier phase and compute $P(\omega)$ when the stepping has finished.

For transmission spectra the power needs to be normalized. Here, to different reference flux planes are considered. What does the transmission spectrum look like compared to a hollow core cylinder of glass of the same size? How does the spectrum change while propagating from one point on the axis to the end of the waveguide?

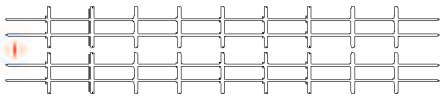

Figure 5.11: Position of the Gaussian source at one end of the structure for flux simulations. The plane at which the transmitted flux is accumulated is placed on the opposite side of the waveguide, on the right side.

5.8.1 Reference Geometry

The first transmission simulation uses a glass tube with a cross section matching the mounting plates of the device under test as reference geometry, illustrated in Fig. 5.6(d). Both geometries are discretized with 20 pixels per length unit, have an overall length of $50a$, and are surrounded with a padding from the wall and perfectly matched layers on the cell boundary. The transverse size varies for both parts according to the number of cells in the PhC.
A Gaussian source with frequency $f = 0.47, \Delta f = 0.1$, and the size of the aperture is placed at one end of the waveguide, shown in Fig. 5.11. The flux plane, in which the Fourier-transformed fields should be accumulated, is placed at the opposite opening of the waveguide and doubled in size to ensure an appropriate integration size in eq. (5.5). The analyzed frequencies range from $f - \Delta f/2$ to $f + \Delta f/2$, separated in 100 linearly spaced points. Care has to be taken when choosing the frequency discretization. If the spacing is too small the Fourier transform may miss very narrow resonances which could lie between two points on the frequency grid. Additionally, narrow band resonances require longer runtime, due to the Fourier uncertainty principle, to achieve an accurate band width. Here, as the Q-factor is expected to be low from previous 3D simulations, it is not necessary to apply longer runtime and higher resolution in frequency space. The runtime is defined via a termination criterion since the time required for propagation through the structure is unknown a priori. The simulation stops when the on-axis field at the exit of the waveguide $E_z(0, 0, l/2, t)$ has decayed by a factor of 1000 from its maximum value.

The computations were repeated for different number of lattice cells ranging from $n_{cells} = 4$ to 11, and for both initially considered rod sizes, $r = 0.24\,\mathrm{a}$ and $r = 0.2\,\mathrm{a}$.
Figure 5.12(a) shows the transmission with rods of radius $r = 0.2\,\mathrm{a}$. With only few of rods, $n_{cells} = 4, 6$, the transmission spectrum exhibits peaks around $f = 0.52$ and at 0.49 resp. $0.47, 0.44$. Between those two configurations, the spectrum for 5 lattice cells drops below 1. One may assign the peak at $f = 0.47$ for 6 lattice cells to the previously found defect mode. But if this were the case, the resonance is expected to increase with increasing number of lattice cells, as described by the Q-factor in Fig. 5.4(c). For $n_{cells} = 7$ the spectrum has a small resonance close to $f = 0.48$, but it has a lowered Q-factor and it vanishes for further increase in lattice cells.
The same is observed for $r = 0.24a$. The maximum transmission is lowered compared to the thinner rods. A peak exists for a larger range of n_{cells}, up to $n_{cells} = 9$. For more rods, $n_{cells} = 10$ and 11, the transmission spectrum in the frequency range of interest drops below 1.

5.8.2 Loss and Transmission through covering box

To get a better understanding of the transmission through the waveguide, the flux through a box is studied. The flux planes, forming the box, are shown in Fig. 5.13. To reduce coupling effects

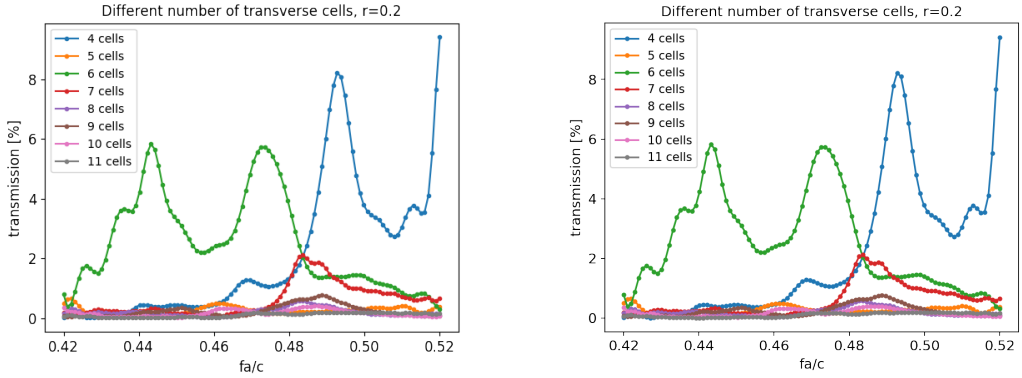

(a) (b)

Figure 5.12: (a) Transmission spectrum of the large aperture waveguide with $r = 0.2a$ compared to a hollow core glass cylinder for varied number of lattice cells in the PhC. (b) The same transmission spectrum for a rod radius of $r = 0.24$

at the entrance, the flux plane for the input signal is shifted away from the vacuum interface into the interior. The flux through the exit is considered as the transmitted power, at the right side of Fig. 5.13(a). In the side walls between the input and output plane, shown in Fig. 5.13(b), the flux is considered as the loss. Transmission and loss flux are normalized by the input flux.
Two geometries were simulated, $n_{cells} = 5$ and $n_{cells} = 10$, with a spectrum ranging from $fa/c = 0.25$ to 0.65. The result for 10 lattice cells is given in Fig. 5.14. For verification of the outcome the sum of transmission and loss is also plotted and shows, that the result is unphysical at the lower boundary of the studied frequency range. The input power is smaller than the sum of transmission and loss which contradicts energy conservation. As the used source has a Gaussian shape, centered at $f = 0.45$, the input intensity varies with frequency. The fluxes are only computed within the pulse bandwidth. Outside the bandwidth the spectral power can be so low that numerical errors become significant.
The unphysical observation may be the result of numerical errors. When repeating the simulation with a lower pulse frequency, the observed transmission and loss sprectrum becomes reasonable at that frequency. But it still exhibits the same abrupt flux increase at the lower frequency tail. It is not clear whether this happens although only the bandwidth range is considered for flux computation.
Additionally, the spectrum exhibits increasing oscillations when approaching the frequency boundaries. They can be assigned to numerical reflections [10, p. 198]. As those frequencies are outside of the band gap light propagates through the waveguide and is partially reflected from the walls of the computational cell. This occurs even with perfectly matched layers. As the spectral power lowers towards the frequency range boundaries the reflected power becomes more significant. Interference with the reflections results in oscillations.

Bise et al. carried out transmission experiments of a photonic band gap fiber with the same transverse geometry, high refractive index rods surrounded by a low refractive index medium, having a low index defect. The microstructured fiber was manufactured by a sol-gel casting technique applied to silica with air holes. The holes were filled with a high index liquid with $n_{589\,\mathrm{nm}}$ (Cargille Laboratories Series M) and transmission of IR light was measured.

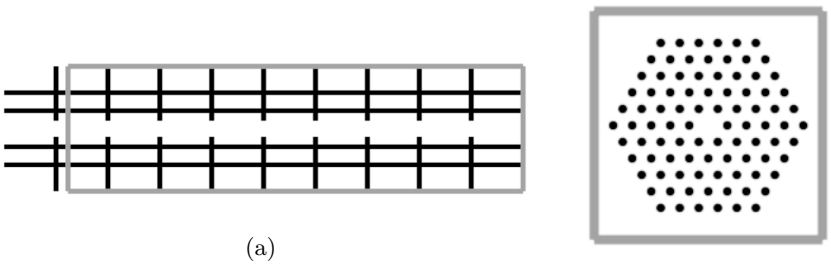

(a) (b)

Figure 5.13: Illustration of the transmission through a box. (b) Cross section along $x = 0$. The flux accumulated through the left base of the box is treated as input signal. At the right exit the transmitted flux is measured. (b) Cross section of the transverse structure. Flux through the box sides is counted as loss

In the frequency range from $f = 0.35$ to 0.55 the simulated transmission spectrum in Fig. 5.14 exhibits similar characteristics as the measured one by Bise et al.. Two flat bumps dominate the spectrum close to the band gap frequency.
On the hand the transmission spectrum can not be trusted because of the non-physical behavior of the simulation. Further work is required to study the origin of this error.

5.9 Discussion of Transmission Results

The transmission simulation with respect to the reference geometry has not shown any feature originating from the band gap. For a TM-like mode one expects a vanishing flux at the resonance frequency, as explained in the following. Since $E_z(0, 0, z, t)$ is symmetric around the z axis, the transverse components (E_x, E_y) are anti-symmetric with respect to the z-axis due to the derivative $\partial_z E_z$ in the transversality constraint, eq. (2.2). This implies $E_x(0, 0, z) = E_y(0, 0, z) = 0$. The on-axis flux in z-direction, computed from the Poynting vector component $S_z = E_x H_y - E_y H_x$, vanishes as well.

To find the origin, the dispersion relation of the defect mode has to be considered.
The TM band gap in the projected band diagram in Fig. 5.15 vanishes for a short frequency range. The studied confined mode from section 5.2 exists at $k_z = 0$, meaning that it has a constant phase along the z-axis, $\mathbf{E} \propto e^{ik_z z} = 1$. This corresponds to a wave only propagating in the transverse plane. As the out-of-plane component becomes non-zero the mode also travels along the z-axis. For small k_z the longitudinal phase velocity $v_{ph} = \omega/k_z$ is clearly above the speed of light dispersion. For acceleration k_z has to be larger, but due to dispersion the frequency of also changes.

5.10 Out-of-Plane Wavevector Component

Fig. 5.15 shows the dispersion relation of the defect mode within the band diagram. Here, band 2 as a TE-like band is blanked out again to highlight the defect.
First, we observe that the mode has zero group velocity as k_z goes to zero,

$$v_g = \left.\frac{\partial \omega}{\partial k_z}\right|_0 = 0. \tag{5.6}$$

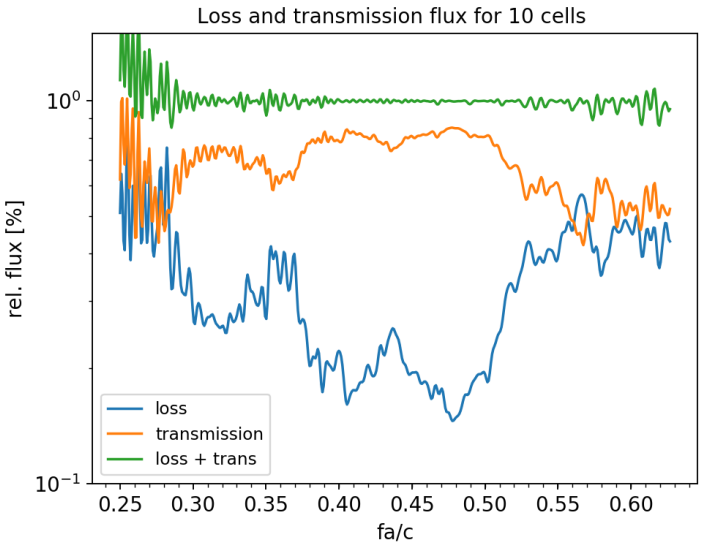

Figure 5.14: Transmission and loss through the waveguide, computed as the ratio between flux through the right gray plane in Fig. 5.13(a) and the left plane, resp. the ratio between the flux through the cladding planes and and the left input plane.

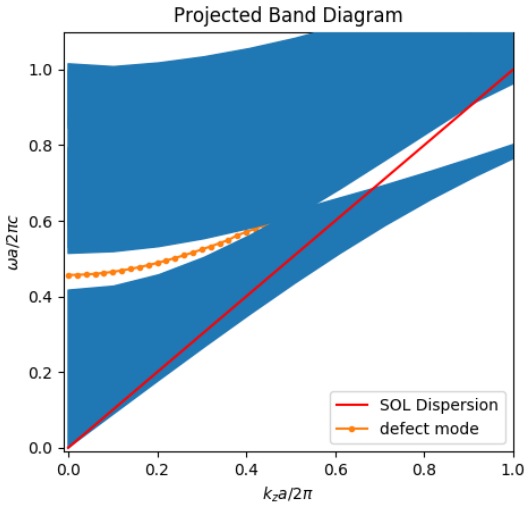

Figure 5.15: Projected band diagram of the crystal from Fig. 5.2(b), together with the defect mode dispersion $\omega(k_z)$ shown in orange. The defect band enters the air band at $k_z = 0.45$ and remains a leaky mode with further increase in k_z.

Such a mode does not propagate along the z-axis, as stated before. When k_z increases the group velocity becomes non-zero and the phase velocity finite. At $k_z \approx 0.45$ the dispersion enters a region without band gap. The mode is no longer localized. Due to continuity the mode still concentrates much of its energy in the core, but it leaks into the continuum of states of the

surrounding crystal.
In fact, the leakage happens already before as the mode is no longer a pure TM mode. Its TE component will leak into the blanked out TE band. As the TE-component of the originally TM-polarized hybrid defect mode is small, the effect was ignored. When k_z reaches 0.45 also excitation of TM-like bands occur which increases the leakage effect.
After passing the band overlap from $k_z = 0.45$ to $k_z = 0.55$ the defect mode does not enter the gap anymore. It remains a leaky mode in the dielectric band. The defect dispersion does not cross the SOL dispersion in the band gap. The introduced defect does not trap a mode SOL mode.

A different kind of defect has to be introduced. As a first try seven rods instead of one were removed in the center, shown in the inset of Fig.5.16(a) The band diagram is shown in Fig. 5.16(a) and, with focus on the band gap - speed of light line crossing, in Fig. 5.16(b). The dispersion relation lies in the band gap for wave vectors above $k_z = 0.55$ but it does not match the synchronicity condition before it enters the air band. A more detailed analysis of different defects has to be done.

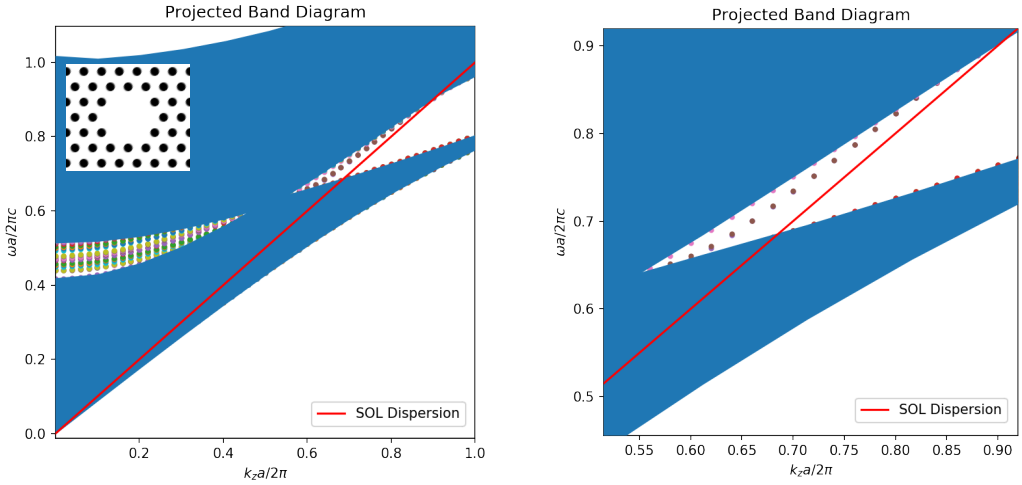

(a) (b)

Figure 5.16: (a) Defect mode dispersion in the Projected band diagram for a core of two missing rods, shown in the inset. The radius of the rods was set to $r = 0.24a$. (b) Enlarged section of the band diagram in the range from $k_z = 0.55$ to $k_z = 0.9$

Apart from matching the SOL dispersion the desired mode must also have a monopole-like E_z field pattern. The multipole character is counted be the number of nodal planes in the hollow core. The pattern from Fig. 5.3(a) is a monopole, since is does not have a sign change in a small region around the center. A dipole exhibits one nodal plane in the defect such that it is only anti-symmetric under mirror reflections along this plane. The six-fold symmetry of the crystal is broken. Such a mode is shown in Fig. 5.17(b) of the following section. A trapped mode with four nodal planes is denoted as quadrupole, while a sextupole has six planes of zero crossing in the field pattern.
As the longitudinal on-axis field vanishes for all higher order modes, $E_z(x = 0, y = 0) = 0$, they can not be used for particle acceleration. Only monopole modes are applicable.

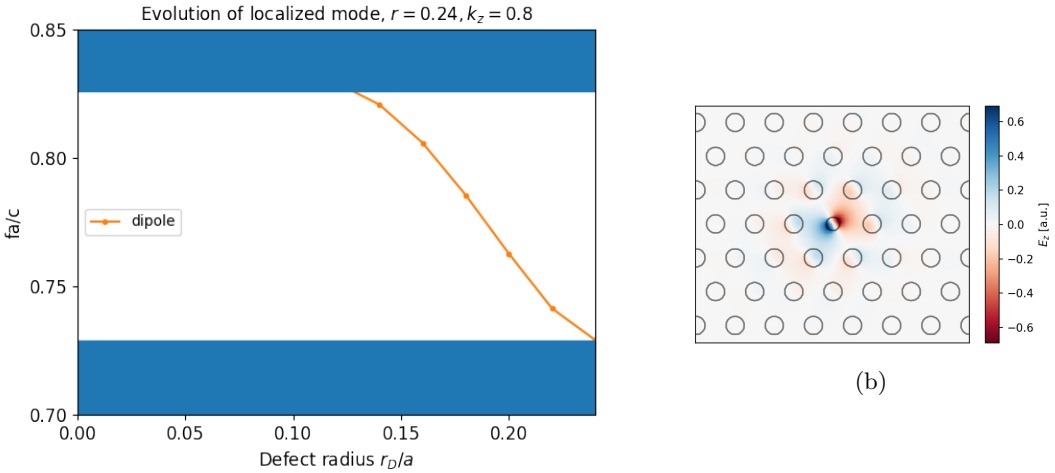

(a)

(b)

Figure 5.17: (a) Evolution of the defect mode at $k_z = 0.8$ when decreasing the size of a rod continuously from $r_D = 0.24$ to $r_D = 0$. The lower and the upper blue boundaries are the frequency ranges of the bands. (b) E_z of the localized mode for a center rod with radius $r_D = 0.18a$.

For instance, even if the localized mode dispersion in Fig. 5.16(a) had intersected the SOL dispersion the multipole character of the mode would have to be checked.

5.11 Radius of Rod Decreased Continuously

For in-plane wave vectors, $k_z = 0$, decreasing the amount of high index material pulls a state from the dielectric band into the gap, giving a trapped monopole [10, p. 81-84]. For out-of-plane propagation the mode does not have to evolve in the same way. To get a better understanding of localized mode evolution, the size of the center rod is gradually decreased. The bands in the supercell are computed for a fixed $k_z = 0.8$. The evolution is shown in Fig. 5.17(a) where the frequency of the trapped mode is plotted depending on the radius r_D of the center rod. The right end of the x-axis represents the perfect crystal while the left side, $r_D = 0$, is the hollow core structure from section 5.2. As already observed previously no state exists in the band gap in the case of a completely missing rod, $r_D = 0$. When the radius is decreased from $r_D = 0.24$ a state sweeps across the band gap from the dielectric band to the lower boundary $f = 0.825$ of the air band. For radii below $r_D = 0.12$ no state exists in the band gap.
The state which enters the band gap is a dipole, as the field pattern for $r_D = 0.18$ in Fig. 5.17(b) shows. No monopole mode exists.

5.12 Redesign of Photonic Crystal

The hollow core defect can be modified in three ways. The first one of removing more rods was already studied briefly for seven missing rods, Fig. 5.16. Instead, in analogy to the previous sec-

tion, the radius of the six core enclosing cylinders can be continuously decreased. An increasing size is expected to be disadvantageous as a larger percentage of high index medium is more likely to exhibit higher-order multipoles.
A third alternative is a circular air hole in the crystal, which is equivalent to removing a single rod if the hole size is the same as the rod size. A larger hole cuts the six inner rods, as will be shown in section 5.12.2.

For hollow core photonic band gap fibers with air inclusion in a high index material, the number of supported modes has been investigated intensively. The number of air guided modes scales approximately linearly with the core area [24], $N_{max} \propto r_D^2$, where r_D^2 is the defect radius. On the other hand, increasing the defect size appropriately eliminates surface modes. Here, the importance of the surface termination is stressed, as it strongly modifies the allowed localized modes. To keep the hollow core, the surface termination is studied by changing the surrounding seven rods.

Apart from defect modification, a crystal with varied radius r can be examined. As this changes also the band structure it gives a lot of degrees of freedom and increases the difficulty to tune the defect.

5.12.1 Size of Inner Rods Decreased

The second option, decreased radius of neighboring lattice cells, is shown in the inset Fig. 5.18 together with the band diagram at the gap for $r_2 = 0.15$. A monopole-like localized mode exists at $k_z = 0.8$, but, compared to 5.16(b), many other modes are confined in the gap as well. Exciting the structure with band gap frequency will excite all those modes.
At fix $k_z = 0.8$ the radius r_2 is varied from 0.24 to the vacancy, $r_2 = 0$. The evolution of band gap modes is shown in 5.19(a). For radii at $r_2 = 0.1$ and below a single mode is isolated in the gap. Its field pattern E_z shown in Fig. 5.19(b) has dipole symmetry. The monopole's field at $r_2 = 0.16$ is given in Fig. 5.19(c).

Due to the variety of multipoles with large r_2 values and the missing multipole mode for small rods this defect is not preferred.

5.12.2 Rod Cutting Defect

The defect introduced is a cylindrical hole cutting the rods from the second cell, illustrated in 5.20(a). For a fixed defect radius $r_D = 1.0a$ the projected band structure with varied longitudinal wave vector is shown in Fig. 5.20(a). Similar to the previous defect type, several trapped modes exist in the band gap which cross the SOL dispersion. The monopole mode at $k_z = 0.8$, shown in Fig. 5.20(b) has a frequency of $f = 0.8$ and stores 31 % of the total energy in the hollow core, defined by the radius of $1.0a$. The next higher modes are two degenerate dipoles at $f = 0.805$ which store 27 % of the energy in the center.
At $k_z = 0.8$ the evolution for varied defect radius r_D was computed, once with 50 bands in the supercell and for verification with 100 bands. Most of the defect modes are separated in two groups of same evolution. The first group enters the gap at around $r_D = 0.82a$ whereas the second one at $r_D = 0.88a$. Each group consists of four bands, two nondegenerate and two doubly degenerate modes.

Some spurious modes appear, for example at $r_D = 0.76a$ and $f = 0.76$ resp. $f = 0.775$ and at roughly $r_D \approx 1.18a$ and $f = 0.74$. Such isolated modes, which appear abruptly when varying

r_D, can occur in case of accidentally choosing inappropriate parameters for the computation. The supercell size was set to 7 and the in-plane wave vector was set to $(0.5, 0.5)$. Thereby, modes extending through the supercell can exist with the specified Bloch-symmetry which do not exist in the normal crystal. They appear if the supercell is small compared to the defect and the number of computed bands is large. In principle they can only exist if the defect repeats regularly with the periodicity of the supercell lattice. As one usually introduces only a single defect into the crystal such modes do not exist.
As an example the extended mode at $r_D = 1.16a, f = 0.745$ is shown in Fig. 5.21(b).
For verification, the supercell size has been changed from 7 to 10 and the evolution for varied r_D was computed. The found gap frequencies have not changed by more than 2 %.

As no isolated monopole mode was found the question arises whether a hexagonal crystal of glass cylinders with such a defect characteristic exists in general. Crystals with different rod radius, ranging from $r = 0.1a$ to $r = 0.4a$, have been examined together with different defect types and sizes. Not all defect types have been studied as detailed as in the last section for $r = 0.24a$, since the mode evolution is continuous. No isolated monopole mode was found. But it is still be possible that a satisfying combination of rod size and defect has been missed. An overview of the studied cases is given in the appendix. Especially for a changed rod radius r one has to keep in mind that the band gap shifts, or, might even vanish.
Lin [7] stated that the chance of a dipole mode frequency being within the band gap is proportional to the band gap width. As a consequence, to eliminate dipole modes the crystal has to be adjusted such that the gap width is small but still exists. In fact, when fixing the wave vector k_z close, but slightly above the point where the band gap opens up, the very first arising localized mode is the monopole.
On the other hand, the smaller the band width the less confined is the defect state. Here, the ansatz of small band width is followed up.

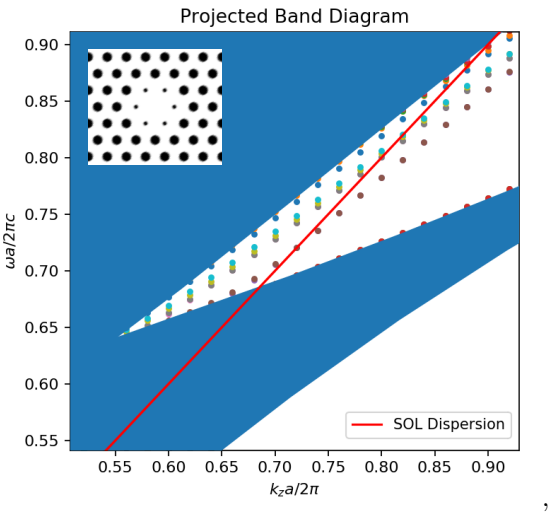

,

Figure 5.18: Band structure with localized modes at the opening of the band gap. The radius of the inner most rods is $r_2 = 0.15$, while the inset shows the PhC with $r_2 = 0.1$

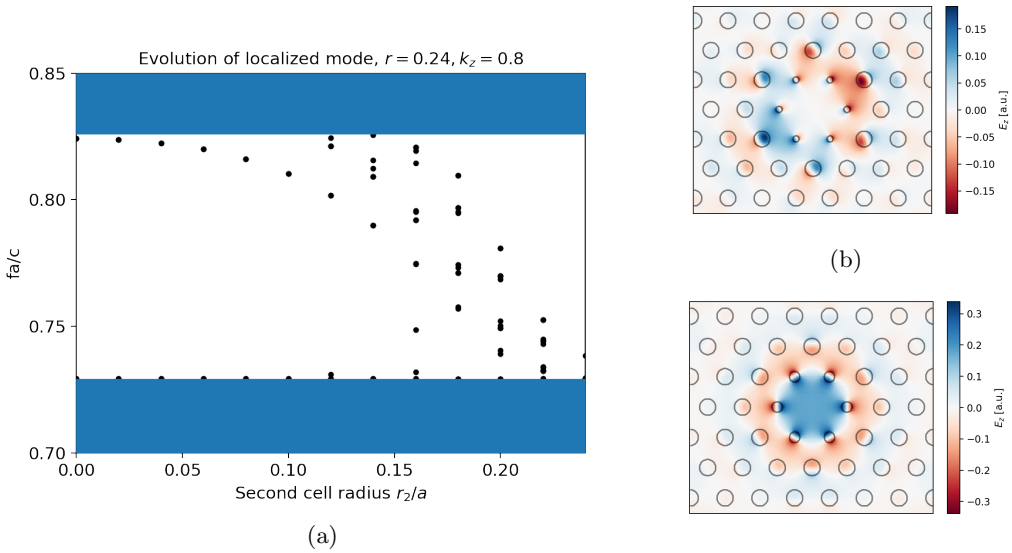

(a) (b) (c)

Figure 5.19: (a) For a crystal of glass rods with radius $r = 0.24$, the size of the inner most rods was decreased stepwise. Many defect modes appear at $k_z = 0.8$. (b) Isolated defect mode in band gap at $r_2 = 0.10$ (c) Non-isolated monopole mode with $f = 0.75$ at $r_2 = 0.16$. Modes below and above in frequency are octupole and 12-fold mode

5.12.3 Narrow Band Gap

Instead of the gap-midgap ratio at fixed k_z, the gap size here is defined along the SOL dispersion, such that k_z is equal to the frequency at the lower and the upper boundary of the gap. In Fig. 5.22(b) the band diagram is shown for a radius of $r = 0.38a$. The axes limits are set to focus on the intersection of the SOL line with the gap. Along $f = k_z$, the first band ends at $f = 0.508$ while the second starts with $f = 0.539$. Thereby, the width of the gap is 5.9 %. For selected radii the corresponding results are listed in table 5.4. For radii above $r = 0.41a$ the SOL dispersion and the first gap do not intersect.
Here, we choose $r = 0.38a$. To attain smaller band widths $r = 0.39a$ and $r = 0.40a$ can be

r	midgap fa/c	gap-midgap ratio [%]
0.16	1.2	41
0.20	1.0	42
0.24	0.80	28
0.25	0.78	27
0.30	0.66	19
0.38	0.52	5.9
0.39	0.51	4.1
0.40	0.50	2.4

Table 5.4: Midgap frequency and width of the first band gap along the SOL dispersion for varied rod radius of the photonic crystal.

taken, but while an appropriate grid discretization to resolve $\Delta r = 0.01a$ can be chosen in two-dimensions, 3D computations may require exceeding computation time. For previous 3D simulations in time-domain $\Delta x = 0.05a$ was used. A detailed convergence study has to be conducted at some point in future.

A defect, which cuts the rods, is introduced into the crystal. The size of the core was tuned to match the synchronicity condition with an accuracy of 0.3 %, resulting in $r_D = 0.97a$ for a frequency of $f = 0.52$. The monopole mode, corresponding to the blue dispersion line in Fig. 5.22(b), is less confined than previously found monopole states, but it is better isolated inside the gap. On the gap edges at $k_z = 0.52$, dipole modes leave the bands, but no further localized modes are close.
The group velocity of the desired mode is approximated by the difference quotient as $v_g(k_z = 0.52) = 0.51$, using a step size of $\Delta k_z = 0.01$.

A figure of merit of the accelerating mode is th characteristic impedance. It relates the on-axis field amplitude E_0 and the longitudinal power flow P by

$$Z_C = \frac{E_0^2 \lambda^2}{P} = \frac{E_0^2 \lambda^2}{\int_A \mathrm{Re}\, S_z \; da}, \tag{5.7}$$

where the integral has to be taken over the cross section A of the waveguide. S_z is the longitudinal component of the Poynting vector $\mathbf{S} = \mathbf{E} \times \mathbf{H}$. The flux of the mode is shown in Fig. 5.23(b). The accelerating mode attains a characteristic impedance of $Z_C = 99\,\Omega$. In comparison to a

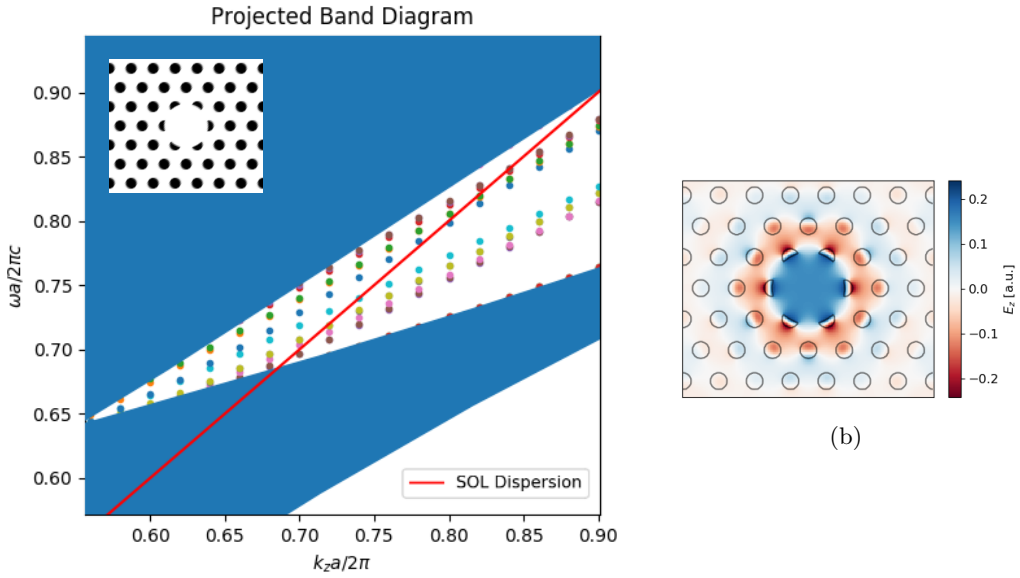

(a) , (b)

Figure 5.20: (a) Band structure with localized modes for the geometry in the inset, having a defect size of $r_D = 1.0a$. The k_z- and f-axes are focused on the crossing of the band gap with the SOL dispersion. (b) Localized monopole mode at $k_z = 0.8$ in structure with defect radius of $r_D = 1.0a$. Within the vacuum core 31 % of the overall energy is stored.

similar transverse Photonic Band Gap (PBG) structure, a silica fiber with an air hole lattice designed for IR wavelengths [7], the mode provides a more efficient acceleration.

5.13 Resonance in Truncated Crystal

In analogy to section 5.3 the Q-factor for a finite crystal is studied. Here, an additional constraint for the third dimension is applied. The boundaries along the z axis are Bloch periodic with a phase shift of $e^{ik_z z}$ for $k_z = 0.52$. The structure is treated as an effectively 2D problem, being infinitely extended. To incorporate the periodic boundaries the longitudinal structure size in the computation was set to a non-zero value resp. $\lambda/2$.
As before, the structure is excited with a Gaussian point source which is placed in the center and aligned along z. After the sources turned off the simulation is continued for a fixed period T during which the component $E_z(t)$ is analyzed with harmonic inversion [22, 20]. The resonance frequencies are extracted together with their Q-factors. The simulation is conducted repeatedly with varied number of cells n_{cells} to find the dependence $Q(n_{\text{cells}})$.
For a broad pulse of $f = 0.3$ and $\Delta f = 0.3$ three different analysis times $T = 300, 1000, 6000$ have been tested. A longer period is beneficial to decrease remaining non-resonant components in the spectrum. As several modes are found, ranging from 7 to 30 the dominating one is chosen for each simulation. As an example, an excerpt from the harmonic inversion outcome is given in table 5.5 for the simulation parameters $\Delta f = 0.3, T = 6000, n_{\text{cells}} = 6$. The mode with the smallest error in signal processing is chosen here.
The results for the broad band excitation with $T = 6000$ is shown in Fig. 5.24, together with

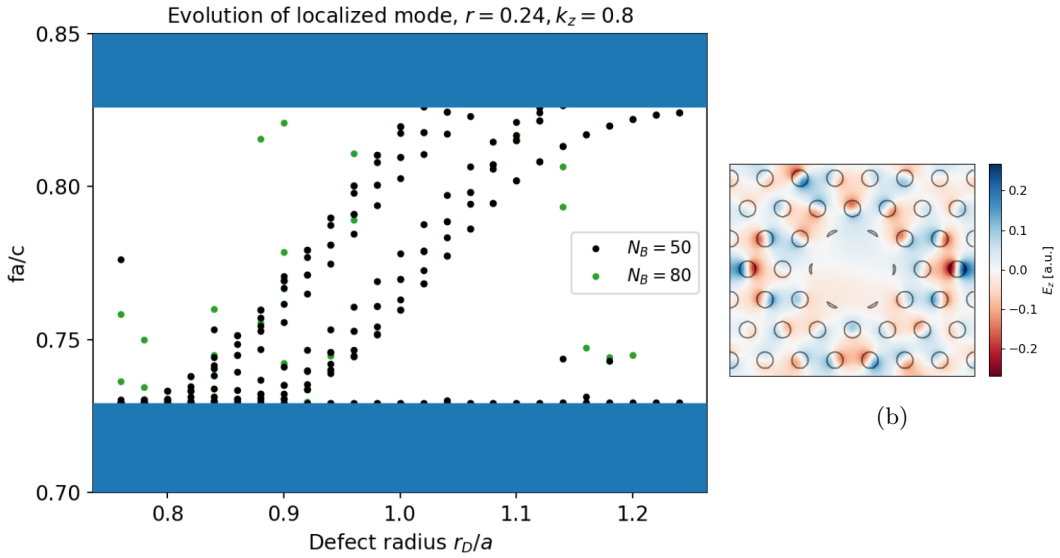

(a) (b)

Figure 5.21: (a) Evolution of localized modes in the band gap for varied core size r_D, as depicted in Fig. 5.20(b), computed with different number of bands N_B. The isolated modes, which do not change continuously with r_D, result from a too small supercell. When setting the supercell size from 7 to 10 they disappear. (b) Spurious mode in the band gap which extends through the superlattice for a defect size $r_D = 1.16$ at $k_z = 0.8$.

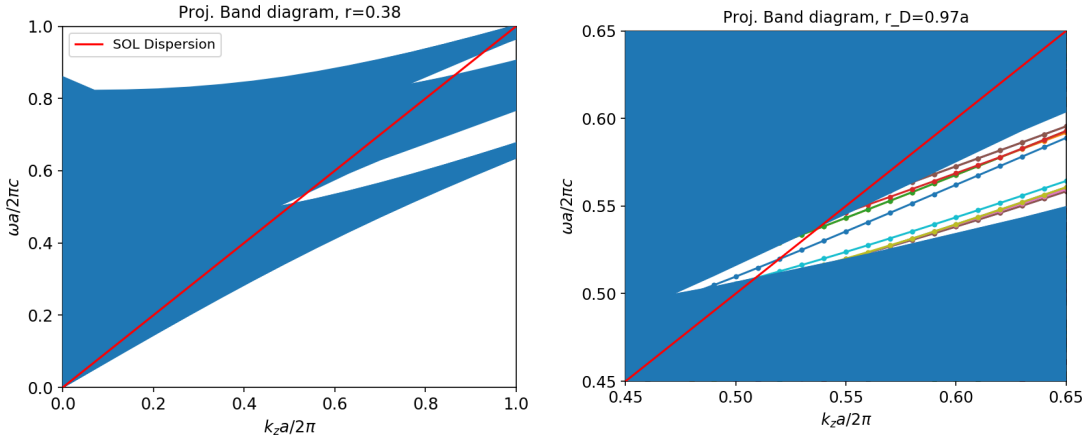

(a) (b)

Figure 5.22: (a) Band diagram for a hexagonal lattice with radius $r = 0.38a$. The gap width is 5.9 %. (b) Defect mode dispersion in the range of the intersection between band gap and SOL dispersion. At $k_z = 0.8$ the phase of the localized state propagates with speed of light.

the result from a narrow band source $f = 0.52, \Delta f = 0.01$ and $T = 1000$. In the narrow band case, $Q(n_{\text{cells}})$ follows the expected exponential law, $Q \propto e^{n_{\text{cells}}}$. Using a broad pulse, a different mode is dominating as the frequency dependence $f(n_{\text{cells}})$ points out in comparison with the narrow band case. In fact, the extracted dominating mode is not always the same as the dip at $n_{\text{cells}} = 12$ indicates. At higher cell numbers, the Q-factor does not increase further. This may result from the limited chosen simulation run time T for harmonic inversion analysis. In general, to get better accuracy in Q, the run time has to be increased. This is the same behavior as in Fourier transform analysis although the required time for high accuracy is much smaller in harmonic inversion analysis [22] with filter diagonalization method.
As the result for $n_{\text{cells}} = 6$ in table 5.5 indicates, there is a second component in the spectrum which contributes with the same order of magnitude to the signal, with $f = 0.520$. Considering the modes with second largest amplitude in the Fourier series in every simulation instead of the largest, the extracted modes from the broad band excitation match exactly those from the narrow band source. The relation $Q(n_{\text{cells}})$ is exactly the same as the one for $\Delta f = 0.01$ in Fig. 5.24.

In fact, the other mode we found has dipole symmetry and just enters the gap at the upper edge of the gap at $k_z = 0.52$, the green dispersion line in Fig. 5.22(b). Using a larger supercell for the band computation highlights the presence of the additional mode in the band gap.

To verify the result the on-axis field $E_z(0, 0, 0, t)$ during the time T has been analyzed for n_{cells} additionally by Fourier transform. The field in time and frequency domain can be found in the appendix D. Two resonant peaks appear in the spectrum whose frequencies match the modes observed harmonic by harmonic inversion analysis, table 5.5.
From table 5.4 it is known that the gap width decreases further with larger rod radius. Without recomputing the defect modes the simulation of the truncated crystal was repeated for rods of $r = 0.39a$. Again, two peaks are observed with amplitudes of the same order of magnitude. In contrast to the previous scenario, the desired mode, referring to the low frequency peak, slightly dominates the high frequency mode.

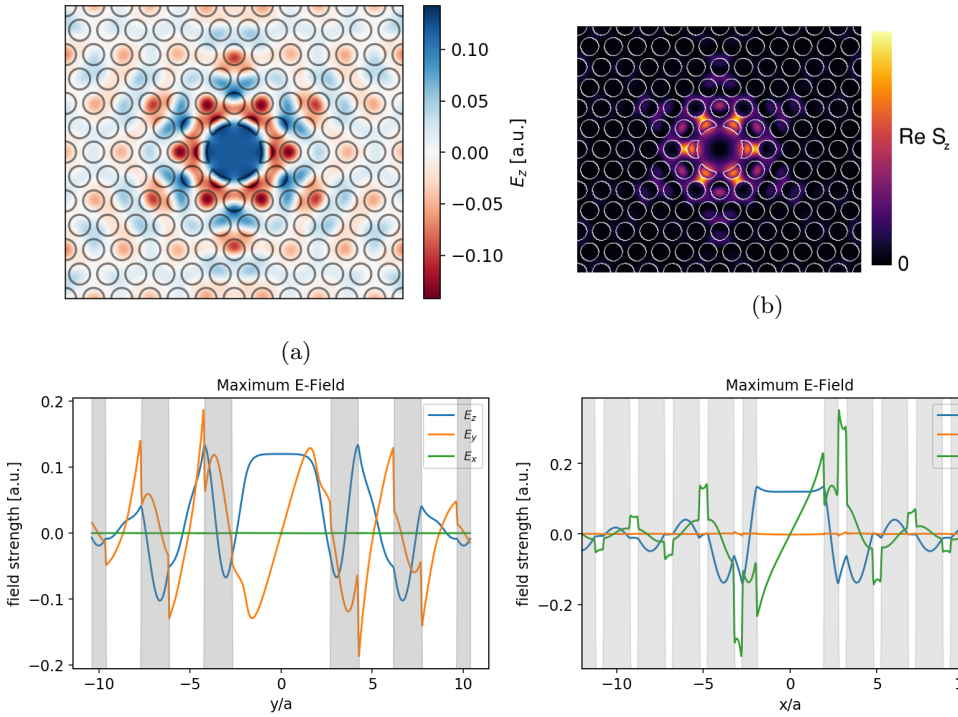

Figure 5.23: (a) Field pattern E_z of the localized mode in the supercell. (b) Intensity, given by in longitudinal direction. (c) Maximum electric field components along the symmetry axis $x = 0$. The transverse components E_x, E_y are shifted by a quarter period w.r.t. the longitudinal E_z. (d)

frequency	Q	|amp |	error
0.504	42 384	0.003	4.53×10^{-10}
0.508	89 040	0.002	1.28×10^{-9}
0.520	2656	0.055	2.32×10^{-10}
0.522	186	0.004	2.79×10^{-7}
0.527	177 398	0.066	3.50×10^{-11}
0.534	239	0.007	3.66×10^{-7}

Table 5.5: Excerpt from the harmonic inversion result of the simulation with $f = 0.52, \Delta f = 0.3, T = 6000, n_{\text{cells}} = 6$. The frequencies, the Q-factor, the relative amplitude and the error from signal processing are listed. The error does not contain information about the error from simulation parameters, only about the harmonic inversion process. More modes were found below and above the listed frequency range.
The mode at $f = 0.527$ was chosen since it has the lowest processing error and the largest Q factor. In comparison with the mode at $f = 0.520$ the relative amplitudes are very similar, meaning that they contribute almost with the same strength to the signal.

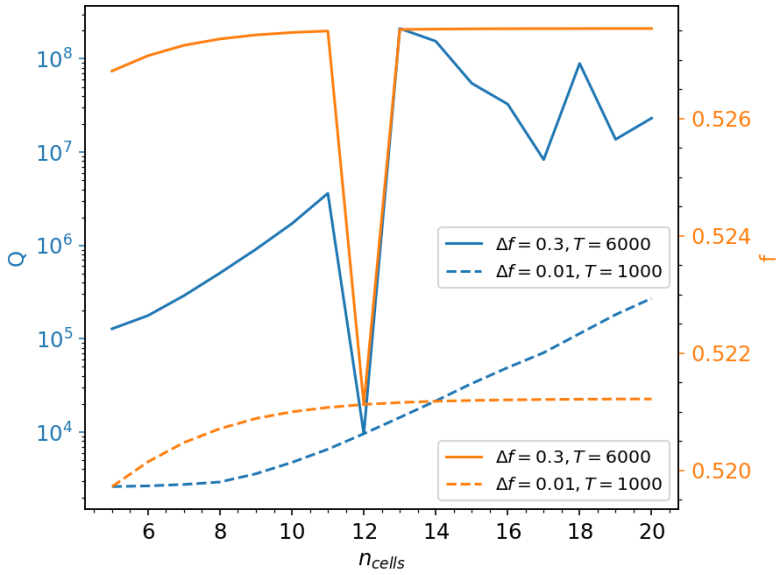

Figure 5.24: Dependence $Q(n_{\text{cells}})$ of the resonant mode in the effectively 2D simulation with periodic boundaries along z, restricted to $k_z = 0.52$, together with the mode's frequency $f(n_{\text{cells}})$. The plots depicted in blue show the Q factor, with the left axis as scale. The right axis refers to the frequency plots shown in orange.

5.14 Three Dimensional Structure

The field propagation through a finite waveguide along the z-axis is studied by FTDT. As periodic mounting introduce new constraints on the electromagnetic states, the rods are fixed only at the entrance and the exit of the waveguide. By this, the device forms an anti-resonant reflecting optical waveguide (ARROW). The cross section along the longitudinal axis is shown in Fig. 5.25(a) for a short variant of this structure. The mountings are $0.5a$ thick. The number of cells

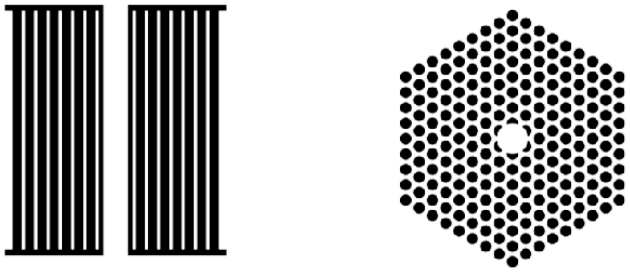

(a) (b)

Figure 5.25: Cross sectional views of the new redesigned 3D Structure of rods mounted at both ends (a) in xz plane (b) in the xy plane. For illustrative purposes the length is kept short to $L = 20\,\text{a}$. $n_{\text{cells}} = 8$

is fixed at $n_{\text{cells}} = 8$.
To stay as close as possible to the infinite model, the length of the structure should be long compared to the wavelength $\lambda = 1.92a$. Here, two cases were tested, having length of $L = 40a, 60a$. The Gaussian source $\mathbf{j}$ is placed in the center of the left aperture and excites the structure with $f = 0.52, \Delta f = 0.4$. Two different pulse widths are also tested.
With the input field $E_in(t) = E(0, 0, -L/2, t)$ and the simulated output field $E_out(t) = E(0, 0, L/2, t)$ at the opposite exit of the waveguide, the transfer function $H(\omega)$ can be defined using linear time-invariant theory

$$H(\omega) = \frac{E_{out}(\omega)}{E_{in}(\omega)},$$

where $E_{out}(\omega)$ and $E_{in}(\omega)$ are the on-axis fields in frequency domain. With the help of the transfer function, the group delay of the signal is computed as

$$\tau_g = -\frac{d\phi(\omega)}{d\omega}. \tag{5.8}$$

where $\phi(\omega)$ is the phase of the transfer function, $\phi(\omega) = \arg H(\omega)$.

5.14.1 Short Structure

The transmitted field at the exit of the short structure, $L = 40a$, is shown in Fig. 5.26(a). Compared to the initial pulse the peak field strength has decreased by a factor of 100. The dominant signal, up to $t = 350a/c$, does not have the original Gaussian shape anymore and reaches local peaks three times. This indicates several superimposed modes. When cutting of the signal for Fourier transform after that period, the spectrum is still dominated by the source frequency at $f = 0.52$, but additional neighboring peaks are already present at $f = 0.49$ and $f = 0.55$. They are five to six times smaller than the main peak.
Including the full simulated period the output spectrum is shown in Fig. 5.26(c). The right tail of the originally Gaussian shaped pulse is stretched towards higher frequencies, indicating a second resonance covered by the pulse tail. The underlying resonances can not be resolved. Further, the pulse is superimposed with a noise spectrum.
As a consequence, the group delay in Fig. 5.26(e) is also very noisy. No reliable information about the delay of a single mode can be read off. The averaged group delay over the range from $f = 0.45$ to $f = 0.58$ is determined as $\tau_g = 75a/c$, but since τ_g depends on the frequency the mean value is not sufficient. The standard deviation of $132a/c$ also emphasizes the noise dominance.

5.14.2 Long Structure

In comparison, Fig. 5.26(b), 5.26(d) and 5.26(f) show the output signal, the normalized spectrum and the group delay for the long structure, $L = 60a$.
The output field E_z shows a clear separation at $t = 191a/c$ between the first arriving pulse and the second one. By taking the envelope maximum $t = 166a/c$ of the first one and the input pulse the propagation time τ from $-L/2$ to $L/2$ was computed. The estimated group velocity of $v_g = 0.51c$ matches the one from the defect mode dispersion in section 5.12.3.
By the same approach the group velocity of the second pulse is estimated. As the peak overlaps with a smaller pulse the estimate is expected to be less accurate. The group velocity was found

to be $v_g \approx 0.35c$. For comparison the group velocity of the green mode dispersion in Fig. 5.22(b) is computed. With $v_g = 0.34c$ they coincide nicely. On the other hand, the mode in the band diagram has a dipole like E_z pattern, meaning the on-axis center lies in a nodal plane.
Also the spectrum allows to separate the modes despite the superimposed noise signal. The first peak is centered at $f = 0.517$ with a width of $\Delta f \approx 0.02$, while the second one splits up in to spikes at $f = 0.526$ and $f = 0.531$. In fact this analysis is very inaccurate as many small resonances are superimposed in the signal. At around $f = 0.55$ such a small peak is observed.
The group delay $\tau_g(f)$ does not support the group velocity estimates from pulse maxima. As before, the noise is dominating any meaningful signal.

5.14.3 Infinitely Long Unmounted Structure

To understand whether the second output pulse in the previous result $E_z(0, 0, L/2, t)$ stems from a supported mode, a simplified FTDT simulation is conducted. The rods are treated as infinitely long and the mounting of the rods at both ends is removed. The comparison between "input" and "output" refers to two points along z which are $L = 60a$ away from each other rather than the input and output ports of the structure. The result is given in the appendix E.
The observed propagated pulse $E_{out}(t)$ does not exhibit the double pulse train anymore. The tail of residual field behind the first pulse is by a factor of 10 smaller than the main peak.

This result is a good starting point for more detailed prospective studies of the pulse propagation and field transmission.

5.15 Intermediate Summary

By introducing a hollow core into a photonic crystal of glass cylinders a defect mode can be trapped in the band gap. To attain a mode propagating with speed of light along the cylinder axis, the size and the surface termination of the defect have to be varied. A core surrounded by six smaller rods, as well as a rod cutting core, supports a mode with a monopole-like E_z field pattern and phase matching velocity. But higher order modes are very close in the spectrum such that they would also be excited. With respect to particle acceleration excited higher order modes lead to undesired transverse deflections. A photonic crystal design with a narrow intersection of the band gap and the speed of light line is needed. Unfortunately this reduces the relative amount of energy stored in the core.
The crystal with $r = 0.38a$ and a rod cutting defect size of $r_D = 0.97a$ provides the desired single mode in the band gap. The resonance study of the truncated crystal indicates a second trapped mode as well as the pulse propagation results for the 3D finite waveguide. As the simulation of propagation through an infinitely extended 3D structure does not fully support this presumption a more detailed study has to be conducted.
Introducing periodic mounting plates changes the modes in such a way that additional band analysis is required. The parameters chosen here lead to undesired resonance frequencies in comparison with the transverse photonic crystal. The modes in the small and large waveguide are poorly trapped as the presence of the source in the field patterns indicate. At the current level the waveguide including mounting plates is not suitable for particle acceleration. A waveguide without periodic mountings has to be tested experimentally in advance to support the approach.

For this purpose the fabrication of such devices is considered in the following.

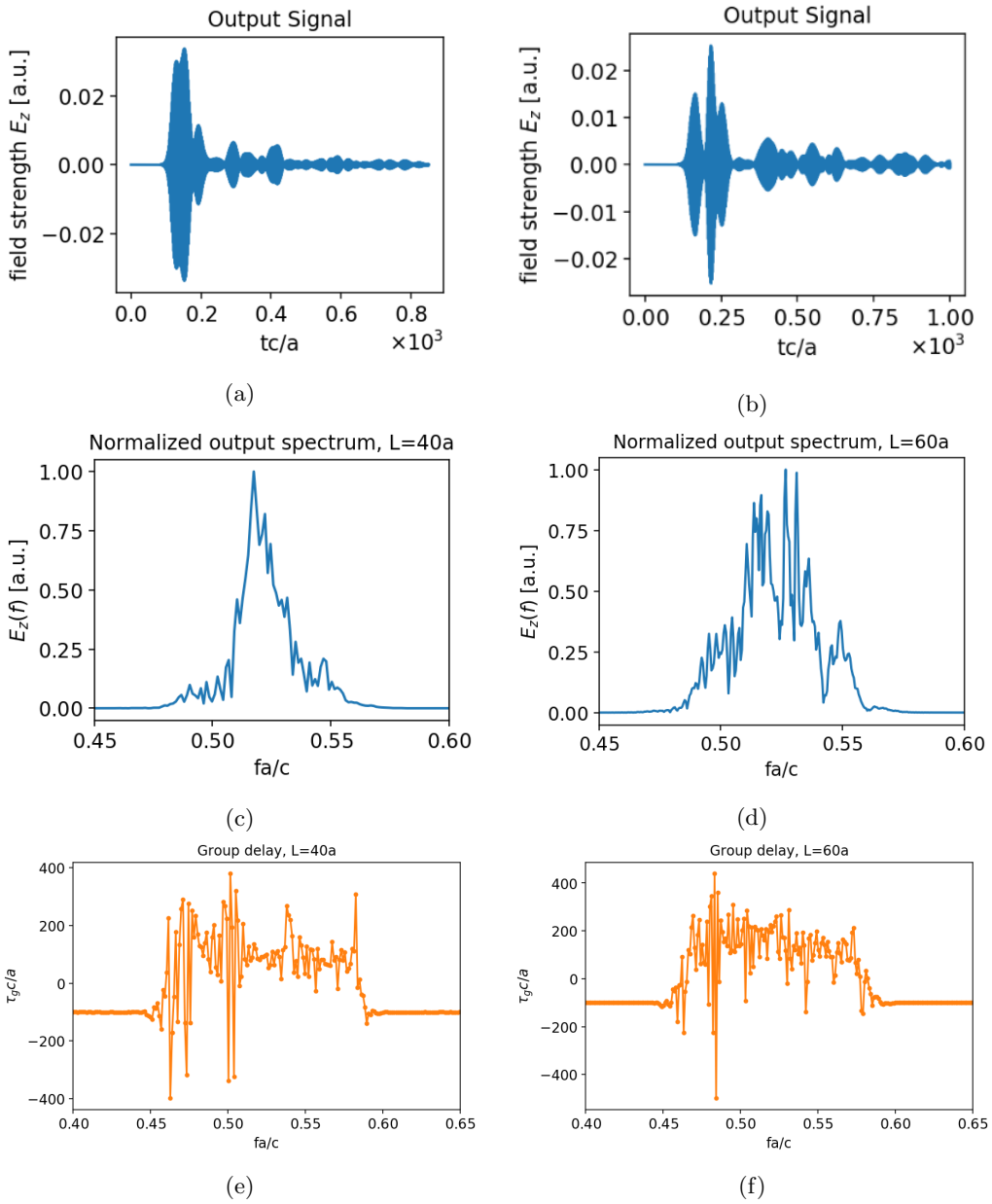

Figure 5.26: Temporal profile of the output on-axis field $E_z(0, 0, L/2, t)$ for a structure of length 5.26(b) $L = 40a$ and 5.26(b) $L = 60a$, using an Gaussian input signal with $f = 0.52, \Delta f = 0.4$. The corresponding normalized spectra are given in (c) and (d) . The group delay is computed by eq. (5.8) for $L = 40a$ in (e) and for $L = 60a$ in (f).

6 Fabrication

Combining local femtosecond laser exposure with chemical etching offers a new fused silica micro machining process for monolithic microdevices [25, 26]. The novel technique has already been demonstrated in the fabrication of micrometer scaled high-aspect ratio channels [25], three dimensional micro-flexures [27], new micro-actuators [28] and other geometric objects.

Exposing a femtosecond laser to fused silica changes the material properties such as refractive index and etching rate. A fundamental understanding for this behavior is part of current research [29, 30].

6.1 Direct Laser Writing

The method consists of the following two steps: [25]

Volume sampling during laser exposure A Ti:Sapphire laser centered around 800 nm emits a femtosecond laser pulse of 100 fs width and 240 nJ energy at a repetition rate of 750 kHz. The pulse is focused into the fused silica sample. The exposed region defines the volume to be etched. The laser affected zones (LAZ) are described as ellipsoids as depicted in Fig. 6.1(a). The focal spot in the transverse plane is about 2 µm in size while the ellipse spans over 8 to 12 µm along the beam axis. Forming large patterns is done by moving the sample in three dimensions with a speed between 5000 and 10 000 µm/s, corresponding to 150 to 300 hits by the pulse per voxel. For the following, x, y, z refer to the coordinate system in 6.1(a). The incident laser comes from the top.

Etching The machined sample is placed in an aqueous solution of hydrogen fluoride (HF) acid with 2.5 % to 5 % concentration for several hours, depending on the depth of the desired pattern. Typically, the etch speed ranges from 60 µm h^{-1} to 120 µm h^{-1}, but strongly depends on the sampling procedure, the pulse energy and its polarization. For instance, vertical walls in the zy plane, written by lines along the y axis with a distance of $\Delta z = 10$ µm, may be etched with 120 µm/h if the beam is polarized along the x axis. The same writing strategy with a polarization along the y-axis results in an etch rate of 45 µm/h at the same pulse energy.
Unexposed silica regions are typically penetrated by the acid with 0.8 µm h^{-1} in 2.5 % HF solution and 3 µm h^{-1} at 5 % concentration [5].

Here, the given figures of merit correspond to the applied settings used in the machining for this thesis. In general, parameters like pulse energy, repetition rate and writing speed can be varied.

To summarize, the technique can be described as an inverse 3D printing procedure as the sampled volume is substracted from the bulk while most conventional 3D printer methods sample the desired volume additively. Here, while structure sizes in the transverse plane are only limited by the voxel size, the height along the longitudinal axis is not only limited by the focal length but also due to increasing perturbations to the ellipse shape and spherical abberation with increasing depth of the focal spot.

For a writing procedure the following geometric aspects have to be considered:

From bottom to top LAZ distort the focal spot as the refractive index has changed. Therefore writing procedures start at the bottom of the desired pattern and always move up towards the sample surface.

No writing at sample edges The closer the focal spot moves towards a sample edge in the transverse plane the more the focus will be distorted from the ellipse shape. At the edge the beam is poorly focused as half of the beam travels through glass while the halftravels through air. The focal conus is clipped.

Direction dependent polarization As described above the etch rate changes with the polarization of the laser field. For vertical features, created by stacked lines written in the transverse plane, optimal etching is achieved with polarization perpendicular to the writing direction. In case of horizontal planes, assembled from lines, parallel polarization is preferred [31]. The change in etch rate for varied polarization results from the formation of nanogratings which are aligned parallel to the incident electric field [32].

Avoiding complete bulk sampling For large regions from which the glass should be removed it is difficult to sample the whole volume. The laser introduces stress into the glass which accumulates in regions where each voxel is exposed. If the energy deposition reaches a certain level mechanical stress is released by fracture. Splitting the volume into smaller subregions such that glass parts can drop out is preferred in this case.
This will become more clear with the aid of an applied example, which is done in a later section.

6.2 Intermediate Steps

The software to operate the volume sampling uses predefined geometric objects and spatial operations like planes, cuboids, trenches and circles, or relative movement and rotation of the coordinate system. Those objects are programmed in the software with an imperative ansatz. In operation, a text file with its own declarative language, defining the volume sampling, is parsed

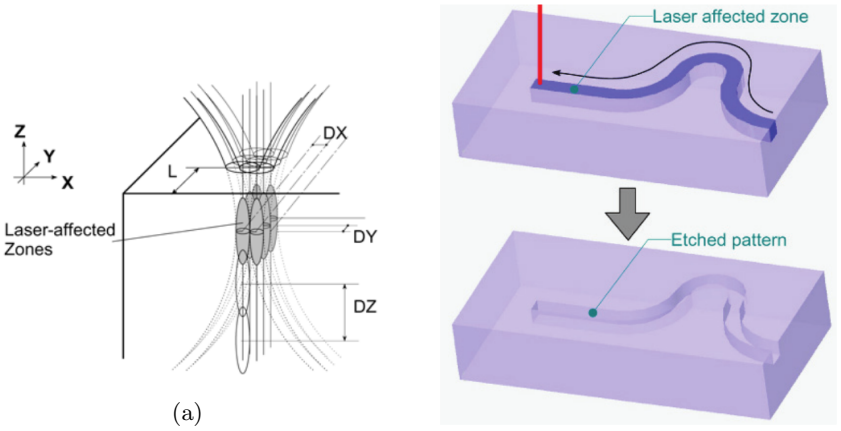

(a) (b)

Figure 6.1: (a) Volume sampling process to form larger patterns by connecting Laser affected zones [25]. (b) Two step process for monolithic manufacturing of a glass structure [26].

by the software and translates it to controller code. The controller operates the stages as well as the polarizer and the laser shutter.

For our purpose of a long waveguide the predefined objects are not sufficient. Currently the maximal tested thickness of silica samples is 1 mm. For cylindrical rods longer than the thickness it is necessary to orient their axis along the transverse xy plane. The predefined circle object allows only writing inside the transverse plane, such that a cylinder axis would be oriented along the laser beam direction. In the transverse plane the LAZ are rotationally symmetric. Considering a circle in the xz plane the size of the ellipse has to compensated.

In the previous chapter the coordinate system for the waveguide was defined such that the guiding direction is called the z-axis, while the plane of periodicity was described as xy plane . Using the coordinate system for the volume sampling we define the laser beam direction as the z axis and x and y are the transverse axes. As the guiding direction of the final structure will be perpendicular to the beam direction of volume sampling, the original coordinate system is adjusted from now on. The 2D PhC plane resp. the cross sectional plane of the rods is termed xz-plane, while the y axis is aligned along the cylinder axis.
In the following, the initial crystal design from Fig. 5.4(a), is manufactured as a feasibility study of the applied method.

6.2.1 In-Plane Aligned Cylinder

The problem of describing cylinders along a transverse axis from an ellipsoid reduces to two dimensions as the third axis is continuous. An ellipse of halfaxes a and b in the xz plane has to be moved such that the enclosed area forms a circle of radius r. In mathematics the gen-

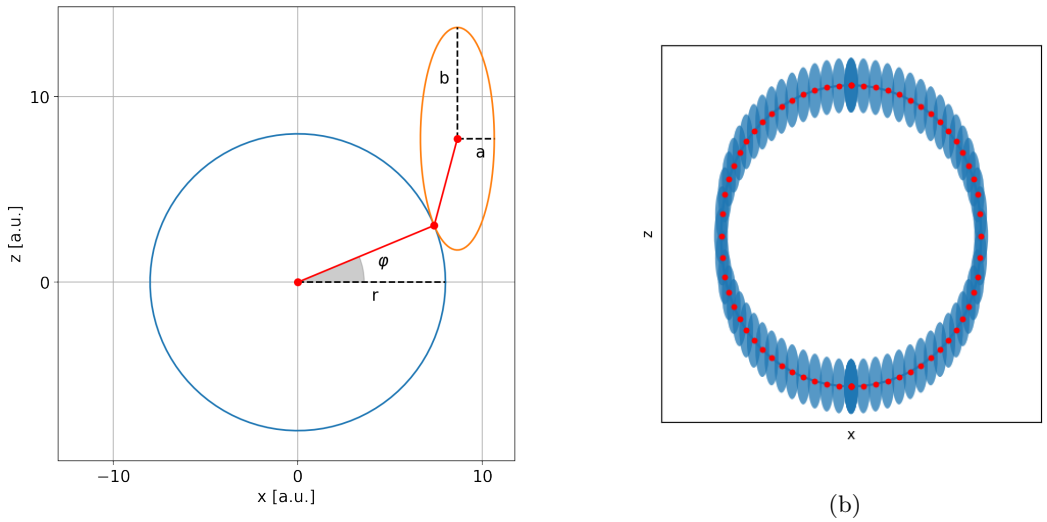

(a) (b)

Figure 6.2: (a) Contact point between circle and ellipse, parametrized by the angle ϕ between contact point and x axis. (b) Discrete volume sampling to enclose a circle by ellipses

eral problem is termed the contact point between two functions. Here, the contact point of the ellipse and the circle is needed, parametrized such that the contact point moves around the circle.

Here, the result is given directly without derivation, but the approach is sketched shortly. First, a movable circle is used to cut out an ellipse. In the following cutting means varying the free parameter over its full range, e.g. a point moving along a circular path over 360° cuts out a circle.
The enclosing circle of fixed radius was derived by adjusting the size of the osculating circle and placing it on the opposite side of the ellipse curvature. By transforming the coordinate system such that its origin matches the circle's center point the ellipse cuts out the circle.

The result is given by

$$\mathbf{K}(\varphi) = \begin{pmatrix} a\cos(s(\varphi)) + r\cos\varphi \\ b\sin(s(\varphi)) + r\sin\varphi \end{pmatrix}, \quad \text{where } s(\varphi) = \arctan2(b\sin(\varphi), a\cos(\varphi))$$

is the parameter describing a centered ellipse as $(a\cos(s), b\sin(s))$. a and b are the halfaxes along x resp. z as shown in Fig. 6.2(a), while $\mathbf{K}$ is the center point of the ellipse. By varying the angle φ from 0 to 2π the ellipse moves around the circle.

In the experimental setup, the stage uses a linear motor to move the sample. Circular motion is also supported but not helpful for writing a circle with the ellipsoid. The free parameter is discretized by a resolution parameter N, but instead of writing the circle from 0 to 2π, two half circles are written by variation of $\varphi \in [-\pi/2, \pi/2]$ with $\Delta\varphi \pm \pi/N$. This is done because of exposed regions within the beam when φ passes π. The laser penetrates the glass from the top, pointing in negative z direction. The written upper half circle would distort the beam due to refraction when writing the lower part.
Fig. 6.2(b) shows an example of the rastering, with a angular resolution of 32 points per half circle. Including the third dimension, the routine works as follows: (i) Start from the bottom of the cylinder and write a line along the y axis. (ii) Do a step by $\Delta\varphi$ in the xz plane (iii) Write a line in negative y direction (iv) Alternate between lines along y and $\Delta\phi$ steps in xz (v) When reaching the top, move back to the bottom with switched off laser (vi) Redo the alternation between lines and angular stepping with $-\Delta\varphi$ for the left half circle.

The waveguide pattern is written by repeated application of the cylinder routine. For this purpose the crystal in Fig. 5.4(a) is split into $2n_{cells}+1$ layers along the z-axis. The result for an exemplary laser writing is shown in Fig. 6.3. As geometric parameters $n_{cells} = 3, r = 40\,\mu\text{m}, a = 170\,\mu\text{m}$ were used while the focal shape was assumed to have halfaxes $a = 1\,\mu\text{m}, b = 4\,\mu\text{m}$. The half circular arc was rastered by 180 steps for each rod. But the written pattern is not accessible for etching which is why channels and grooves from the surface to the rods are required.

6.2.2 Three Cylinder Structure

As an intermediate step for acid accessibility a structure of three parallel rods close to the surface is manufactured. Two horizontal planes, in the xy plane , connect the rods in between while a vertical plane at the top of each rod is written towards the surface. Further walls and planes at the sides and on the bottom allow to embed the cylinders in a hollow box made out of glass walls.
Fig. 6.4(a), 6.4(b) and 6.4(c) show the sample after laser writing, after etching of 6 h, and after 12 h from the cross sectional view. The first etching was not sufficient as the slightly skewed glass blocks indicate. Close to the surface they should have dropped out if the etching at the

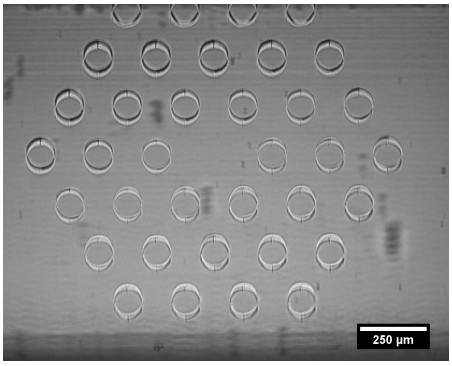

Figure 6.3: Hexagonal pattern of written circles with radius $r = 40\,\mu m$ and a assumed size of the focal ellipse of halfaxes $a = 1\,\mu m, b = 4\,\mu m$.

opposite side was sufficient. This is the case in the third image.

Here, the rods are still attached to the bulk on both sides. They form a bridge like structure between the glass in front and behind the cross sectional view in 6.4(c). As the later waveguide has to be accessible from one side to send the particles and the accelerating laser into it, the bulk glass in front has to be removed. Three written vertical planes and one horizontal one, going from the sample to the edge, form a cube which should drop out during the acid bath., Fig. 6.5(a). At the sample edge the horizontal plane didn't etch completely because of clipping of the beam, as described in section 6.1.

A different approach was considered by writing the structure far from the sample edge and "cut" out a smaller sample on which the written pattern resides on the cut edge. Four vertical walls of 1000 µm height, ranging from the substrate bottom surface to the top surface, are written around the cylinders. During etching the walls detach the subsample from the surround glass. Fig. 6.5(b) shows the first result of a free standing rod structure. The rods are $(71.0 \pm 1.2)\,\mu m$ by $(57.0 \pm 0.9)\,\mu m$ in size and separated by from each other by $200\,\mu m$, measured from center to center. The uncertainty refers to the relative differences in size rather than the absolute uncertainty due to calibration.

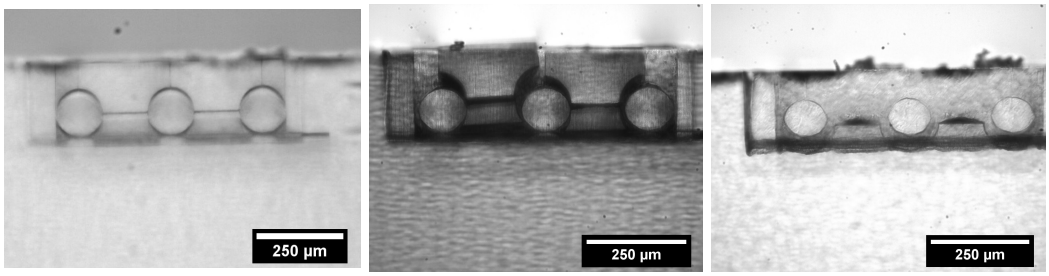

(a) (b) (c)

Figure 6.4: Three cylinders written close to surface to study planes as etching paths. (a) Written pattern by the femtosecond laser (b) Structure not fully etched (c) Final structure after additional 4 h acid bath

6.2.3 Bulk Etching

The pattern applied in Fig. 6.4(b) to remove bulk glass can not be used between inner rods in the hexagonal waveguide structure in Fig. 6.3. The glass blocks are to big to drop out through the spacing between the outer rods.
The bulk is split into two parts, as presented in Fig. 6.6. The region enclosed in blue is denoted as the volume between layers and the volume bounded by the green lines and the rods is called in-layer volume.
The first one is sampled as a rectangular block consisting of multiple horizontal planes. This is shown in the appendix, F.1.
The second procedure requires a correction for the circular arc in the xz-projection. Two approaches were tested in which horizontal planes resp. vertical planes are used. both consisting of written lines along the y axis. The horizontal routine is sketched in the inset of Fig. 6.7. The sampling takes two discretization parameters, one for the number of angular positions and one for the number of lines within the plane. For illustrative purposes those parameters are set to low values in the sketch. Using those settings the LAZ would be distinct and wouldn't form a continuous volume in the bulk.
To test the in-layer bulk etching an additional three rod device was written. The result is shown in Fig. 6.7. In comparison with the three rod structure from Fig. 6.5(b), the width of (73 ± 1) µm is the same within the uncertainty range. Along the z-axis, (64 ± 1) µm are larger than in the first structure. Further, the cylinder top exhibit some fracture like features, highlighted by the lower arrow in the image. In the surrounding substrate an additional characteristic is observed on the edge, tagged by the upper arrow. It is not clear what happened to the surface in that region.

The test in the hexagonal pattern failed which is why the in-layer sampling routine was switched to vertical planes, as depicted in the appendix in Fig. F.1(c)

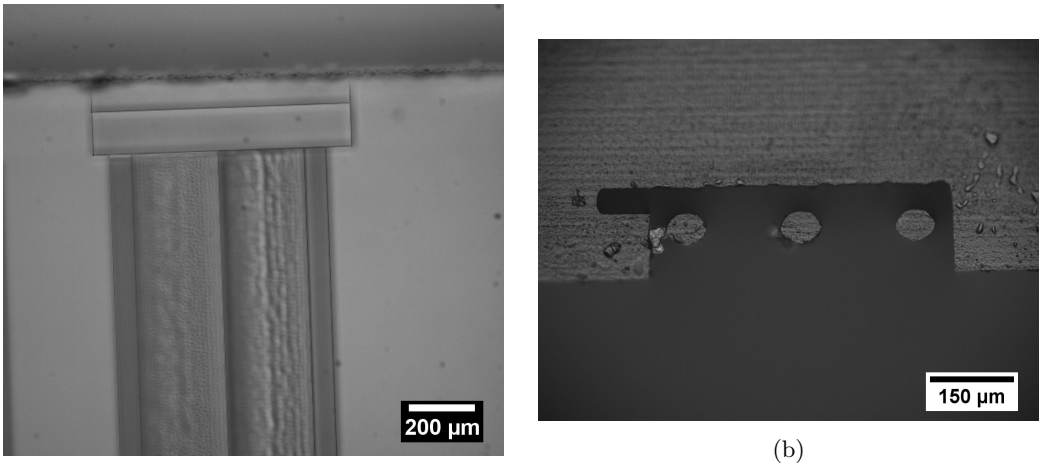

(a) (b)

Figure 6.5: (a) View onto the sample from the top, the laser direction. The pattern is written close to the sample edge to remove the small glass block in front. (b) Three free standing rods, attached to the glass only on the opposite side, attained by cutting a subsample from the main sample. They have a length of 1 mm, a horizontal width of (71.0 ± 1.2) µm, and a height of (57.0 ± 0.9) µm at the shown side.

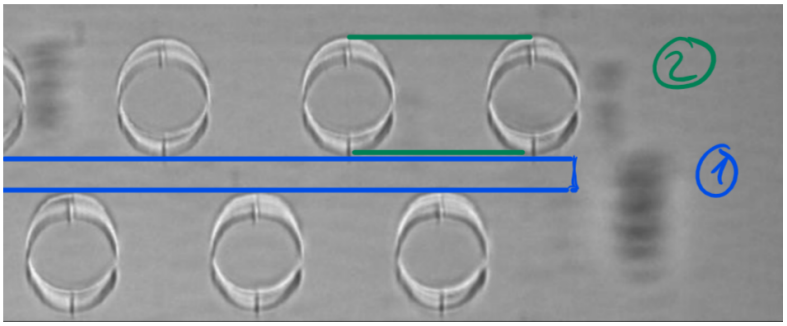

Figure 6.6: Between-layer volume (1) and in-layer volume (2) highlighted. A layer is a row of rods along the x axis.

6.2.4 Discretization Parameters of Writing Strategy

For the complete bulk sampling different components are required. The sampling scheme is given in the appendix F.

Eight different resolution parameters are used for a single hexagon waveguide, denoted as $c_\alpha, m_\alpha, m_x, m_z, n_x, n_y, p_\alpha, \Delta x_p$. The required spacing between lines must be adjustable for different components of the assembled geometry.

There are three different values for the discretization of the circle. The first one c_α refers to the number of angles for a single cylinder, 6.2(b). In order to get a cross section as close as possible to the circle this resolution should be large. The surface roughness of the cylinder is determined by a small angular discretization, and not yet by the limitations of the ellipse shape. The in-layer bulk sampling requires an additional angular resolution parameter m_α. The step size precision for the circle is not needed, and a large line density induces a lot of stress in the bulk. It is preferential to keep this parameter small. Experimentally, a factor of 4 smaller than c_α has been applied and is sufficient to remove the bulk silica around a single rod. The last angle parameter p_α discretizes the stepping over the hollow core. As the core radius is larger than the rod radius the step size also has to be increased.

An additional parameter is used to define the step size Δx_p for lines inside the core. The routine does an angular step in the xz plane, samples the volume in the horizontal xy plane, and continues with the next angular step on the opposite half circle. The residual lamallas in the center of Fig. 6.8(d) are due to the horizontal stepping.

Four parameters discretize the in-layer bulk sampling, Fig. F.1(b), and the bulk sampling between the rod layers, Fig. F.1(d). In-layer each with a horizontal and vertical number of steps, m_x and m_z resp. n_x and n_z. The parameters are distinguished to reduce energy deposition. For instance, a small horizontal step size $1/n_x$ between layers is beneficial for the etch front speed along the x-axis. This is desired to get the acid fast into the core. For the in-layer bulk the etch front should predominantly move along z.

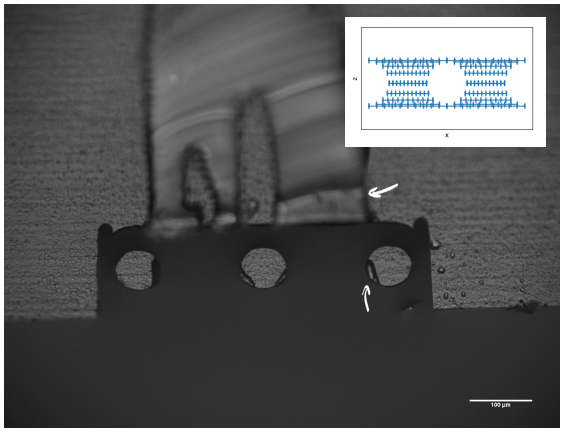

Figure 6.7: Three free standing rods written with in-layer bulk etching routine, shown in the inlet. The lower arrow marks a fracture on the top of the rod while the feature at the top arrow is not well understood but could also indicate fracture.

6.3 Final Routine for Hexagonal Waveguide

The intermediate steps are assembled in a routine for the geometry of interest. Here, only the rods are considered without mounting plates. The rods will remain attached to the bulk on one end. The method will have to be extended n future to include mounting plates, attached to the substrate, and a hollow channel going through the structure from both sides.
The density of written lines for bulk etching induces a lot of stress during exposure. This may lead to cracks when the stored energy is abruptly released during the acid bath. An example is visible in Fig. 6.8(b). The appropriate choice of line density in the bulk is a difficult question which has to be addressed separately.

Fig. 6.8(a) to 6.8(d) show images of a single cell waveguide. Since this is far from a lattice the previous simulations are not applicable but it exhibits many characteristics relevant for further optimization of the writing procedure.
The structure was placed close to the sample surface and the acid diffused into the sample only from one side. Etch paths from the surface to the structure are visible. The square blocks between the circular like rods are due to a missing bulk etching part in the writing routine. At the top end of the rods, Fig. 6.8(a), the hollow core has a size of 150 µm by 155 µm. The white blurred characteristic already indicates some geometrical features which lie deeper below the surface of projection. Images taken with a scanning electron microscope, using an energy selective backscattered detector, present the underlying features, Fig. 6.8(c) and Fig. 6.8(d). Their depth is estimated as (100 ± 30) µm. Those lamellas remain because of incomplete etching in the deep bulk. The line spacing was set to 2 µm.
The size of the rods was also measured, as shown in Fig. 6.8(d). Rods closer to the surface are smaller since they are longer exposed to HF than the deeper ones.

Two additional structures with $n_{cells} = 2$ were written. While the first one uses the same routine as the previous single cell waveguide, Fig. 6.9(a), the second one improves three steps. As shown in Fig. 6.10, the cubic blocks between the rods are exposed to the laser and are either partially or fully etched at the sample edge. The blocks closer to the bottom are less etched

such that parallel walls remain. Second, by measuring the ratio of the vertical and horizontal rod size in previous samples the ellipse parameters were corrected for the circular shape, $a_e = 1\,\mu\text{m}, b_e = 11\,\mu\text{m}$. The cylinder's bases have a height-to-width ratio of 1.05 which is closer to 1 than the previous ratios of roughly 0.8. Third, the structure was placed in the center of the 1 mm thick sample and etch paths were added from both surfaces. Hereby, the acid penetrates the LAZs from both sides, leading in principle to similar size of the upper most and lowermost rods.
On the other hand, the fused silica in the center was not removed in the acid bath. Similar to the square blocks below the center bulk the regular writting pattern is visible. Furthermore the rods are not symmetrically arranged anymore. The very first layer is unfinished as the stage controller stopped the routine before the end. The second layer is more far away from the central layer than the fourth one. Within the central layer, the second and fourth rod are shifted towards the bottom, counting from left to right. The same happened to the first one in the fourth layer, while the central rod is missing the lower most layer. The cylinders in the last layer also exhibit grooves along the z-axis.
Whether the latest characteristics are due to some error in the writing method, in the fixing of the sample on the stage or due to damage during transportation can not be clarified here because of time limitations.

None of the manufactured hexagonal structures is geometrically close to the desired photonic crystal. Further work has to be done to achieve a satisfying structure. Each intermediate step requires a more detailed study, starting with the cylindrical rods.

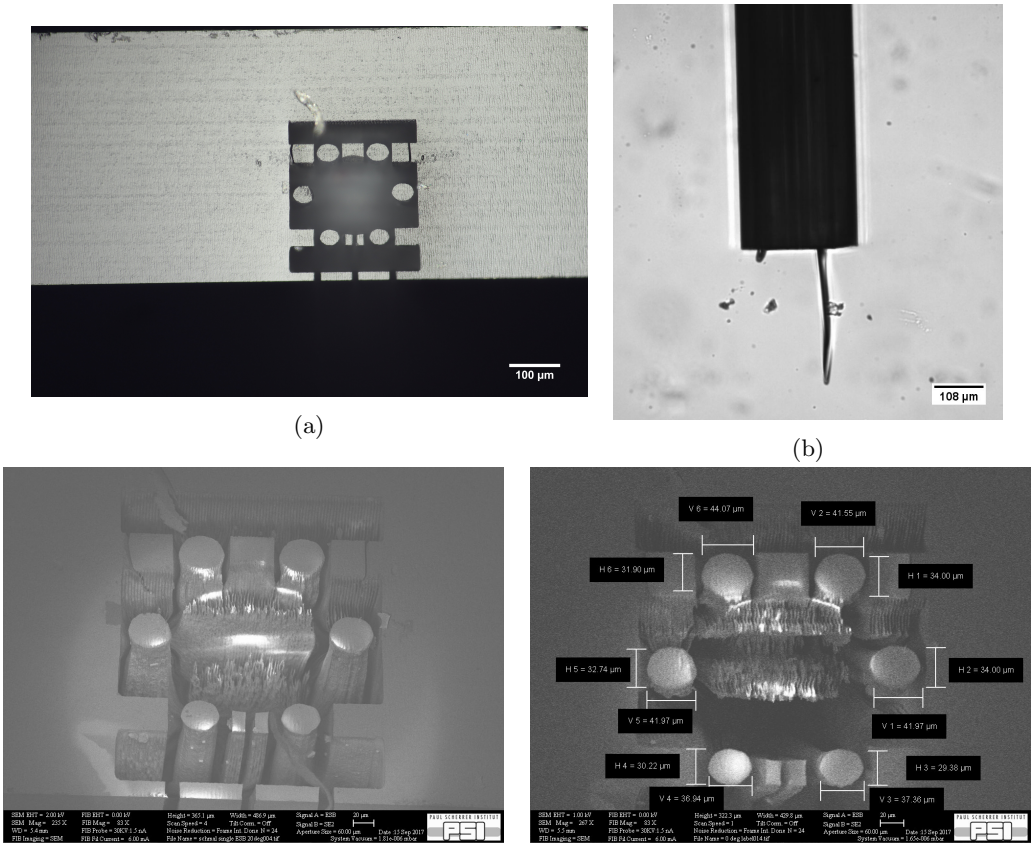

(a) (b)

(c) (d)

Figure 6.8: A hexagonal structure of cylindrical rods, written with a radius of $r = 25\,\mu\text{m}$, distance $a = 100\,\mu\text{m}$, $n_{cells} = 1$, angular discretization with 64 points per halfcircle, an ellipse shape estimated with $a_e = 1\,\mu\text{m}, b_e = 4\,\mu\text{m}$. The cylinders are 1 mm long. Some residual square-shaped beams remain between the rods due to a missing part in the bulk etching routine. 6.8(a) Side view in the xz plane 6.8(b) Top view in the xy plane, focused on the attached end of the rods 6.8(c) SEM image of the xz-surface under a tilt of 20° 6.8(d) SEM image of the xz-projection with measured size of the rod dimensions. The SEM images were taken by a Zeiss Nvision, using the energy selective backscattered detector.

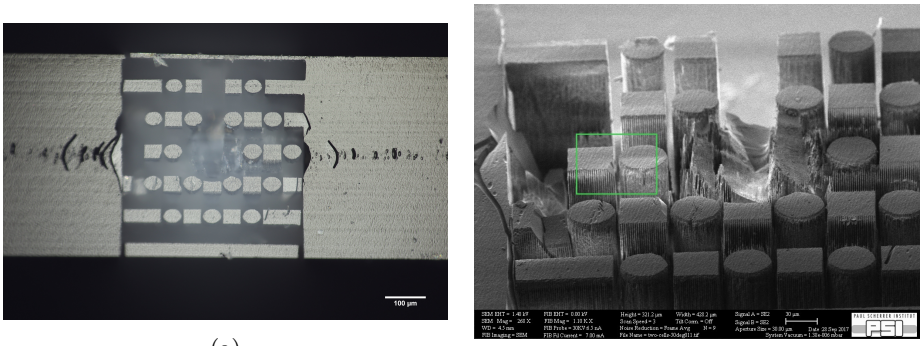

(a) (b)

Figure 6.9: (a) Hexagonal waveguide structure with two lattice cells. Apart from the angular resolution, 90 point per half circle, the same parameters as for the single cell structure, Fig. 6.8 were used. (b) The same structure imaged with the SEM under an angle of 50°. The discterization of the circle as well as the bulk volume can be observed.

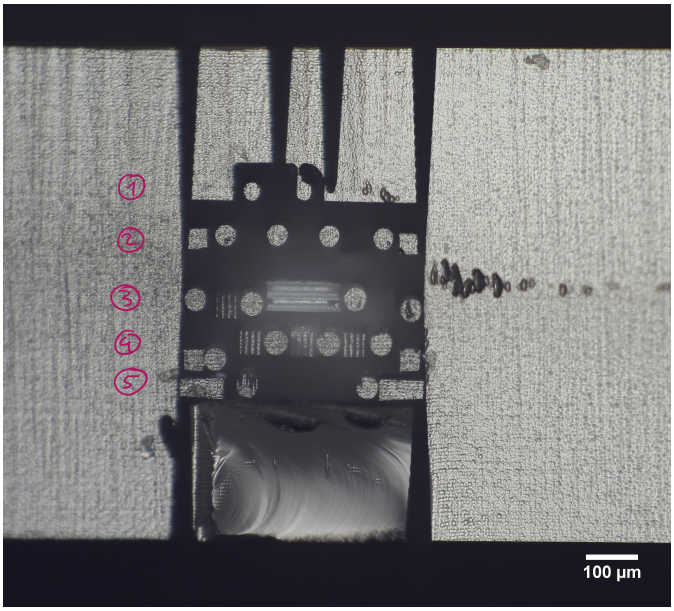

Figure 6.10: Incomplete hexagonal waveguide, centered in the fused silica sample.

7 Discussion and Outlook

No structure has been manufactured successfully which matches the designed geometry. The fabrication technique is discussed with focus on effects from etchant diffusion, laser setup and writing parameters. Based on those parameters, a more detailed step-by-step approach is proposed to improve the current results.
In the third section the approach in PhC design is summarized and discussed. Finally future improvements and potential coupler designs are proposed as well as two waveguide dimensions for future experiments.

7.1 Fabrication

The first obstacle is the complex diffusion problem of the etchant, in which the acid removes material from the surface of contact and, thereby, lowers the acid concentration. The lowered concentration affects the etch speed. Second, the laser exposure exhibits physical limitations. Defining the focus as an ellipse of a fixed size is an approximation which fails when the limits of this definition are reached. Finally, also parameters of the writing strategy contribute to the outcome.

7.1.1 Diffusion

The highly anisotropic etching is possible due to the change of material properties by the laser exposure. While the LAZ are removed in 2.5 % HF with a speed between 60 µm h^{-1} and 120 µm the unaffected silica etches with 0.72 µm at 2.5 % concentration [31] resp. 3 µm h^{-1} at 5 % [5]. During the process the ratio between those etch rates, called selectivity, decreases as the aqueous solution saturates [31].
The diffusive effect is sketched in 7.1(a) and is observed easily in the etch paths in Fig. 6.10 The written pattern from the surface to the structure is a simple stack of lines, forming a wall, but the shape after etching is conical in cross section. For deep walls the etching takes longer than for flat ones. The present walls should require about 5 h to reach the region of interest. During that time the selectivity may have dropped by factor of 2 approximately [31], depending on the concentration. Using heated potassium hydroxide (KOH) (at 80°) instead of HF improves the selectivity significantly. The selectivity is almost constant over a long period [31] but it also lowers the etch rate by itself leading to longer etching times.
Regions which are closer to the acid channels will be more etched than regions far away from the channels. This is especially important for deeply buried rods. While an outer rod, close to the surface, is exposed to HF everywhere along the z-axis at the same time, a deep rod may be reached by the acid first at the cylinder cover. This is due to the vertical cutting walls. This can lead to a different cross sectional width along the cylinder axis, similar to the scheme in 7.1(a), but with smaller diameter close to the sample edge than inside the bulk. A detailed analysis for the rod geometry is needed.

Inverting the diffusion process is a difficult task in general, and can be done only for very simplified models [33, 34]. Here, we observed that the diameter of the resulting rods is about 35 µm which differs from the applied parameter of 25 µm in radius resp. 50 µm diameter. Studying

the etching of a single rod in more detail may allow to invert the surface defining process for a limited range of parameters. In a simplified approach in which continuous etching along the cylinder axis is assumed, one may ask what radius do you have to apply to the writing method to get the desired outcome of $r = 25\,\mu m$.

7.1.2 Laser Exposure

Within the LAZ of a single spot, self-organized features on the nanoscale are present, the nanogratings. Those parallel groves are aligned perpendicular to the incident electric field and their orientation relative to the writing direction affects the etch rate. For instance, the etching time for vertical walls can be halved by changing the polarization from parallel to perpendicular orientation with respect to the transverse writing direction [31]. This polarization dependence can help to minimize the different acid exposure times to the rods. For instance, etch paths to a deeper rod should have higher etch rate than those to a closer rod. By controlling the etch rate the acid reaches both rods at the same time.

The energy deposited in a LAZ is an additional parameter which has impact on the etch rate resp. the diffusion process. Here, the pulse energy, the repetition rate and the writing speed were kept fixed for all experiments but the density of lines varies. If lines have a large overlap, the induced stress in the overlapping volume is larger than in the surrounding volume. The glass-water interaction is accelerated by the application of stress [36] and, therefore, also benefits the interaction with an aqueous solution as HF.
Especially when using a high angular resolution for small circles the overlap is significant in the writing scheme of Fig. 6.2(b). Comparing the etch rate for single rods with different angular discretization allows to quantify the effect for this certain routine.

When moving the focal spot of the laser deeper into the silica, depth dependent spherical aberration becomes relevant. The ellipse is elongated along the beam axis which is illustrated in

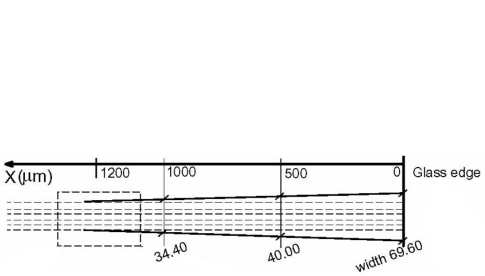

(a)

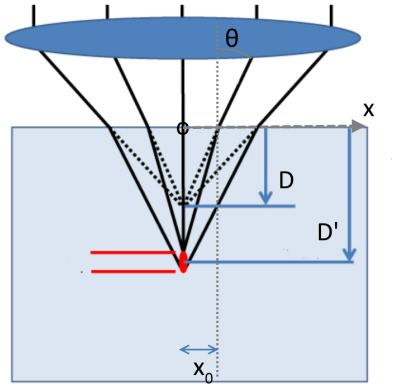

(b)

Figure 7.1: (a) Sketch of the written pattern of a tunnel from the glass edge into the bulk (dashed line) and the resulting shape after etching (solid line) [5]. Instead of an identical cross sectional width along the x axis, a conical shape is observed. (b) Schematic of depth dependent spherical aberration by ray optics [35]

Fig. 7.1(b) using ray optics.
A bundle of rays is focused onto a spot in distance D below the interface if the two media had the same index of refraction. When increasing n_2 each ray is refracted towards the normal axis and thereby changes its intersection with the optical axis y. The ray which hits the interface under the angle

$$\theta = \arctan(x_0/D)$$

is refracted according to Snell's law, $\sin\tilde{\theta} = \frac{n_1}{n_2}\sin\theta$. It intersects the y-axis at

$$D'(x_0) = \left(\frac{n_1}{n_2}\sin\theta\right)^{-1} x_0\cos\tilde{\theta} = \frac{D}{n_1/n_2}\sqrt{1+\left(\frac{x_0}{D}\right)^2\left(1-\left(\frac{n_1}{n_2}\right)^2\right)}$$

where the angle of refraction $\tilde{\theta}$ is replaced by Snell's law, the above expression for incident angle was inserted and trigonometric identities applied. For an incident light cone with half opening angle α, penetrating the silica from air, the outermost ray crosses the optical axis at

$$D'(x_0^{(out)}) = Dn_{\text{glass}}\sqrt{1+\tan^2\alpha\,(1-(1/n_{\text{glass}})^2)}. \tag{7.1}$$

The on-axis ray has its virtual focus at $D'(0) = Dn_{\text{glass}}$ such that the overall spot, located at $(D'(x_0^{(out)}) + D'_0)/2$, spans over a length of

$$\Delta = Dn_{\text{glass}}\left(\sqrt{1+(1-(1/n_{\text{glass}})^2)\tan^2\alpha}-1\right) \tag{7.2}$$

Due to this elongation the peak intensity decreases as well. Huang et al. [35] studied numerically and experimentally the depth range over which the aberrations are important. By adjusting the incident pulse energy a uniform focal shape was achieved for a depth range of 400 µm with a numerical aperture (NA) of 0.4. Including adaptive optics for aberration corrections, experimentally studied first for optical memory devices [37], the quality of the laser spot improves significantly and allows to write channels at depths up to 1.2 mm [35]. The microscope image in Fig. 7.2 shows the difference between uncorrected and corrected beam spots.

The lens used in the current setup has a NA of 0.4. When writing at a depth of $D' = 500\,\mu\text{m}$ the elongation is estimated as 25 µm, which is longer than the defined longitudinal spot size.

7.1.3 Writing Strategy

Appropriate parameters for the discretization will affect the outcome as well. As shown in Fig. 6.8(d), the bulk silica between the bottom and the center layer is not removed. In 6.10 the vertical walls in the second lowest layer illustrate the discretization as well.

Figure 7.2: Transmission microscope image of waveguides fabricated at a depth 1.0 mm. The left three waveguides were aberration corrected, whereas the right three were aberration uncorrected. The central marker splitting the two sets is a region of laser induced damage. [35]

For instance, in Fig. 6.8(d) and 6.10 one observes that the core is not fully etched which can result from the choice for Δx_p.
On the other hand, reduced etching time and HF concentration compared to layers closer to the surface could explain the residual bulk glass.

As the examples above show, the discretization parameters also play a significant role in optimizing the manufactured outcome. Up to now, the angular resolution of the cylinders predominantly determines the surface roughness. This should be the starting point for a detailed analysis of the strategy parameters.

7.2 Proposal for Detailed Cylinder Analysis

The manufactured structures have shown that many aspects of the process remain unclear and require a better analysis of the effects. Here, we propose an experimental roadmap for improvements.

Rods with circular cross section As a first step multiple rods with varied ellipse parameters a_e, b_e will be written close to the surface at the same depth, using fixed laser parameters. In analogy to the latest fabricated structure, Fig. 6.10, this allows to optimize the height-to-width ratio towards 1. With the optimal parameters the cross sectional shape of a rod can be compared to a circle. Image processing allows to extract the shape and a fit to the circle can be applied. If the fit error is in the order of the surface roughness the ellipse parameters a_e, b_e are optimal.

Surface roughness So far, the discretization of the half circle dominates the surface pattern of a single rod. Decreasing the angular step size will lower the surface ripples. At which discretization is the surface roughness saturated such that the spot size and nanogratings dominate the effect? Arbitrary large angular resolution is not preferred because of increasing stress.

Depth dependence of circularity With optimized ellipse parameters and discretization multiple cylinders will be written vertically stacked. How will the rod's cross section change depending on the depth? At which depth will the elongation of the focal spot play a role? Varying the pulse energy may correct for spherical aberrations. Up to which depth is this possible?

Variation of cross section along cylinder axis How much does the radius or the height-to-width ratio change along the cylinder axis? Close to the sample surface it is expected that the cross section does not change within the range of uncertainty since the acid etches continuously along the axis. As you go deeper into the bulk it is not clear whether the average etch rate along the z axis is faster inside the cross sectional plane, or in the front cutting wall which makes the rods free standing. If the etching along the vertical wall is much faster the rods will mainly be etched by diffusion along the cylinder axis instead of diffusion along the vertical axis. This will depend on the writing strategy and describes a complex diffusion problem.

Adaptive aberation correction Neil et al. [38, 37] described and set up a wavefront sensor for Zernike aberration modes in order to correct them adaptively in a lithium niobate ($LiNbO_3$) crystal. A spatial light modulator was used to preshape the beam's wave fronts, allowing corrections up to a depth of 1 mm. Huang et al. [35] applied this setup for

micromanufacturing of waveguides in fused silica. Implementing the adaptive aberration correction in the current setup will allow to write micro structures deep in the bulk with similar precision as structures written close to the surface. The mentioned experiments indicate that writing throughout the whole sample of 1 mm thickness should be possible.

Circular hollow core channel As the center of the PhC structure is written as a hollow cylinder the geometry should be studied separately in detail. Again, the surface quality achieved with optimal angular discretization is of great importance. An interesting device by itself may be a vertical microchannel from the surface into the bulk, bended towards a horizontal channel, and bended again towards the surface again, similar to an unrounded U-pipe.

Having studied the base parts of the hexagonal waveguide structure and limitations of the setup in more detail a more sophisticated approach can be taken to manufacture the waveguide.

7.3 Photonic Band Gap Design

Fused silica/air photonic band gap fibers have been studied intensively for optical frequencies in the past. Using different cladding materials, such as PMMA, guidance of terahertz in a hollow core photonic band gap fiber has been demonstrated [39]. ARROWs provide a different guiding geometry in which high index inclusions surround the low-index core. Both structures make use of band gap guidance by introducing a defect which localizes one or more modes inside the gap. In general, the properties of a defect, such as number of modes, mode profiles and confined energy, can be directly computed numerically. In contrast, the inverse problem of designing a structure with desired PBG properties is very difficult.
In this thesis, an approach was taken to design a single-mode waveguide with TM-like field pattern.

7.3.1 Two-Dimensional Photonic Crystal Waveguide

In the first approach, chapter 5.1 and 5.2, the 2D hexagonal PhC of silica rods was examined with respect to in-plane wave vectors. By removing one of the silica rods a TM-mode is localized which concentrates 44 % of its energy inside the defect. Including out-of-plane propagation along the continuous axis, the mode dispersion $\omega(k_z)$ does not intersect the SOL line inside the band gap, meaning that no trapped mode exists with matching phase velocity to accelerate relativistic particles.

Considering the 3D mounted structure with large aperture, Fig. 5.8(a), the resonant mode is confined to the core and originates from the defect dispersion in Fig. 5.15. At this frequency $k_z = 0.172\pi/a$ which gives a wavelength of $\lambda = 5.9a$. This does not agree with the wavelength analysis in chapter 5.7. While the peak in λ-space, Fig. 5.10, is poorly defined because of low resolution, it is far away from $\lambda \approx 6a$. The phenomenon of shifted wavelength may originate from the presence of the mounting plates and requires a more detailed analysis.

To make use of the localized mode with $k_z = 0$ a cavity design is necessary. This can be attained by encapsulating the crystal with metal walls in $\lambda/2$ distance along the z-axis [40] by which TM modes are confined. This is analogous to the RF pillbox design with a cladding replaced by the PhC. This does not represent a suitable solution with respect to the goal of an

all-dielectric structure.

Additionally, the mounting plates introduce a new periodicity along the z axis. Arbitrary plates may distort the field in a unintended way such that some frequency ranges are prohibited for mode propagation along the waveguide axis. Such a band gap could be the origin of the mode depicted in 5.7 whose frequency of $f = 0.29$ was outside the band gap range. As shown, the field extends through the transverse crystal but is confined in longitudinal direction. In this case it would not be a resonance but a rather an evanescent wave whose length scale is a few orders of magnitude larger than the structure length under study, such that the decay could not be observed anymore.
Apart from that it could be a mode located at the band edges where the group velocity approaches zero. As both explanations indicate, a detailed analysis of the band structure of the mounting plates is required. By variation of the thickness and the distance the dispersion $\omega(k_z)$ could in principle be tuned for properties such phase and group velocity. In practice, this approach becomes challenging as one has to start with trial and error based parameters.
This study should be conducted after having a PBG based waveguide with out-of-plane propagation which is why it was not considered here anymore for the first design.

7.3.2 Out-of-Plane Propagation

To find a trapped mode with out-of-plane propagation k_z the defect in the crystal was modified. Removing seven rods, instead of one, shifted a state in the gap at large k_z, closer to the light line. As they do not intersect, a different type of defect is needed which should not introduce more than one localized mode.
For photonic band gap fibers the maximum number of modes N_{max} scales approximately with [24, 41]

$$N_{max} \approx \frac{1}{2}\left(\frac{\omega_0 a}{c}\right)^2 \left(1 - \frac{k_U^2(\omega_0)}{\frac{\omega_0^2}{c^2}}\right) \cdot \left(\frac{r_D}{a}\right)^2, \tag{7.3}$$

where a is the lattice constant, ω_0 the lower frequency at which the SOL line enters the gap and k_U the wave vector component at which the upper gap edge $\omega_U(k_z)$ crosses the fixed frequency ω_0, $\omega_U(k_U) = \omega_0$. r_D is the radius of the defect.
For instance, the Lin structure [7] has the following parameters: (i) $r_D = 0.35a$ (ii) $\omega_0 = 8.05c/a$ (iii) $7.8\mathrm{a}^{-1}$, for which $N_{max} = 2$ were found. In fact, when the supercell bands are computed two localized modes arise in the gap.
Looking at the derivation of this equation presumes air-guided modes, in which the power propagates predominantly in air. Above the SOL line, trapped modes are air-guided, while below, the guiding mainly occurs in silica. At the intersection a transition from air- to silica-guiding occurs. For the modes of interest, air-guided modes are not desired if they have maximum power on-axis because this implies a non-zero magnetic field. Therefore the above number of modes is not applicable here.
Further, surface termination at the core boundary takes a crucial role in the formation of defect modes [42].

As no band gap modes were found for a core as large as a single rod, $r_D = r$, the second ring of rods around the core was modified. By varying the rod radius r_2 of the neighboring rods the surface termination has been modified in terms of surface curvature.
By lowering r_2, four partially degenerate bands enter the gap. This can be understood in the scalar limit of LP-modes (linearly polarized)[10, p. 163]. In the limit $k_z \to \infty$, resp. in the short

wavelength limit, each rod can be regarded as isolated, surrounded by vacuum. The solution to Maxwell's equations are fully determined by a scalar function ψ, which is separated in a radial and an angular part whereas the radial dependence is given by Bessel functions [43, Sec. 8.8]. When the rods are brought together resp. the wavelength is increased, overlapping states are formed in analogy to the tight-binding model in solid-state physics. As k_z is finite, the continuous radial symmetry of the scalar limit breaks and the scalar state ψ splits into two vectorial states. In case of a doubly degenerate scalar state four corresponding vectorial states emerge in the finite k_z case.
The same argument holds for the core region. In the limit of large k_z the localized state is scalar, and breaks down in vectorial modes for finite k_z.

In the case of rod cutting surface termination, Fig. 5.20(a) the asymptotical behavior $k_z \to \infty$ can already be observed for the defects when approaching $k_z = 0.9$. The upper family of modes consists of two non-degenerate and a doubly degenerate mode. The same holds for the lower mode family at approximately $\omega \approx 0.82\pi c/a$.

To isolate a single defect mode from the other states of the same scalar ψ, the k_z region has to be chosen such that the other vectorial modes still reside in the bands, corresponding to leaky modes. In Fig. 5.20(a) this is the case at $k_z = 0.58$, but this point is far from the SOL dispersion. The opening of the band gap is shifted towards the light line by increasing the rod radius r of the PhC.

The crystal with $r = 0.38a$ and $r_D = 0.97a$ supports an accelerating mode at $f = 0.52c/a$ with a characteristic impedance of $Z_C = 99\,\Omega$. The longitudinal power flow occurs mainly between the second and the third lattice cell, where the field reaches its maximum. Those are not surface states because the intensity $\mathrm{Re}\, S_z$ does not decay into air exponentially.

Another important figure of merit for the point of operation is the group-velocity dispersion, $d^2\omega/dk^2$, which has not been investigated here. The variation of the dispersion slope causes pulses to spread. For interaction with particle bunches the pulse distortion should be small over a distance of the interaction length.

7.4 Finite Waveguide

Simulations of the truncated crystal to extract the Q-factor and propagation of the electric field through the finite structure have shown that still more than a single mode are supported by the waveguide.
The Q-factor for both modes increases significantly with increasing number of surrounding lattice cells. The loss due to truncation of the infinite crystal is small and the resonances are very well localized in the spectrum. Only few lattice cells are needed to confine the electromagnetic wave. For instance, $Q \sim 10^4$ is achieved with only $n_{\mathrm{cells}} = 12$.
An open waveguide has been excited at one end with a Gaussian dipole source. The output longitudinal field $E_z(0, 0, L/2, t)$ at the opposite end the waveguide has shown two significant pulses. A rough estimation of the group velocity of the first pulse agrees with the calculation from the slope in the dispersion. A proper extraction of the group delay $\tau_g(\omega)$ was not possible because the signal contained too much noise.
After the main pulses have passed the output, residual signal from the propagation was observed in the temporal profile. As largest amplitude in the tail is just smaller by a factor of three than

the initial output pulse, it contributes significant noise to the spectrum. A possible origin for this tail in $E_z(0, 0, L/2, t)$ may be boundary effects as the wave couples into free space at the point of record. Additionally, the mounting of the glass rods also modify the waveguide modes.

To simplify the output field simulation, the propagation of the pulse inside the waveguide has been examined far away from the open ends. A second peak of the same strength as the first is not observed, but a small residual tail remains.

As a next step the mountings have be introduced into the infinite long waveguide, which allows to study the losses and mode distortion from the glass plates. Finally, the simulations done here will be repeated with a longer structure.

7.5 Future Improvements to the Designed Structure

Because of strong fields inside the dielectric rods, material losses become relevant. To quantify the effect, time domain simulations including the absorption index from chapter 3 have to be conducted.

The design may be improved further by investigating other types of defects which have not been studied here. The diversity of defect geometry is rather unlimited. For instance, Bauer et al. [44] optimized the position of dielectric rods for maximal mode confinement in a cavity while keeping their shape fixed. The result is shown in Fig. 7.3. Gennaro et al. [45] studied photonic quasi crystals and a hybrid structure including metal rods on the outside of the cavity. Two additional types of defects have been tested shortly during this work but not appropriately detailed.
The first defect also removes the rods from the third lattice cell, consisting of a core of 19 missing rods. Potentially, a larger defect can lead to more modes in the gap, but regarding the change from 1 to 7 missing rods in Fig. 5.16(a), only a single defect mode was added to the gap.
Second, by centering the defect between three rods, the defect can be smaller while still modifying the surface termination of three rods. This will break the six-fold symmetry of the structure. If the SOL mode resembles the surface termination it will be little effected from the symmetry breaking.

For a proof of concept device the proposed design is sufficient. In order to excite the TM-like monopole field, a coupler must modify the incident free-space mode for matching field symmetry.

7.6 Potential Coupling Designs

For the cylindrical loaded waveguide demonstrated by Nanni et al. [2], a segmented half waveplate was used to convert the free-space linearly-polarized pulse into radial polarized one. The radial polarizations couples well to the TM_{01} mode. The accelerating mode of the proposed design does not exhibit the continuous, but a six-fold rotational symmetry. Whether a nonparaxial radially polarized THz beam can be matched to the hexagonal symmetry [3] requires additional studies.

To attain a non-paraxial field distribution, a THz axicon can also be used. In Thz imaging an axicon made off high density polyethylene (HDPE) has been tested to obtain a zeroth order

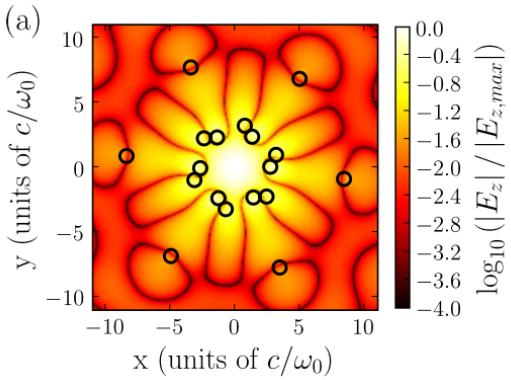

Figure 7.3: Rod positions of an optimized structure for maximal mode confinement, starting from the hexagonal PhC design [44].

quasi-Bessel beam. [46]. As the zeroth order mode is concentrated in the center, a modification can be achieved by incident Laguerre-Gaussian beams [47]. To the best of our knowledge, higher order Bessel modes have not been studied for terahertz.

By cleaving the end of a cylindrical loaded waveguide at an angle, THz extraction has been demonstrated using particle wakefields. Ultra-relativistic electrons with 60 MeV pass through such waveguide by which the TM_{01} mode is excited. An appropriate cut angle at the exit port allows for efficient free-space coupling.
In principle this should also work the other way round because of time reversal symmetry of Maxwell's equations. An incident THz is focused onto the cut aperture under the matching angle. The TM_{01} mode is excited and propagates inside the waveguide.

Finally, cylindrical horn antennas have also been studied for coupling a free-space THz beam into the TM guided mode of cylindrical waveguide [48].
Because of the novel design of the ARROW waveguide, each proposed coupler has to be analyzed by numerical studies with respect to coupling to the hexagonal field pattern.

7.7 Realistic Parameters for an Experiment

The physical quantities used throughout this thesis are given in terms of relative units with the lattice constant as reference parameter. In principle, as long as the resulting frequency is in the range of constant ε introduced in chapter 3, one parameter can be chosen arbitrarily. For a more sophisticated choice the feasibility of manufacturing as well as availability of laser sources and material absorption has to be taken into account.
From the manufacturing point of view the height is limited due to deep writing in the bulk. With increasing writing depth the focus spot is less defined. For the laser setup used during this project, a depth of approximately 500 µm is acceptable.
Further, the longitudinal size of the focal spot $\approx 20\,\mu m$ limits the distance between the rods of different layer, leading to a minimal lattice constant of $a_{\min} = 75\,\mu m$.
To attain good confinement with many surrounding lattice cells n_{cells} the lattice constant a and the rod radius r has to be decreased to keep the height in the given range. Small a also in-

cludes larger frequency and therefore larger absorption (see chapter 3). Therefore, two designs are proposed, listed in table 7.1. Design 1 is based on the limitation by longitudinal focal size, $a = 75\,\mu m$. For design 2 the frequency of 1.8 THz is chosen as the free parameter. A novel tunable strong-field THz laser [4] allows extraction of narrow band pulses at $f = 1.80\,THz$ with bandwidth $\Delta f \approx 200\,GHz$, energy $E = 20\,\mu J$ and field strength $200\,MV/m$.

An open question remains whether the new design with larger rods compared to those in chapter 5.2 can be machined. Apart from the considerations of the focal spot and writing depth, etching introduces additional difficulties because of the diffusion in unexposed silica.

Parameter	In reference units	Design 1	Design 2
Lattice constant a	a	75 µm	87 µm
Radius r	0.38 a	29 µm	33 µm
Defect radius r_D	0.97 a	73 µm	84 µm
n_{cells}	-	4	4
Width w	$2n_{\text{cells}}a + 2r$	657 µm	759 µm
Height h	$\sqrt{3}n_{\text{cells}}a + 2r$	577 µm	666 µm
Guided mode frequency f	0.52 c/a	2.08 THz	1.80 THz

Table 7.1: Two proof of principle proposals for design parameters of the photonic band gap structure. A larger number of lattice cells is desirable but not achievable with the current fabrication setup. For reference, the relative units are also provided. All size values rounded to 1 µm

8 Conclusion

A new type of terahertz waveguide suited for a confined TM-like mode is proposed. The confinement is achieved by photonic band gap guidance using cylindrical fused silica rods. The hollow core introduces a defect in the photonic crystal which binds electromagnetic states. A difficulty arises in isolating a single TM-like mode to reduce energy loss due to coupling between the defect modes.
The two-step manufacturing process of direct laser writing in combination with aqueous etching provides an new approach for monolithically integrated devices. For deep structures the writing procedure becomes challenging and requires a detailed analysis of each structural component of the device before assembly. Especially bulk etching requires a sophisticated writing procedure to compensate for etching of unexposed silica.

As a next step further detailed analysis of the pulse propagation and transmission through the waveguide is needed. The current studies closed with noisy results for the group delay in the finite structure. It is an open question which features in the output signal originate from the finite extent and which originate from the mountings.
Finally, a coupler should be designed which suppresses obstructive modes by matching only the desired symmetry. Having such a coupler, the propagation of a terahertz pulse through the structure can be characterized experimentally.

A Acknowledgments

For the opportunity to write my master thesis at the Paul-Scherrer-Institut (PSI) I have to thank Andreas Adelmann and Rasmus Ischebeck. Throughout the course of this project they supported me with many motivating discussions and ideas how to proceed when reaching a deadlock. I also thank Micha Dehler who suggested different approaches to test my design and how to adjust the new waveguide design. I learned a lot from his understanding of computational electrodynamics.
For having me at the Galatea lab, École polytechnique fédérale de Lausanne (EPFL), I would like to express my gratitude to Yves Bellouard. It was a pleasure for me to discuss and to work on the microfabrication with him, David Lambelet and Sacha Pollonghini, who gave me many insights to approach the bulk etching problem. For performing the acid bath I would also like to thank Pieter Vlugter as well as Sacha Pollonghini. Sometimes many attempts had to be made to get the sample sufficiently etched. Additional difficulties occurred in handling the software. I am thankful for the help from Benedikt Braun in tackling those issues.
For suggestions on coupling design I express my gratitude to Paolo Craievich. Although I didn't reach the point to study the coupler it was helpful for understanding the requisites and figure of merits.
Further, I like to thank Elisabeth Müller who trained me on the electron microscope. The SEM images provided insight in deep features below the sample surface.
Finally, I am grateful for the help from Nick Sauerwein on how to align optics devices. In the end, setting up a Terahertz characterization experiment was not doable because of the lack of the structure under test. But the attained knowledge is very helpful for future.

B Illustrative Reasoning of Preferred Sphere-like Brillouin Zone

As illustrated in Sec. 2.5 an arbitrarily small perturbation to the dielectric contrast from 1 leads to the opening of a band gap in a one-dimensional crystal. In higher dimensions this is not the case as the size of the Brillouin zone is not spherical. To illustrate the reasoning consider a quadratic lattice in two dimensions with lattice constant a along the x and the y axis. The Brillouin zone terminates at $k_x = \pi/a$ and $k_y = \pi/a$ along the axes in the reciprocal space. Applying the phenomenological approach from section 2.5 to both directions separately results in the same band gap at $\omega \approx \frac{c}{\sqrt{\varepsilon}}\ \pi/a$. But for the Brillouin zone edge along the diagonal direction, $\mathbf{k'} = \pi/a\,(\hat{\mathbf{x}} + \hat{\mathbf{y}})$, the magnitude of the wave vector is $|\mathbf{k'}| = \sqrt{2}\pi/a$. The gap will open up at

$$\omega \approx c|\mathbf{k'}|/\sqrt{\varepsilon} = \tfrac{\sqrt{2}}{\sqrt{\varepsilon}}\ c\pi/a.$$

The dispersion relations along these two different directions are shown in Fig. B.1(c). If the gap sizes at $\mathbf{k} = \pi/a\ \hat{\mathbf{x}}$ and $\mathbf{k'} = \pi/a\ (\hat{\mathbf{x}} + \hat{\mathbf{y}})$ are not sufficiently large, as shown, they don't overlap and the crystal does not exhibit an omnidirectional band gap, meaning a forbidden frequency range for all directions.
In contrast to the one-dimensional case, 2D and 3D crystals require a minimal dielectric contrast for the opening of a complete band gap as the gap sizes illustrated in Fig.B.1(c) increase with larger dielectric contrast. For a given dielectric contrast one would always find a band gap if the Brillouin zone edges were equally distant in all directions. As a spherical Brillouin zone is not possible, it is favorable to have a zone shape as close as possible to a sphere. In 2D the trigonal lattice exhibits the most sphere-like Brillouin zone while in 3D the Brilluoin zone of the FCC crystal is closest to the sphere.

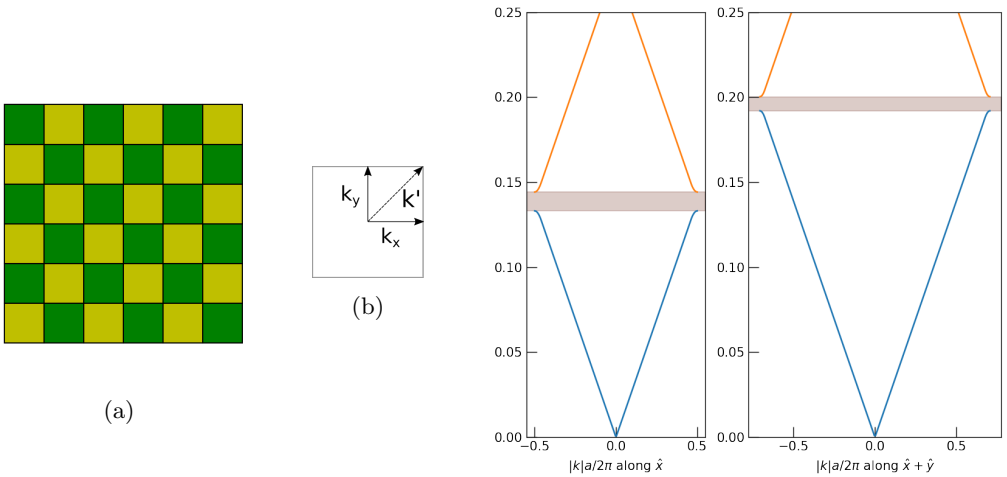

(a) (b) (c)

Figure B.1: (a) Two dimensional square lattice of two media with slightly different permittivity ε such that one medium is treated as perturbation to the homogeneous medium. This is in analogy to the one-dimensional approach in Sec. 2.5. (b) Brillouin zone of the square lattice and the directions in $\mathbf{k}$-space along which the dispersion is studied. (c) Directional band diagrams along $\hat{\mathbf{x}}$ and $\hat{\mathbf{x}} + \hat{\mathbf{y}}$.

C Perfectly Matched Layers in Transmission Simulation

The importance of a sufficiently thick perfectly matched layer for the transmission simulations in chapter 5.8 is qualitatively reported here for the large aperture. The waveguide consists of rods of $r = 0.2a$ radius, truncated at $n_{cells} = 4$ in the transverse plane, and nine mounting plates of $0.5a$ thickness in $5a$ distance along the waveguide axis. Again, a hollow core cylinder of the same size was used as reference geometry. The input pulse was centered at $f = 0.47$ with $\Delta f = 0.1$.

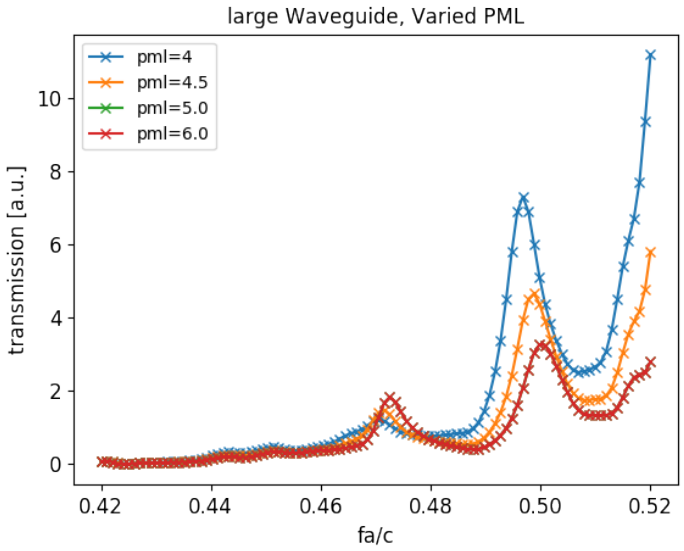

Figure C.1: Change in the transmission spectrum depending on the size of the perfectly matched layer.

D Spectrum of On-Axis Field in 2D

In sec. 5.13 resonant modes of an effectively 2D truncated crystal with $r = 0.38a$, $r_D = 0.97a$ and periodic boudaries along z were studied. Here, the on-axis field $E_z(0,0,0)$ for $n_{\text{cells}} = 10$ is analyzed after the sources have turned off. The time sequence of E_z is shown in Fig. D.1(a). The field is Fourier transformed to find resonances in the spectrum. The peaks in Fig. D.1(b) indicate that two resonant modes exist instead of the expected single-mode.
For comparison, the same result is presented for a structure with $r = 0.39a$ in Fig. D.2

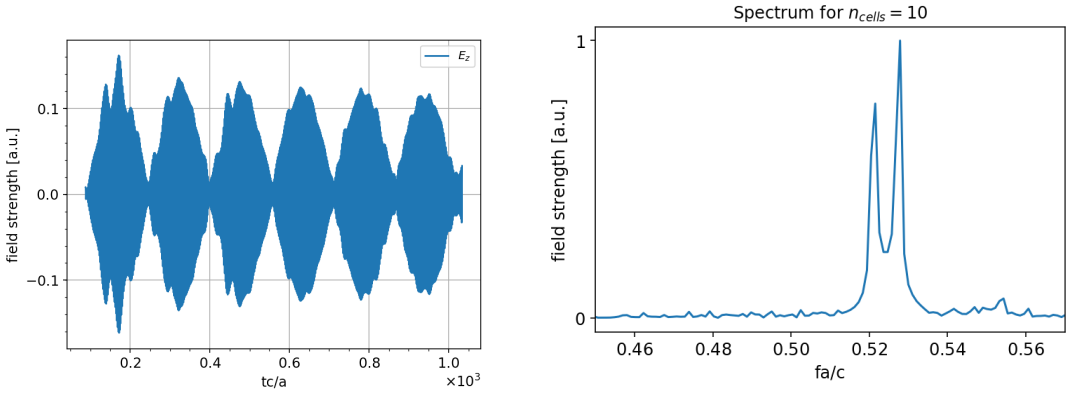

(a) (b)

Figure D.1: (a) $E_z(0,0,0,t)$ after the sources turned off. (b) Normalized spectrum of the on-axis longitudinal field. Radius of the rods: $r = 0.38a$. Defect radius: $r_D = 0.97a$

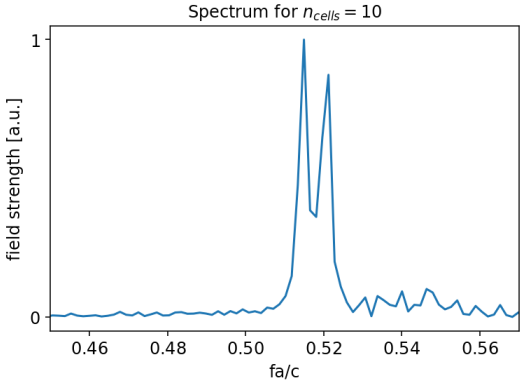

Figure D.2: Spectrum for a truncated crystal with radius $r = 0.39a$, defect $r_D = 0.97a$, number of cells $n_{\text{cells}} = 10$

E On-Axis Propagation in Infinitely Extended Structure

In chapter 5.14.3 a FTDT simulation of an infinitely long waveguide with the redesigned photonic band gap structure has been discussed. Here, the outcome from this simulation are presented.

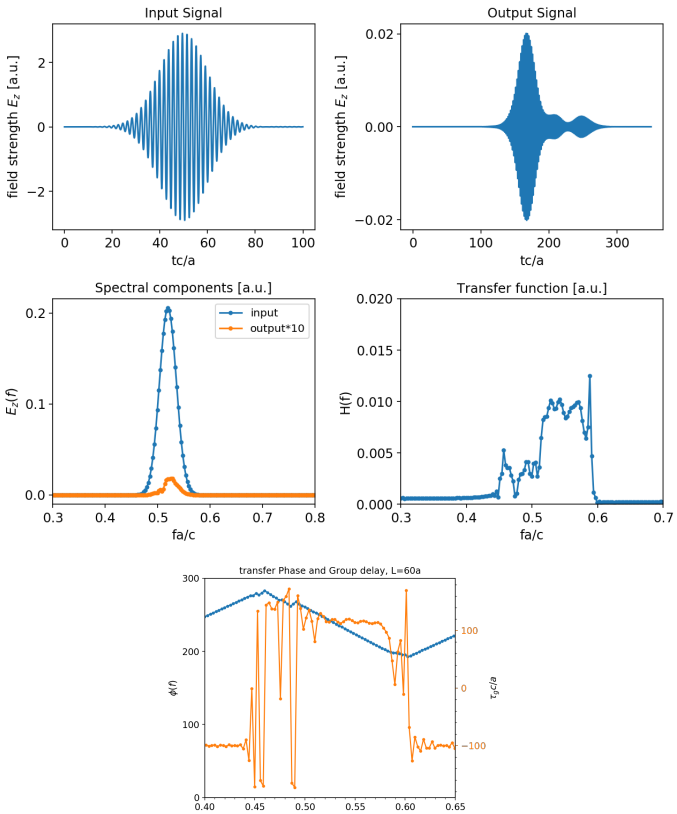

Figure E.1: (a) On-axis field $E_z(0, 0, -L/2, t)$ generated by the source. (b) Field $E_z(0, 0, L/2, t)$ after propagation over a distance of $60a$ (c) Spectrum at source and after propagation, last one multiplied by a factor of 10 (d) Absolute value of transfer function $H(\omega)$. (e) Phase of the transfer function and Group delay $\tau_g(\omega)$.

F Structural Components for Writing Procedure of Hexagon

In addition to the cylinder sampling in Fig. 6.2(b), section 6.2 separate routines are needed for bulk sampling. Here, the different components are presented.

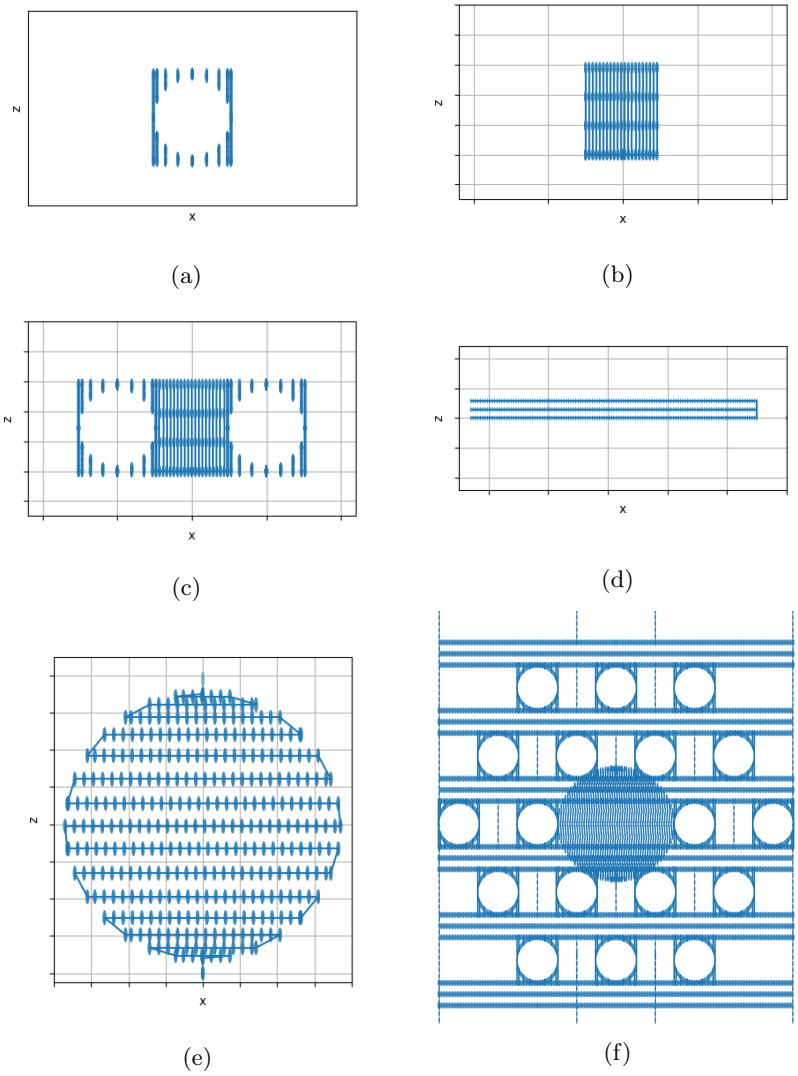

Figure F.1: F.1(a) Bulk etching routine around a single cylinder, parametrized with an angular resolution m_α. The step size in z is given by the ellipse shape. F.1(b) **In-layer** bulk etching between the rods, parametrized by a horizontal m_x and a vertical resolution m_z (number of steps). F.1(c) First and second routines combined for in-layer bulk etching.F.1(d) **Between-layer** bulk etching. Like the in-layer routine, the shape is a cuboid, but the between-layer routine uses a different resolution n_x, n_z. F.1(e) Volume sampling for a cylindrical hole. Two discretization parameters are applied, the angular resolution p_α and Δx_p as the steps size between neighboring lines in the xy plane. F.1(f) Assembled writing strategy. For illustrative purposes the in-layer bulk routine uses only two step in x-direction, leading to a wall between two cylinders. Also the other resolution parameters are set to a low value. When applied to manufacturing, they are set to larger values.

G Overview of Studied Photonic Crystal Defects

Apart from the configurations of the hexagonal lattice mentioned in the thesis, the following have been studied. The field E_z was output for every step to check the mode manually. The number of computed bands was always 50 while a supercell size of 8 lattice sites was used.

Fixed quantities	Varied quantity	Result
$k_z = 0.8, r = 0.2a$, $r_D = 1.25a$,	r_2 from $0.16a$ to 0.49, $\Delta r_2 = 0.03a$	Best phase velocity matching monopole mode at $r_2 = 0.16a$. Many other defect modes.
$k_z = 0.8, r_2 = 0.16a, r_D = 1.25a$	r from $0.21a$ to $0.29a$, $\Delta r = 0.01a$	The monopole mode is not localized anymore for $r = 0.28a$. The monopole's frequency changes from 0.794 at $r = 0.24$ to 0.784 at $r = 0.27$. The energy in the core was not computed
$k_z = 0.52, r = 0.38a, r_2 = r$	r_1 from $0.38a$ to $0.0a$	Same behavior as for $r = 0.24a$ in chapter 5.11. Conducted to check validity of binding a dipole mode for different rod size r.

H External Ressources

CAD files for the woodpile crystal can be found at https://www.thingiverse.com/thing:2509695. The first attempt of a two-dimensional waveguide is uploaded as 3D model at https://www.thingiverse.com/thing:2742789.

The scripts written for the simulations are published at https://gitlab.psi.ch/kellermeier_m/Reproducibility-2D-PBG-Structure-for-THz-driven-acceleration while the functions developed for the laser writing are documented and hosted at https://gitlab.psi.ch/kellermeier_m/Drawing-mounted-Hexagonal-PBG/tree/bulk_etching_vertically/docs.

Bibliography

[1] E. A. Peralta. Demonstration of electron acceleration in a laser-driven dielectric microstructure. *Nature*, 503.7474:91–94, 2013.

[2] E. A. Nanni, W. R. Huang, K.-H. Hong, K. Ravi, A. Fallahi, G. Moriena, R. J. Dwayne Miller, and F. X. Kärtner. Terahertz-driven linear electron acceleration. *Nature Communications*, 6:8486 EP –, Oct 2015. URL http://dx.doi.org/10.1038/ncomms9486. Article.

[3] R. J. England, R. J. Noble, K. Bane, D. H. Dowell, C.-K. Ng, J. E. Spencer, S. Tantawi, Z. Wu, R. L. Byer, E. Peralta, K. Soong, C.-M. Chang, B. Montazeri, S. J. Wolf, B. Cowan, J. Dawson, W. Gai, P. Hommelhoff, Y.-C. Huang, C. Jing, C. McGuinness, R. B. Palmer, B. Naranjo, J. Rosenzweig, G. Travish, A. Mizrahi, L. Schachter, C. Sears, G. R. Werner, and R. B. Yoder. Dielectric laser accelerators. *Rev. Mod. Phys.*, 86:1337–1389, Dec 2014. doi: 10.1103/RevModPhys.86.1337. URL https://link.aps.org/doi/10.1103/RevModPhys.86.1337.

[4] C. Vicario, A. V. Ovchinnikov, O. V. Chefonov, and C. P. Hauri. Multi-octave spectrally tunable strong-field terahertz laser. *arXiv:1608.05319*, 2016. URL https://arxiv.org/abs/1608.05319.

[5] Y. Bellouard, A. Said, M. Dugan, and P. Bado. Monolithic three-dimensional integration of micro-fluidic channels and optical waveguides in fused silica. *MRS Proceedings*, 782, 2003. doi: 10.1557/PROC-782-A3.2.

[6] B. Cowan. *Photonic crystal laser-driven accelerator structures*. Doctoral dissertation, Stanford University, 2007. URL https://arxiv.org/pdf/0708.3206.pdf.

[7] X. E. Lin. Photonic band gap fiber accelerator. *Phys. Rev. ST Accel. Beams*, 4:051301, May 2001. doi: 10.1103/PhysRevSTAB.4.051301. URL https://link.aps.org/doi/10.1103/PhysRevSTAB.4.051301.

[8] I. Staude, C. McGuinness, A. Frölich, R. L. Byer, E. Colby, and M. Wegener. Waveguides in three-dimensional photonic bandgap materials for particle-accelerator on a chip architectures. *Opt. Express*, 20(5):5607–5612, Feb 2012. doi: 10.1364/OE.20.005607. URL http://www.opticsexpress.org/abstract.cfm?URI=oe-20-5-5607.

[9] S. Atakaramians, S. Afshar, T. M. Monro, and D. Abbott. Terahertz dielectric waveguides. *Adv. Opt. Photon.*, 5(2):169–215, Jun 2013. doi: 10.1364/AOP.5.000169. URL http://aop.osa.org/abstract.cfm?URI=aop-5-2-169.

[10] J. Joannopoulos, S. Johnson, J. Winn, and R. Meade. *Photonic Crystals: Molding the Flow of Light, Second Edition*. Princeton University Press, 2011. ISBN 9781400828241. URL http://ab-initio.mit.edu/book.

[11] R. Kitamura, L. Pilon, and M. Jonasz. Optical constants of silica glass from extreme ultraviolet to far infrared at near room temperature. *Applied Optics*, 46(33):8118, 2007. ISSN 0003-6935. doi: 10.1364/AO.46.008118. URL https://www.osapublishing.org/abstract.cfm?URI=ao-46-33-8118.

[12] R. Kitamura, L. Pilon, and M. Jonasz. Optical constants of silica between 30 nm and 1,000 microns near room temperature, 2007. URL https://www.seas.ucla.edu/~pilon/downloads.htm. Accessed: 2017-09-10.

[13] S. F. Busch, M. Weidenbach, M. Fey, F. Schäfer, T. Probst, and M. Koch. Optical properties of 3d printable plastics in the thz regime and their application for 3d printed thz optics. *Journal of Infrared, Millimeter, and Terahertz Waves*, 35(12):993–997, Dec 2014. ISSN 1866-6906. doi: 10.1007/s10762-014-0113-9. URL https://doi.org/10.1007/s10762-014-0113-9.

[14] Y. Lee, Y. Hao, Y. Zhao, and C. G. Parini. On the design of millimetre wave ebg resonator antenna based on woodpile structure. *IET Conference Proceedings*, pages 149–152(3), January 2006. URL http://digital-library.theiet.org/content/conferences/10.1049/ic_20060400.

[15] K. Wootton, R. Assmann, D. Black, R. Byer, B. Cowan, H. Deng, T. Egenolf, R. England, S. Fan, J. Harris, I. Hartl, P. Hommelhoff, T. Hughes, J. Illmer, R. Ischebeck, F. Kärtner, W. Kuropka, Y. J. Lee, A. Li, F. Mayet, J. McNeur, A. Mittelbach, P. Musumeci, U. Niedermayer, M. Qi, L. Rivkin, A. Rühl, N. Sapra, N. Schönenberger, O. Solgaard, A. Tafel, S. Tantawi, and J. Vuckovic. Towards a Fully Integrated Accelerator on a Chip: Dielectric Laser Acceleration (DLA) From the Source to Relativistic Electrons. pages 2520–2525. 8th International Particle Accelerator Conference, Copenhagen (Denmark), 14 May 2017 - 19 May 2017, JACoW, Geneva, Switzerland, May 2017. ISBN 978-3-95450-182-3. doi: 10.18429/JACoW-IPAC2017-WEYB1. URL http://bib-pubdb1.desy.de/record/329338.

[16] S. G. Johnson and J. D. Joannopoulos. Block-iterative frequency-domain methods for maxwell's equations in a planewave basis. *Opt. Express*, 8(3):173–190, Jan 2001. doi: 10.1364/OE.8.000173. URL http://www.opticsexpress.org/abstract.cfm?URI=oe-8-3-173.

[17] K. Ho, C. Chan, C. Soukoulis, R. Biswas, and M. Sigalas. Photonic band gaps in three dimensions: New layer-by-layer periodic structures. *Solid State Communications*, 89(5):413 – 416, 1994. ISSN 0038-1098. doi: https://doi.org/10.1016/0038-1098(94)90202-X. URL http://www.sciencedirect.com/science/article/pii/003810989490202X.

[18] A. Taflove and S. C. Hagness. *Computational electrodynamics: the finite-difference time-domain method*. Artech house, 2005.

[19] A. F. Oskooi, D. Roundy, M. Ibanescu, P. Bermel, J. D. Joannopoulos, and S. G. Johnson. MEEP: A flexible free-software package for electromagnetic simulations by the FDTD method. *Computer Physics Communications*, 181:687–702, January 2010. doi: 10.1016/j.cpc.2009.11.008.

[20] V. A. Mandelshtam and H. S. Taylor. Erratum:"harmonic inversion of time signals and its applications"[j. chem. phys. 107, 6756 (1997)]. *The Journal of Chemical Physics*, 109(10): 4128–4128, 1998. doi: http://dx.doi.org/10.1063/1.477013.

[21] R. Courant, K. Friedrichs, and H. Lewy. Über die partiellen Differenzengleichungen der mathematischen Physik. *Mathematische Annalen*, 100(1):32–74, 1928.

[22] V. A. Mandelshtam and H. S. Taylor. Harmonic inversion of time signals and its applications. *The Journal of Chemical Physics*, 107(17):6756–6769, 1997. doi: 10.1063/1.475324. URL http://dx.doi.org/10.1063/1.475324.

[23] R. T. Bise, R. Windeler, K. Kranz, C. Kerbage, B. Eggleton, and D. Trevor. Tunable photonic band gap fiber. In *Optical Fiber Communication Conference and Exhibit, 2002. OFC 2002*, pages 466–468. IEEE, 2002.

[24] M. N. Petrovich, F. Poletti, A. van Brakel, and D. J. Richardson. Robustly single mode hollow core photonic bandgap fiber. *Opt. Express*, 16(6):4337–4346, Mar 2008. doi: 10.1364/OE.16.004337. URL http://www.opticsexpress.org/abstract.cfm?URI=oe-16-6-4337.

[25] Y. Bellouard, A. Said, M. Dugan, P. Bado, R. S. Taylor, C. Hnatovsky, E. Simova, D. M. Rayner, M. Mehandale, V. R. Bhardwaj, and P. B. Corkum. Fabrication of high-aspect ratio, micro-fluidic channels and tunnels using femtosecond laser pulses and chemical etching. *OPTICS EXPRESS*, 12(10), 2004.

[26] Y. Bellouard, A. Champion, B. Lenssen, M. Matteucci, A. Schaap, M. Beresna, C. Corbari, M. Gecevičius, P. Kazansky, O. Chappuis, M. Kral, R. Clavel, F. Barrot, J. M. Breguet, Y. Mabillard, S. Bottinelli, M. Hopper, C. Hoenninger, E. Mottay, and J. Lopez. The femtoprint project. *Journal of Laser Micro Nanoengineering*, 2012. ISSN 18800688. doi: 10.2961/jlmn.2012.01.0001.

[27] V. Tielen and Y. Bellouard. Three-dimensional glass monolithic micro-flexure fabricated by femtosecond laser exposure and chemical etching. *Micromachines*, 5(3):697–710, 2014.

[28] T. Yang and Y. Bellouard. Monolithic transparent 3d dielectrophoretic micro-actuator fabricated by femtosecond laser. *Journal of Micromechanics and Microengineering*, 25(10): 105009, 2015.

[29] A. M. Streltsov and N. F. Borrelli. Study of femtosecond-laser-written waveguides in glasses. *JOSA B*, 19(10):2496–2504, 2002.

[30] A. Agarwal and M. Tomozawa. Correlation of silica glass properties with the infrared spectra. *Journal of Non-Crystalline Solids*, 209(1):166–174, 1997.

[31] S. Kiyama, S. Matsuo, S. Hashimoto, and Y. Morihira. Examination of etching agent and etching mechanism on femotosecond laser microfabrication of channels inside vitreous silica substrates. *The Journal of Physical Chemistry C*, 113(27):11560–11566, 2009.

[32] Y. Shimotsuma, P. G. Kazansky, J. Qiu, and K. Hirao. Self-organized nanogratings in glass irradiated by ultrashort light pulses. *Phys. Rev. Lett.*, 91:247405, Dec 2003. doi: 10.1103/PhysRevLett.91.247405. URL https://link.aps.org/doi/10.1103/PhysRevLett.91.247405.

[33] H. K. Kuiken. Etching: a two-dimensional mathematical approach. *Proceedings of the Royal Society of London A: Mathematical, Physical and Engineering Sciences*, 392(1802): 199–225, 1984. ISSN 0080-4630. doi: 10.1098/rspa.1984.0029. URL http://rspa.royalsocietypublishing.org/content/392/1802/199.

[34] H. K. Kuiken. Etching through a slit. *Proceedings of the Royal Society of London A: Mathematical, Physical and Engineering Sciences*, 396(1810):95–117, 1984. ISSN 0080-4630. doi: 10.1098/rspa.1984.0110. URL http://rspa.royalsocietypublishing.org/content/396/1810/95.

[35] L. Huang, P. S. Salter, F. Payne, and M. J. Booth. Aberration correction for direct laser written waveguides in a transverse geometry. *Opt. Express*, 24(10):10565–10574, May 2016. doi: 10.1364/OE.24.010565. URL http://www.opticsexpress.org/abstract.cfm?URI=oe-24-10-10565.

[36] M. Tomozawa. Fracture of glasses. *Annual Review of Materials Science*, 26(1):43–74, 1996.

[37] M. A. A. Neil, R. Juškaitis, M. J. Booth, T. Wilson, T. Tanaka, and S. Kawata. Active aberration correction for the writing of three-dimensional optical memory devices. *Applied optics*, 41(7):1374–1379, 2002.

[38] M. A. A. Neil, M. J. Booth, and T. Wilson. New modal wave-front sensor: a theoretical analysis. *J. Opt. Soc. Am. A*, 17(6):1098–1107, Jun 2000. doi: 10.1364/JOSAA.17.001098. URL http://josaa.osa.org/abstract.cfm?URI=josaa-17-6-1098.

[39] J.-Y. Lu, C.-P. Yu, H.-C. Chang, H.-W. Chen, Y.-T. Li, C.-L. Pan, and C.-K. Sun. Terahertz air-core microstructure fiber. *Applied Physics Letters*, 92(6):064105, 2008. doi: 10.1063/1.2839576. URL http://dx.doi.org/10.1063/1.2839576.

[40] S. L. McCall, P. M. Platzman, R. Dalichaouch, D. Smith, and S. Schultz. Microwave propagation in two-dimensional dielectric lattices. *Phys. Rev. Lett.*, 67:2017–2020, Oct 1991. doi: 10.1103/PhysRevLett.67.2017. URL https://link.aps.org/doi/10.1103/PhysRevLett.67.2017.

[41] M. J. F. Digonnet, H. K. Kim, G. S. Kino, and S. Fan. Understanding air-core photonic-bandgap fibers: analogy to conventional fibers. *Journal of Lightwave Technology*, 23(12):4169–4177, Dec 2005. ISSN 0733-8724. doi: 10.1109/JLT.2005.859406.

[42] K. Saitoh, N. A. Mortensen, and M. Koshiba. Air-core photonic band-gap fibers: the impact of surface modes. *Opt. Express*, 12(3):394–400, Feb 2004. doi: 10.1364/OPEX.12.000394. URL http://www.opticsexpress.org/abstract.cfm?URI=oe-12-3-394.

[43] J. D. Jackson. *Classical electrodynamics*. Wiley, 1962. ISBN 0-471-43131-1.

[44] C. A. Bauer, G. R. Werner, and J. R. Cary. Truncated photonic crystal cavities with optimized mode confinement. *Journal of Applied Physics*, 104(5):053107, 2008. doi: 10.1063/1.2973669. URL http://dx.doi.org/10.1063/1.2973669.

[45] E. D. Gennaro, C. Zannini, S. Savo, A. Andreone, M. R. Masullo, G. Castaldi, I. Gallina, and V. Galdi. Hybrid photonic-bandgap accelerating cavities. *New Journal of Physics*, 11(11):113022, 2009. URL http://stacks.iop.org/1367-2630/11/i=11/a=113022.

[46] Z. Zhang and T. Buma. Terahertz imaging in dielectric media with quasi-bessel beams. In *Proc. SPIE*, volume 7938, page 793806, 2011. doi: 10.1117/12.875864.

[47] D. McGloin and K. Dholakia. Bessel beams: Diffraction in a new light. *Contemporary Physics*, 46(1):15–28, 2005. doi: 10.1080/0010751042000275259. URL http://dx.doi.org/10.1080/0010751042000275259.

[48] F. Scheiba, A. Fallahi, and B. Poppe. *THz coupler design for electron accelerators*. Bachelor thesis, Universität Oldenburg, DESY Hamburg, November 2013. URL http://pubdb.xfel.eu/record/168158/files/DESY-2014-02383.pdf.

List of Figures

List of Tables

Acronyms

RF radiofrequency.

3D three-dimensional.

SOL speed of light.

THz Terahertz.

IR infrared.

2D two-dimensional.

PhC Photonic Crystal.

FCC face-centered cubic crystal.

MPB MIT Photonic Bands.

FTDT Finite-difference time domain.

MEEP MIT Electromagnetic Equation Propagation.

PBG Photonic Band Gap.

ARROW anti-resonant reflecting optical waveguide.

LAZ laser affected zones.

HF hydrogen fluoride.

KOH potassium hydroxide.

NA numerical aperture.

$LiNbO_3$ lithium niobate.